ACOUSTIC PULSE DIFFRACTION BY CURVED AND PLANAR STRUCTURES WITH EDGES

By

Qin Zhang

B. Sc. (Electrical Engineering) Tianjin University

M. Sc. (Electrical Engineering) Beijing Broadcasting Institute

A THESIS SUBMITTED IN PARTIAL FULFILLMENT OF

THE REQUIREMENTS FOR THE DEGREE OF

DOCTOR OF PHILOSOPHY

in

THE FACULTY OF GRADUATE STUDIES

ELECTRICAL ENGINEERING

We accept this thesis as conforming

to the required standard

THE UNIVERSITY OF BRITISH COLUMBIA

October 1990

In presenting this thesis in partial fulfilment of the requirements for an advanced degree at the University of British Columbia, I agree that the Library shall make it freely available for reference and study. I further agree that permission for extensive copying of this thesis for scholarly purposes may be granted by the head of my department or by his or her representatives. It is understood that copying or publication of this thesis for financial gain shall not be allowed without my written permission.

Electrical Engineering

The University of British Columbia

6224 Agricultural Road

Vancouver, Canada

V6T 1W5

Date: *November 15th 1990*

Abstract

Efficient and accurate solutions of acoustic wave diffraction by a rigid step discontinuity and a curved half-plane are derived by the uniform geometrical theory of diffraction. These solutions can be used in seismic data processing to evaluate and, eventually, to improve the existing data processing procedures. They can also find applications in electromagnetics, microwave antenna design, acoustic design and sound engineering.

The rigid step discontinuity solution given in this thesis is more accurate than the existing solutions which are based on Kirchhoff theory of diffraction. This solution removes the previous restriction on the source and the receiver arrangement. It also provides high efficiency by the use of ray theory. This solution is further generalized to two offset half-planes and an inclined wedge. Solutions for more complicated structures can be obtained by superposition of these solutions with added interactions. The complex source position method is used to extend the omnidirectional point source solution to a beam source solution. The effect of changes of the directivity and orientation of the beam source is studied. Time-domain single and double diffraction coefficients are determined through direct Fourier transforming and convolution. An infinite impulse response filter is applied to the time-domain direct computation of single diffraction. This combination achieves a total saving of 75% of computing time over the frequency-domain approach.

Diffraction by a curved half-plane is analyzed with the inclusion of creeping wave diffraction and second order edge diffraction. An acoustic model of a curved half-plane is designed to verify the theory. The experimental results obtained by Mellema have verified the existence of the creeping wave diffraction and weak traces of the second order edge diffraction.

ii

Table of Contents

List of Figures

viii

Acknowledgement

Chapter 1

INTRODUCTION

1.1 Introduction

Scattering properties of subsurface complex shapes to the impinging energy from a point source, directional or omnidirectional, are of interest to the geophysicist. From the records of seismograph arrays, information can be extracted to predict the structure of the earth. Current seismic investigations include both reflection and refraction surveys, which complement each other. In recent years, owing to the advance of computers, sophisticated methods have been developed to obtain more accurate information about the scattering objects. Improved techniques in field surveys as well as in data processing have provided increasingly realistic images of scattering structures. Reflection seismics is an important method in applied geophysics, but it has limitations. The reflection image will be enhanced, when other forms of waves, such as diffraction from edges and shear waves, are included in the scattering image. As field survey technique improves and the need for a clear scattering image increases, the study of diffraction by complex shapes becomes more important both in theory and in application.

Because the solution to a specified scattering problem is unique, a scattering body can be uniquely represented by its scattering image. Generally speaking, a complete scattering image will include reflection, refraction and diffraction. A correct interpretation of the scattering results depends on the knowledge of the propagation properties of these wave forms. In the past, reflection and refraction have been thoroughly studied. The

investigation of diffraction has been restricted to very simple cases with limited accuracy, although it has become increasingly important, especially when sharp edges are involved.

Mathematical models to account for diffraction of acoustic effects can be found in the work of Trorey [1], [2] and Hilterman [3]. Kirchhoff theory has been used by Hilterman to construct zero offset synthetic scattering images. He also constructed an experimental model to verify his theoretical results. Owing to the limitations of the Kirchhoff theory, his theoretical scattering images are different from the measured results when sharp edges and corners are present. From the computational point of view, his program can only handle zero offset arrangements of the source and receiver pair. This greatly limits the application of the result. Also in his calculations, only omnidirectional sources can be used.

The numerical modelling of seismic diffraction by a perfectly reflecting wedge has been studied by Hutton [4]. In his paper, Biot and Tolstoy's [5] solution was used to construct the seismogram for the semi-infinite plane and an infinite wedge. Comparison between the exact result and Kirchhoff approximation was made. In Fig.17 (page 695 of [4]), he showed that the diffraction in the deep shadow region obtained from Kirchhoff approximation was 54% of the exact solution for an infinite half-plane. They also introduced Keller's geometrical theory of diffraction (GTD) and revealed that the GTD or high frequency solution for edge diffraction is generally more accurate than the Kirchhoff method.

The mathematical representation of the scalar electromagnetic waves and acoustic waves are almost identical. For a linear, homogeneous and isotropic medium, the electric and magnetic fields are described by Maxwell equations. In particular, for a monochromatic wave, each component of the electric and magnetic fields satisfies a second order linear wave equation. For the acoustic field, if the medium has negligible viscosity, its motion at all ordinary points in space is described by Newton's equations and the continuity equation. For harmonic time dependence, the velocity potential satisfies the same

second order linear wave equation as an electromagnetic wave. For a perfect conductor, the tangential electric field boundary condition is the same as the velocity potential boundary condition of a perfectly soft scatterer in acoustics. The tangential magnetic field boundary condition is the same as the boundary condition on a perfectly rigid scatterer. Thus, a solution for an electromagnetic model is also a valid solution to the corresponding acoustic model. In this thesis, the problem will often be discussed in terms of electromagnetic fields; then the results will be applied to the acoustic model.

In order to achieve both accuracy and efficiency, we have employed the GTD method throughout this thesis. The geometrical theory of diffraction [11], which can satisfy the boundary condition, is generally superior to the Kirchhoff diffraction theory in both accuracy and efficiency. Instead of directly dealing with the field problem, this method takes advantage of the high frequency property of the diffracted waves and uses ray methods to calculate the diffracted field. Diffractions are determined by three key factors— diffraction coefficient, amplitude and a phase shift. Amplitude and phase are calculated according to the rules of the geometrical optics. Diffraction coefficients are given by the asymptotic analysis of canonical problems.

In this thesis, scattering models are studied in the frequency-domain by the method of GTD. These solutions are most accurate for high frequencies. (By high frequencies we mean that the smallest dimension of the scattering body is larger than a wavelength.) The time-domain solution is then constructed for an appropriate pulse with suppressed low frequency components by inverse Fourier transforming the frequency-domain results. Both directional and omnidirectional sources are used with no restriction of source and receiver arrangement. The configurations modeled are the step discontinuity, inclined step, two parallel separated half-planes and a curved half-plane. Double edge diffractions are also included, which accurately give the total field in the transition regions. Creeping wave diffraction and the effect of the change of curvature in the half-plane are of interest.

In the transition regions, there are very strong second order edge diffractions and creeping wave diffractions. These diffractions are clear indications of the existence of the edges and the changes of the curvature, while it may not be obvious in the reflections. A digital filter approach to the time-domain solution is also investigated. For single diffraction by an edge, when away from the shadow and reflection boundaries, this approach can reduce the time of calculation by a factor of 4. The complex source point (CSP) method is used to extend the result of an omnidirectional source to a beam source. The combination of the GTD and CSP method greatly increases the efficiency and accuracy of the beam diffraction result. An experimental model of a curved half-plane has been designed and constructed. The creeping wave diffraction in the geometrical shadow is clearly shown in the experiment result, but experimental difficulties prevented the verification of the second order edge diffraction. The mathematical models and programs in this thesis can be easily adapted to analyze more complicated models. In comparison with the previous results, better agreement is demonstrated between the experimental data and our theoretical results. Calculation efficiency, accuracy and application potential are the main features of our new approach.

1.2 Geometrical Theory of Diffraction (GTD)

Rigorous mathematical studies of high-frequency diffraction by an edge date back about a century [6], [7], [8], [9]. The asymptotic analysis has been limited to simple shapes, since exact solutions are not available when the scattering body shape is complicated.

GTD was developed in the 1950s by Keller [10], [11]. This method includes diffraction as well as geometrical optics fields, but retains the simple form of the ray theory. In GTD, the ray path of diffraction is governed by Keller's generalized Fermat's principle, and the diffracted field is determined by multiplying the incident field by a diffraction coefficient,

a phase factor and an amplitude factor. The diffraction coefficient is obtained from the high-frequency asymptotic solution of a canonical problem. When the scattering object is large compared to the wavelength, and the field point is away from the edge, caustic and transition regions, GTD results agree with the exact asymptotic solution.

The fact that Keller's GTD fails in transition regions is a major defect. This difficulty was overcome by the uniform asymptotic theory of diffraction (UAT) [12], [13], [14], the uniform theory of diffraction (UTD) [15], and the spectral theory of diffraction (STD) [16]. In UTD and UAT, additional factors or terms which involve Fresnel integral are introduced to ensure that the diffracted field at the shadow boundary and reflection boundary behave regularly. In STD, a singularity-free spectral diffraction coefficient is obtained from the Fourier transform of the induced surface current distribution. Comparison studies have been conducted by Rahmat-Samii and Mittra [17]. The results indicate that the numerical solutions derived from the UAT and UTD theories are different but do not show large discrepancies. UAT gives the exact asymptotic solution for a half-plane but is approximate for a wedge. UTD is approximate for both but more versatile.

UTD keeps the simple form of GTD and gives finite values in transition regions. For a perfectly conducting half-plane, UTD can give exact solution. Fresnel integral is used in UTD to smoothly connect the fields across transition boundaries. The Fresnel integral can be easily computed by the Fresnel integral subroutine available on MTS in University of British Columbia (UBC). Because of these properties, the UTD formula is used here whenever edge diffraction is involved.

In the application of GTD, care must be taken to ensure that the high frequency condition is satisfied. For a plane with step discontinuities, the height of the step is the critical dimension which should not be less than a wavelength of the lowest significant frequencies of the acoustic pulse. For a curved half-plane, the radius of the curved surface should be greater than the wavelength of the lowest significant frequencies of the acoustic

pulse. The position of the source and receiver must be located away from the edge. The closest distance from the source or receiver to the edge should be greater than a quarter of the longest significant wavelength of the pulse, otherwise inaccuracy may occur.

1.2.1 Uniform Theory of Diffraction

UTD was developed by Kouyoumjian and Pathak in 1974 [15]. By an extra multiplier with a Fresnel integral, they gave the diffraction coefficient a uniform character. They also extended UTD to the edge formed by curved screen. This extension was justified by the argument of the local effect of the diffraction phenomenon. UTD as a directly modified version of GTD has been widely used in antenna analysis and design.

According to GTD, a high-frequency wave incident on a discontinuous surface with an edge gives rise to a reflected wave and an edge-diffracted wave. The total field observed with the presence of the edge is the sum of the incident field, the reflected field and the diffracted field,

$$u = u^i + u^r + u^d, \qquad (1.1)$$

or

$$u = u^{g.o.} + u^d. \qquad (1.2)$$

In equation 1.2, $u^{g.o.}$ is the geometrical optics field, which is composed of the incident field u^i and the reflected field u^r; u^d is the diffracted field. The geometrical optics field $u^{g.o.}$ can be easily found by ray methods. Referring to figure 1.1, the UTD edge diffracted field can be expressed as

$$u^d(\rho) \sim u^i(Q) \cdot D(L, \phi, \phi') \cdot A(\rho) \cdot \exp(-jk\rho). \qquad (1.3)$$

Here, $A(\rho)$ describes the spatial variation of field amplitude along the diffracted ray,

$$A(\rho) = \begin{cases} \sqrt{\frac{1}{\rho}} & \text{for plane, cylindrical wave incidence,} \\ \sqrt{\frac{\rho'}{\rho(\rho+\rho')}} & \text{for spherical wave incidence,} \end{cases} \qquad (1.4)$$

where ρ' and ρ are the distances from the source to the edge and from the edge to the field point respectively. $u^i(Q)$ is the incident field on the edge. $\exp(-jk\rho)$ is the phase variation along the diffracted ray. $D(L, \phi, \phi')$ is the diffraction coefficient obtained from the high-frequency asymptotic solution of the canonical problem, ϕ and ϕ' are incident and diffracted angles, and L is a distance parameter. For soft (upper sign) and hard (lower sign) boundaries, the diffraction coefficients are given by the following equation [15]

$$
\begin{aligned}
2D_{s,h}(L, \phi, \phi') = \frac{-\exp[-j(\pi/4)]}{2n\sqrt{2\pi k}} \Bigg\{ &\cot[\frac{\pi + (\phi - \phi')}{2n}]F[kLa^+(\phi - \phi')] \\
&+ \cot[\frac{\pi - (\phi - \phi')}{2n}]F[kLa^-(\phi - \phi')] \\
&\mp \cot[\frac{\pi + (\phi + \phi')}{2n}]F[kLa^+(\phi + \phi')] \\
&\mp \cot[\frac{\pi - (\phi + \phi')}{2n}]F[kLa^-(\phi + \phi')] \Bigg\},
\end{aligned}
\tag{1.5}
$$

where n is a parameter describing the wedge angle. When the two planes forming the wedge are $\phi = 0$ and $\phi = n\pi$, the wedge interior angle is $(2 - n)\pi$, as shown in figure 1.1. The modified Fresnel integral $F(x)$ is defined by

$$
F(x) = 2j\sqrt{x}\exp(jx)\int_{\sqrt{x}}^{\infty}\exp(-j\tau^2)d\tau,
\tag{1.6}
$$

in which one takes the principal (positive) branch of the square root. The parameter $a^{\pm}(\beta)$ are given by

$$
a^{\pm}(\beta) = 2\cos^2(\frac{2n\pi N^{\pm} - \beta}{2})
\tag{1.7}
$$

in which $N^{\pm}$ are the integers which most nearly satisfy the equations

$$
2\pi n N^+ - \beta = \pi
\tag{1.8}
$$

and

$$
2\pi n N^- - \beta = -\pi,
\tag{1.9}
$$

with $\beta = \phi \pm \phi'$. For an arbitrary wave front incident on a straight wedge, the distance parameter L is given by the following equation:

$$L = \frac{\rho(\rho_e^i + \rho)\rho_1^i\rho_2^i}{\rho_e^i(\rho_1^i + \rho)(\rho_2^i + \rho)},$$ (1.10)

where ρ_1^i and ρ_2^i are the principle radii of the curvature of the incident wavefront, ρ_e^i is the radius of the curvature of the incident wavefront at the diffraction point in the plane containing the incident ray and the unit vector tangent to the wedge.

There are several special cases when the diffraction coefficients given by equation 1.5 can be considered separately. For grazing incidence, D_s is zero and D_h must be multiplied by a factor of 0.5. If the wedge interior corner angle is π/m, where m is an integer, the diffraction coefficient will vanish, and the boundary value problem can be solved exactly by the image method.

Because GTD method is only valid when the incident field is a ray field and spatially slowly varying, we must pay special attention to the situation of double diffraction when the second edge is located in the transition region of the diffracted field emerging from the first edge. In this case, the incident field at the second edge is not spatially slowly changing; consequently, the above GTD equation cannot apply. This special case has been investigated by several authors with different methods. Lee and Boersma [18] used UAT and Tiberio and Kouyoumjian [19] [20] and Tiberio, Manara, Pelosi and Kouyoumjian [64] used UTD. The results of Tiberio and Kouyoumjian are adopted in chapter two to solve the double diffraction of a hard step.

1.2.2 Creeping Wave Diffraction

Apart from the edge diffraction, there is creeping wave diffraction for smoothly curved surface. The GTD result of creeping wave diffraction for smooth objects was obtained by Levy and Keller [21]. They obtained the diffraction coefficient and attenuation constant

of the creeping wave for a smooth surface by comparing the GTD form and the high frequency asymptotic expansion of the rigorous solution of diffraction by a cylinder and sphere.

The edge diffraction coefficient for the creeping wave was derived much later. Albertsen and Christiansen [22] constructed some creeping wave hybrid diffraction coefficients from a set of elementary diffraction coefficients. But there is no rigorous proof for the perfectly conducting curved sheet. Later Idemen and Erdogan [23], using Fock's result [29], solved the second order canonical problem of GTD— diffraction by a perfectly conducting curved sheet. They used a generalized cylindrical coordinate to construct a Hilbert problem and found a high frequency asymptotic solution. From this solution, they extracted the various diffraction coefficients (or transformation coefficients, as they were called in their paper) for the creeping wave.

1.2.3 Second Order Edge Diffraction

The geometrical theory of diffraction provides us with a means to accurately and efficiently analyze the scattering wave. A crucial step in applying GTD is to find an appropriate diffraction coefficient. Some diffraction coefficients can be derived by the asymptotic solution of a canonical diffraction problem. Other problems cannot be solved by this procedure and different methods are used to construct approximate diffraction coefficients.

Weston [30] studied the effect of a discontinuity in the curvature on the high frequency scattering. He modeled the problem by conjunction of two parabolic cylinders and solved the current distribution asymptotically. Senior [31] extended Weston's work by extracting the diffraction coefficient from the asymptotic expansion. But Senior's result is non-uniform and invalid in the vicinity of the reflection boundary where the diffraction is significant. James [32] derived a diffraction coefficient for the edge formed by a smoothly

joined cylinder based on both the theory of physical optics and Senior's result. James' result gives the correct diffraction on the reflection boundary and retains Senior's result away from the reflection boundary.

1.3 Thesis Overview

This thesis will emphasize accuracy, efficiency and application. We will target the topics which have very high application value, but with no existing accurate and efficient solution. The UTD is used in edge diffraction. The complex source point method is employed for the beam diffraction. A time-domain infinite impulse response (IIR) digital filter approach is investigated. An experimental model for curved surface diffraction is constructed. The measured results show good agreement with theoretical predictions.

In chapter two, mathematical models of transient pulse diffraction are studied by the method of UTD. Soares and Giarola [33] analyzed a 90° step in hard plane by UTD for plane wave incidence. The solutions obtained here are more general. The important but analytically difficult situation where source or receiver lies on the reflection boundary for the multiple diffraction is also included; Soares and Giarola's result fails in this instance. The solution is then extended to other diffraction models related to the step. This includes diffraction by two offset half-planes and diffraction by an inclined step. Time-domain diffraction is constructed for an appropriate pulse with suppressed low frequency components. Numerical examples are presented which demonstrate the importance of including multiple reflection and diffraction for such models.

In chapter three, the complex source point method is used for beam diffraction. One advantage of the frequency-domain approach is that the solution can be easily adapted to directional sources with Gaussian beam patterns. By changing the source position coordinates from real to complex, a beam diffraction result can be obtained. Suedan

and Jull [34] have used the complex source point method to convert an omnidirectional source diffraction solution into a beam solution for the half-plane and wedge diffractions. In their paper, the combination of UTD and complex source point method is investigated. Result showed that this combination provides accurate far field values for all parameters of the complex source position. Here, both frequency and time-domain beam diffraction by a step discontinuity are obtained. The complicated ray tracing procedure has been avoided. The numerical results show that the diffraction is enhanced when a beam is focused on the edge and weakened when a beam is aimed away from the edge. By using directional source, with zero offset source and receiver pair, diffraction from the edge is much weaker than for omnidirectional source incidence. Above the edge, the response of reflection and diffraction are relatively the same. When we position the source and receiver pair above the edge and change the beam direction over the entire step plane, the diffraction response increases as the source points to the edge, while the reflection becomes weaker as the source points away from the edge.

Time-domain filtering technology is investigated in chapter four. Dalton and Yedlin [38] obtained an exact time-domain solution for diffraction of acoustic waves by a half-plane by inverse Fourier transforming the frequency-domain integral solution and used a filtering method to calculate the pulse diffraction by a half-plane. Here, a similar approach is used. First, we transfer the frequency-domain UTD diffraction coefficient to the time-domain. Then an infinite impulse response (IIR) filter is used to carry out the convolution. Because the FFT and discrete convolution procedures are eliminated from the computer program, this method consumes only a quarter of the time used by the FFT. The filter design method discussed by Shanks [39] and Burrus and Parks [40] is used in IIR filter design. The filtering technology is not widely used in electromagnetic fields and this study should also serve the purpose of drawing attention to the filtering technology in wave propagation problems.

Curved half-plane diffraction is more complicated and has very interesting features. High frequency diffraction of the curved surface has been studied by Fock [29] and his USSR colleagues. The principle of the local field in the penumbra region established by Fock is basic to the analysis of the high-frequency diffraction by a convex, perfectly conducting object with continuously varying curvature. A convex side of a cylindrically curved sheet joined by a half-plane was investigated by Weston [30], Hong and Weston [42], Senior [31] and James [32]. Idemen [23] studied the case of oblique incidence on a perfectly conducting cylindrical sheet and derived the diffraction coefficient for the creeping wave. In chapter five, a complete GTD result for general spherical scalar wave incidence from an arbitrary point above the perfect hard surface is obtained. This solution includes the geometrical optics field, the edge diffracted creeping wave and space ray, and the second order edge diffracted space ray. An experimental model has also been constructed and the measured results demonstrate good agreement with theory [43], [59]. The creeping wave diffraction shown in the measured results are clearly seen on the theoretical result. Because of limitations of the present experimental set-up, the second order edge diffraction is masked by reflection in the experimental results.
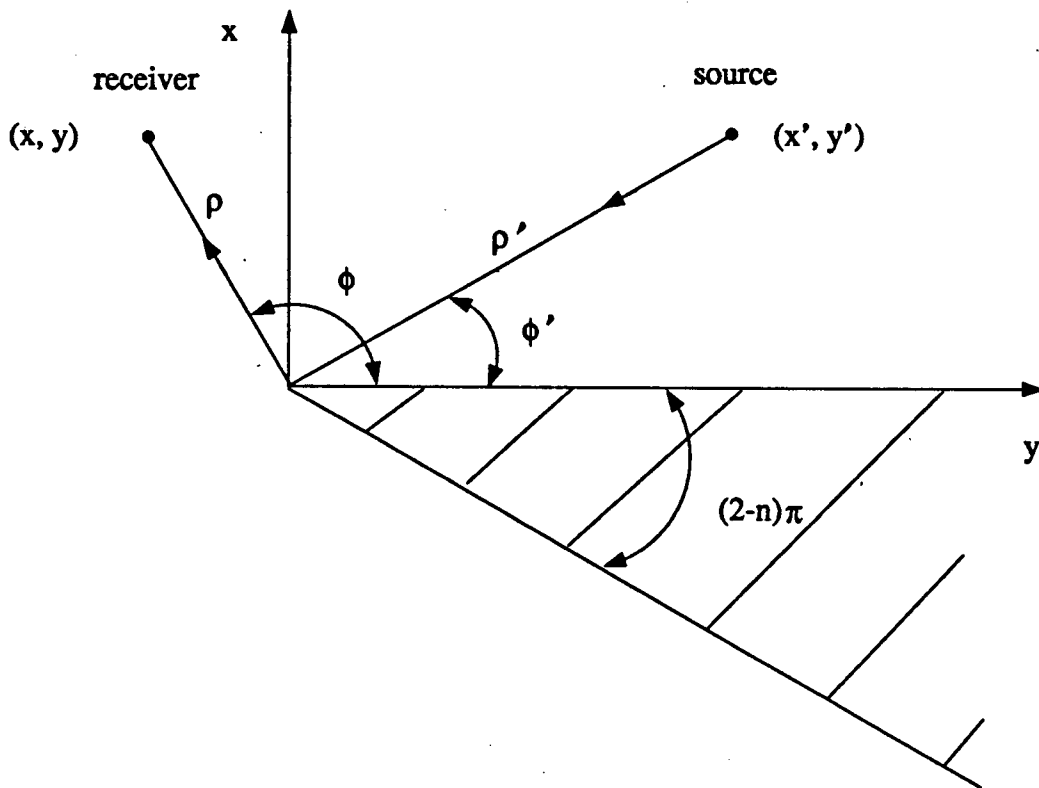
Figure 1.1: The configuration of a spherical wave diffraction by a wedge with an interior angle $(2 - n)\pi$.

Chapter 2

DIFFRACTION OF A STEP DISCONTINUITY

2.1 Introduction

Diffracting edges produce characteristic signatures in seismic records. As these may indicate the presence of geological faults and possible associated hydrocarbon traps, they have long been of interest in seismology. Edges caused by normal faulting frequently occur, for example, in the Horst and Graben structures found in the North Sea. Mathematical models to account for diffraction usually have been limited to acoustic effects. Examples are the work of Trorey [1] [2] and Hilterman [3] who used Kirchhoff diffraction theory to study acoustic sections. Hilterman also provided experimental data which for many geometries supported his theory. However for normal faults his theory, because of its inherent limitations, fails to account for the corner reflections and double diffraction evident in the experimental results. Jebsen and Medwin [44] investigated diffraction backscatter from a semi-infinite plate and a rigid wedge in the time and frequency domains. The spectrum of diffraction, as predicted by use of the Kirchhoff assumption in the Helmholtz-Kirchhoff integral formulation, was compared to the experimental results and was found to be substantially incorrect.

Frequency domain solutions of high-frequency diffraction by a step discontinuity or thick half-plane have been difficult. Jones [45] obtained a low-frequency asymptotic solution of the diffraction by a thick semi-infinite plate for a two-dimensional plane wave incidence by Wiener-Hopf technique. The explicit solution can only be obtained for the

14

case that the thickness of the plate is less than one-tenth of the wave-length. Kobayashi [46], [47] extended Jones' solution to a rectangular conducting rod and derived a high-frequency asymptotic solution. His results are not valid when the source and receiver lie on the reflection boundary because the field incident on the second edge is not spatially slowly varying, and therefore, the standard GTD approach fails. Michaeli [48], [49] used a method based on the extension of the physical theory of diffraction, in which the radiation integral over the actual induced current is replaced by the Helmholtz integral over a surface enclosing the wedges. Then an extended spectral theory of diffraction and a singularity-matching procedure is proposed to obtain a uniform doubly diffracted field. The limitation of his solution is that the incident wave is approximately planar throughout the gap between the edges. Solutions for the spherical wave are only available for the case that receiver or source lies exactly on the reflection boundary, given by Tiberio and Kouyoumjian [20]. Recently, Tiberio et al [64] published another paper which studied the double edge diffraction problem. The solution is valid for arbitrary positions of source and receiver, but it still has the restriction of plane wave incidence.

Plane wave diffraction by a $90°$ step in a hard plane was analyzed by Soares and Giarola [33] with UTD. The solution given here is more general as it is for an omnidirectional local source. The important but analytically difficult situation where source or receiver lies on the reflection boundary for multiple diffraction is also included; Soares and Giarola's result fails in this instance. In addition, this solution is extended to pulse diffraction.

The GTD [11], which can satisfy the boundary conditions, generally is superior to Kirchhoff diffraction theory in both accuracy and efficiency, but it fails at and near shadow and reflection boundaries because of singularities in the diffraction coefficients. Here, UTD [15] is used to model acoustic pulse diffraction by step discontinuities on planar structures. This shows considerable improvement over the earlier methods in

accurately and efficiently accounting for the observations. It also suggests that errors may occur in using Kirchhoff theory with inversion of seismic data.

The basic procedure here is to develop a frequency-domain solution for acoustic point source diffraction by a step on a plane surface with a hard boundary condition [50]. This solution is most accurate for high frequency diffraction. The limiting dimension is that of the step: it should not be much less than a wavelength in height for the lowest significant frequency of the acoustic pulse. The time domain solution is then constructed for an appropriate pulse with suppressed low frequency components. Numerical examples are presented which demonstrate the importance of including multiple reflection and diffraction for such models, which are canonical in the sense that seismic records for acoustic pulse diffraction by more complex geometries may be constructed by their superposition with added interaction.

2.2 Diffraction by A 90° Step

In figure 2.2a a point source of velocity potential $u^i = R^{-1} \exp(-jkR)$ is located at ρ', ϕ' from the upper edge (x=y=0) of a 90° step discontinuity in a plane surface with a hard boundary. The total fields that arrive at the receiver are comprised of the incident field from the source, the reflected field from the plane surface and the corner of the step, and the diffraction from the edge. Owing to the interaction of the edge and the lower boundary, there are also multiple diffractions. Here, the consideration is limited to double diffractions, for higher order diffractions are insignificant.

2.2.1 Geometrical Optics Fields

The geometrical optics field can be written

$$u^{g.o.} = u^i + u^r_1 + u^r_2 + u^r_3, \qquad (2.11)$$
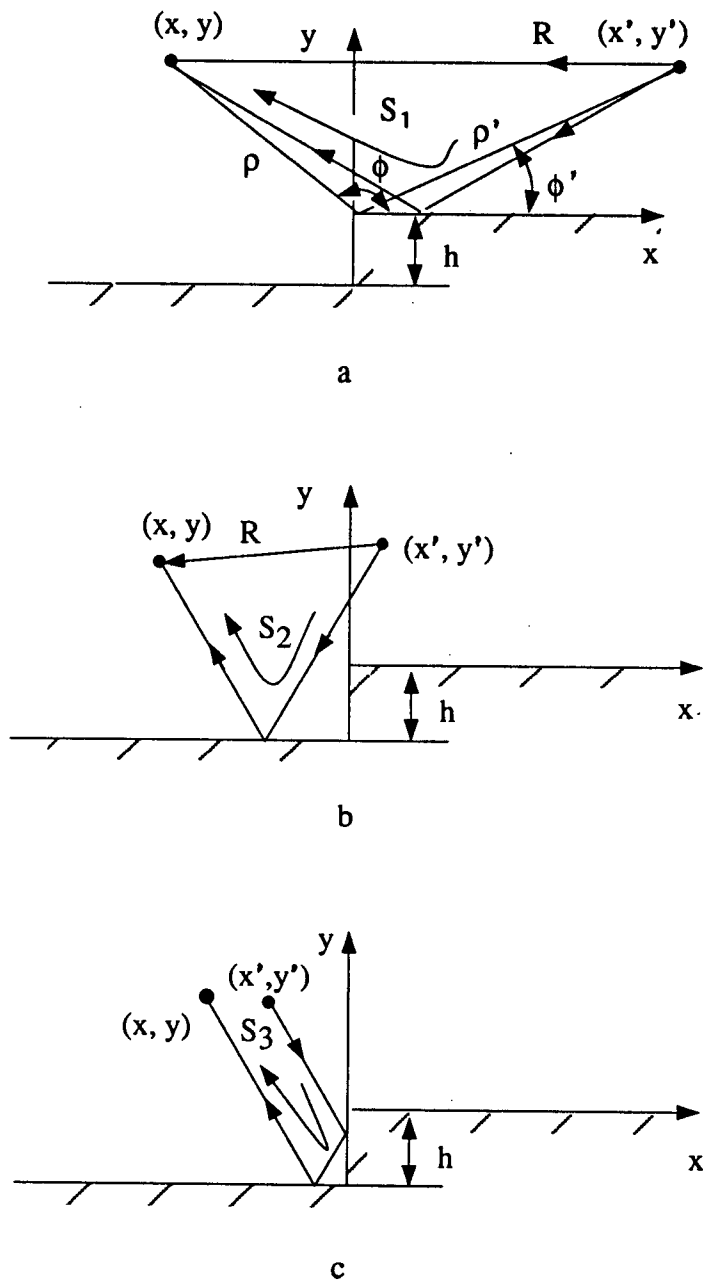
Figure 2.2: Paths of direct and reflected ray. A source at (ρ', ϕ') and a receiver at (ρ, ϕ) from the edge of a 90° step in a plane for different source-receiver positions.

where u_1^r and u_2^r are reflected fields from the upper and lower boundary planes, as shown in figure 2.2a and figure 2.2b, and u_3^r is the reflected field from the walls of the corner as in figure 2.2c. For source and receiver in the x-y plane, the reflected fields at ρ, ϕ are

$$u^i = U(\pi + \phi' - \phi)\frac{\exp(-jkR)}{R}, \tag{2.12}$$

$$u_1^r = U(\pi - \phi' - \phi)\frac{\exp(-jkS_1)}{S_1}, \tag{2.13}$$

$$u_2^r = U(\phi - \Phi_1)\frac{\exp(-jkS_2)}{S_2}, \tag{2.14}$$

$$u_3^r = U(\phi - \frac{\pi}{2})U(\phi - \Phi_2)U(\Phi_3 - \phi)\frac{\exp(-jkS_3)}{S_3}, \tag{2.15}$$

with $U(x) = 1$, $x > 0$ and $U(x) = 0$, for $x < 0$. R is the distance from the source to the receiver on the incident ray path in figure 2.2a. S_1 is the distance from the source to the receiver along the reflected ray path. Similarly for S_2 and S_3 as indicated in figure 2.2b and figure 2.2c. The angular limits for the optics field can be obtained from figure 2.3. When the sum of the source and receiver angles ($\phi' + \phi$) is less than π, the reflected wave from the upper boundary can reach the receiver. Beyond this limit, no reflection from the upper boundary can be received by the receiver. The reflection boundary of the lower surface can be obtained from figure 2.3b. When the source is in the right half plane, the reflection boundary is in the left half plane; when the source is in the left half plane, the reflection boundary is in the right half plane. From the geometry, Φ_1 can be expressed as

$$\Phi_1 = \begin{cases} \pi - \phi' + \arctan\frac{2h\cos\phi'}{\sqrt{\rho^2 - 4h^2\cos^2\rho'}}, & \text{if}\phi' < \pi/2, \text{ and}|\frac{2h}{\rho}\cos\phi'| < 1; \\ 2\pi, & \text{if}\phi' < \pi/2, \text{ and}|\frac{2h}{\rho}\cos\phi'| \geq 1; \\ \arctan|\frac{y'+2h}{x'}|, & \text{if}\phi' > \pi/2. \end{cases} \tag{2.16}$$

The angular limits for the reflection from the corner can by obtained from figure 2.3c, which can be summarized as

$$\Phi_2 = \pi - \arctan|\frac{y'+2h}{x'}|, \tag{2.17}$$
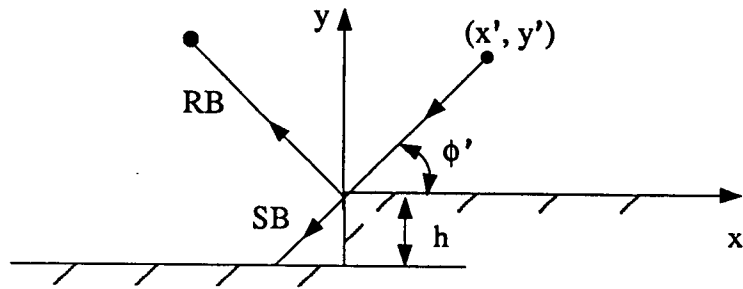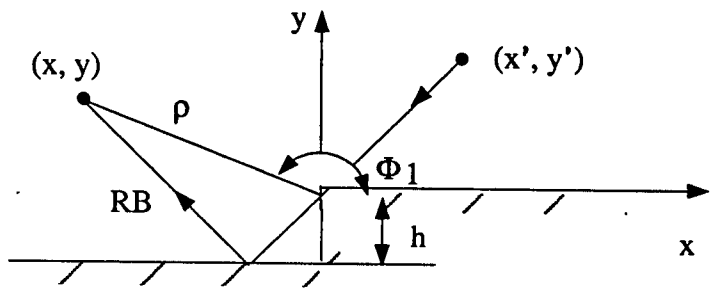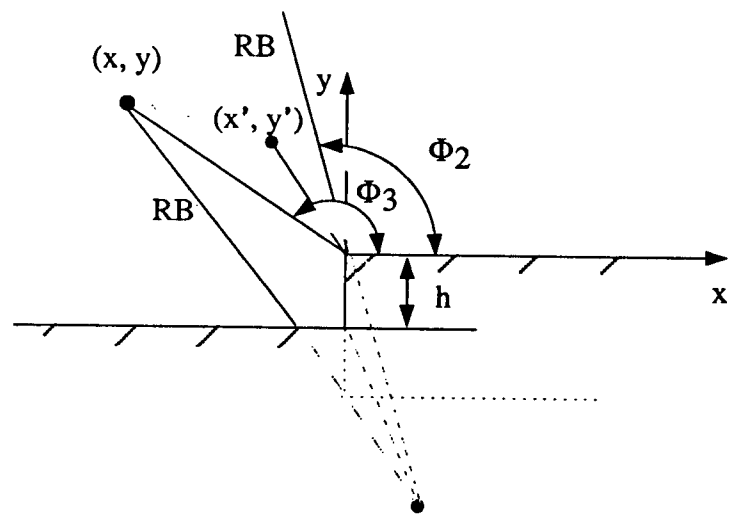
Figure 2.3: Reflection boundaries and shadow boundaries for a source at different locations above a step discontinuity.

$$\Phi_3 = \begin{cases} \phi' - \arctan \dfrac{2h \cos \phi'}{\sqrt{\rho^2 - 4h^2 \cos^2 \phi'}}, & |\frac{2h}{\rho} \cos \rho'| < 1; \\ 2\pi, & |\frac{2h}{\rho} \cos \rho'| \geq 1. \end{cases} \qquad (2.18)$$

The distance parameters are given by

$$R = \sqrt{(x - x')^2 + (y - y')^2}; \qquad (2.19)$$

$$S_1 = \sqrt{(x - x')^2 + (y + y')^2}; \qquad (2.20)$$

$$S_2 = \sqrt{(x - x')^2 + (y + y' + 2h)^2}; \qquad (2.21)$$

$$S_3 = \sqrt{(x + x')^2 + (y + y' + 2h)^2}. \qquad (2.22)$$

2.2.2 Singly Diffracted Fields

The geometrical optics field of equation 2.11 is discontinuous at shadow and reflection boundaries given by the angular limits. These field discontinuities are reduced by successive diffracted fields of which the singly diffracted fields are dominant. Their ray paths are shown in figure 2.4. For example, the reflection from the upper surface is discontinuous at the reflection boundary RB, shown in figure 2.4a. This discontinuity is compensated for by the diffraction from the edge, where the amplitude of the diffraction is half of the reflection with a different sign on each side. Thus, the total field is continuous on the reflection boundary and half of the reflection.

By GTD, the singly diffracted field at ρ, ϕ in the x-y plane containing the source and the edge in figure 2.4a is

$$u^d(\rho, \phi; \rho', \phi') = \frac{\exp[-jk(\rho + \rho')]}{\rho'} D\left(\frac{\rho\rho'}{\rho + \rho'}, \phi, \phi'\right) \sqrt{\frac{\rho'}{\rho(\rho + \rho')}}, \qquad (2.23)$$

in which the scalar diffraction coefficient $D(L, \phi, \phi')$ of Kouyoumjian and Pathak [15] is given in equation 1.5 and the distance parameter L for a spherical wave is given in equation 1.10. This result (2.23) is not exact but its accuracy is well established. For
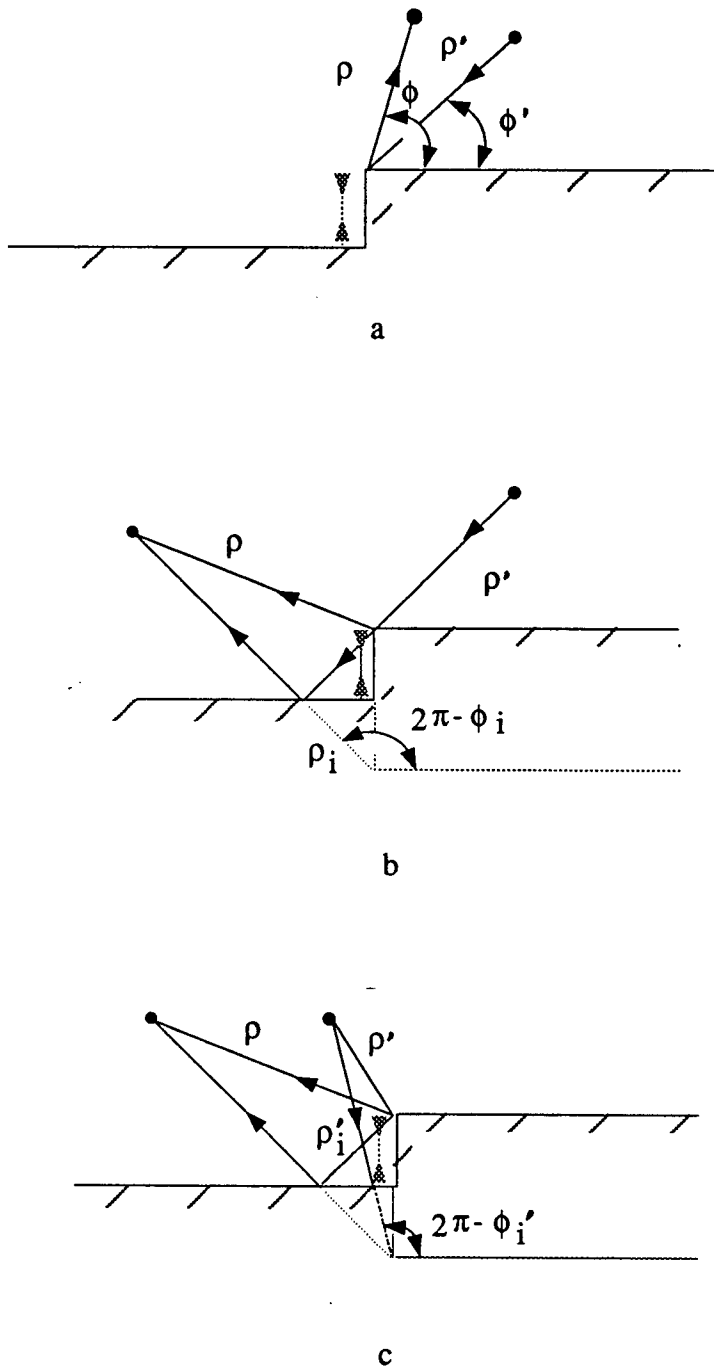
Figure 2.4: Diffracted ray paths over a hard step discontinuity with source and receiver at different locations. The dashed vertical paths indicate multiple diffractions.

a 90° wedge its graphical numerical values generally are indistinguishable from exact values (Suedan and Jull [34], figure 7). Also, the diffraction coefficient is not singular at shadow and reflection boundaries and has the considerable advantage of being expressed in terms of Fresnel integral which can be efficiently calculated from available computer subroutines. Moreover, Fresnel integral time-domain transforms can be expressed in closed form, providing exceptional computational gain in single diffraction.

Equation 2.23 is the entire singly diffracted field if both source and receiver are in $x > 0$ ($\phi, \phi' < \pi/2$), as in figure 2.4a. If $\phi' < \pi/2$ and $\phi > \pi/2$ singly diffracted fields from the edge are reflected from the lower plane back to the receiver, figure 2.4b. The total singly diffracted field is then

$$u^d(\rho, \phi; \rho', \phi') + u^d(\rho_i, \phi_i; \rho', \phi'), \tag{2.24}$$

where ρ_i, ϕ_i are the coordinates of the receiver relative to the image of the upper edge in the lower boundary in figure 2.4b

$$\rho_i = \sqrt{x^2 + (y + 2h)^2}, \tag{2.25}$$

$$\phi_i = \frac{3\pi}{2} - \tan^{-1}|\frac{x}{y + 2h}|. \tag{2.26}$$

If both source and receiver are in $x < 0$ ($\phi, \phi' > \pi/2$), there are, in addition, reflected fields from the lower boundary which are diffracted directly or after reflection back to the receiver, as illustrated by the ray paths in figure 2.4c and figure 2.4d. The total singly diffracted field is then

$$u^d(\rho, \phi; \rho', \phi') + u^d(\rho_i, \phi_i; \rho', \phi') + u^d(\rho, \phi; \rho'_i, \phi'_i) + u^d(\rho_i, \phi_i; \rho'_i, \phi'_i), \tag{2.27}$$

where ρ'_i, ϕ'_i are the source coordinates relative to the image of the upper edge in the lower boundary.

$$\rho^i = \sqrt{(x')^2 + (y' + 2h)^2}, \tag{2.28}$$

$$\phi'_i = \frac{3\pi}{2} - \tan^{-1} |\frac{x'}{y' + 2h}|. \tag{2.29}$$

There is no diffraction at the lower edge of the corner. This applies to all corners where the interior wedge angle is an integer fraction of π radians, for then the boundary conditions on the walls of an infinite wedge are satisfied exactly by an incident field and the fields of a finite number of images.

2.2.3 Doubly Diffracted Fields

Fields diffracted from the edge in the $\phi = 3\pi/2$ direction of figure 2.4 are again diffracted after reflection from the lower boundary, as indicated by the dashed line. These doubly diffracted fields are weaker than the singly diffracted fields (unless on the reflection boundary of the singly diffraction field) and arrive at the observation point later in the time. In the frequency-domain, they further improve field continuity at the reflection boundaries.

If both source and receiver are in $x > 0$ ($\phi, \phi' < \frac{\pi}{2}$), the total doubly diffracted field is

$$
\begin{aligned}
u^{dd}(\rho, \phi; \rho', \phi') &= \frac{\exp[-jk(\rho' + \rho + 2h)]}{\rho'} D(\frac{2h\rho'}{2h + \rho'}, \frac{3\pi}{2}, \phi') \sqrt{\frac{\rho'}{2h(2h + \rho')}} \\
&\quad \times D(\frac{2h\rho}{2h + \rho}, \phi, \frac{3\pi}{2}) \sqrt{\frac{\rho' + 2h}{\rho(\rho + \rho' + 2h)}}
\end{aligned} \tag{2.30}
$$

If the source is in $x > 0$ ($\phi' < \pi/2$) and the receiver is in $x < 0$ ($\phi > \pi/2$) as in figure 2.4b, the doubly diffracted field is given by equation 2.24 with u^{dd} replacing u^d and if both source and receiver are in $x < 0$ ($\phi, \phi' > \pi/2$) as in figure 2.4c and figure 2.4d, the doubly diffracted fields are given by 2.27 with u_{dd} replacing u_d in all terms.

The ray paths of higher order diffractions are those in figure 2.4 with an additional bounce between the upper edge and the lower boundary. The above expressions fail in the transition regions of the doubly diffracted fields; i.e., if the source is in the vicinity

of the reflection boundary ($\phi' \approx \pi/2$). This situation has been examined by Tiberio and Kouyoumjian [19], [20]. From their results a doubly diffracted field for $\phi' = \pi/2$ can be determined as

$$
\begin{aligned}
u^{dd}(\rho, \phi; \rho', \frac{\pi}{2}) &= \frac{\exp[-jk(\rho' + 2h)]}{2(\rho' + 2h)} D\left(\frac{(\rho' + 2h)\rho}{2h + \rho' + \rho}, \phi, \frac{3\pi}{2}\right)\sqrt{\frac{\rho' + 2h}{\rho(2h + \rho' + \rho)}} \\
&+ \frac{\exp(-jk\rho')}{2\rho'} D_2 D\left(\frac{2h\rho}{2h + \rho}, \phi, \frac{3\pi}{2}\right)\sqrt{\frac{\rho}{(\rho' + 2h)(\rho + \rho' + 2h)}} \quad (2.31)
\end{aligned}
$$

where

$$
D_2 = -\frac{2\exp(-j\pi/4)}{3\sqrt{2\pi k}} \cot\left(\frac{2\pi}{3}\right) F\left[2k\frac{\rho'(\rho + 2h)}{\rho + \rho' + 2h}\right] \quad (2.32)
$$

is a new diffraction coefficient needed for the doubly diffracted field with $\phi' = \pi/2$. $F(x)$ is the modified Fresnel integral given by equation 1.6. Reciprocity can be used to obtain a similar expression for $\phi = \pi/2$ and arbitrary ϕ' from 2.31, but these results are valid for either ϕ' or $\phi = \pi/2$ only. A more general result for arbitrary values of ϕ and ϕ' near $\pi/2$ and spherical wave incidence is substantially more involved and has not yet been determined.

Triple and higher order multiple diffraction may also be included by continuing this procedure. Successive diffractions represent additional interactions between the edge and the lower plane along the dashed ray paths of figure 2.4. Each diffracted field is weaker and later in arrival than the last at the receiver. If the receiver and source are both in the right half plane and the receiver is not in the transition region, the triply diffracted field is given by

$$
\begin{aligned}
u^{ddd} &= \frac{\exp(-jk\rho')}{\rho'} D\left(\frac{2h\rho'}{2h + \rho'}, 270^\circ, \phi'\right)\sqrt{\frac{\rho'}{2h(2h + \rho')}} \exp(-j2kh) \\
&\times D(h, 270^\circ, 270^\circ)\sqrt{\frac{\rho' + 2h}{2h(\rho' + 4h)}} \exp(-j2kh) \\
&\times D\left(\frac{2h\rho}{2h + \rho}, \phi, 270^\circ\right)\sqrt{\frac{\rho' + 4h}{\rho(\rho + \rho' + 4h)}} \exp(-jk\rho). \quad (2.33)
\end{aligned}
$$

Multiple diffraction can be obtained by adding higher order diffractions to the expression above. For plane wave incidence ($\rho' \to \infty$) the multiply diffracted fields can be written in a closed form

$$
\begin{aligned}
u^d_{total} \;\; = \;\; & D(\rho, \phi, \phi')\frac{\exp(-jk\rho)}{\sqrt{\rho}} + D(2h, 270^\circ, \phi)D(\frac{2h\rho}{2h+\rho}, \rho, 270^\circ) \\
& \times \frac{\exp[-jk(2h+\rho)]}{\sqrt{2h\rho}} \left[1 + \sum_{i=1}^{\infty} D^i(h, 270^\circ, 270^\circ)(\frac{\exp(-j2h)}{\sqrt{2h}})^i \right], \quad (2.34)
\end{aligned}
$$

or

$$
u^d_{total} = \frac{\exp(-jk\rho)}{\sqrt{\rho}} \left[D(\rho, \phi, \phi') + \frac{D(2h, 270^\circ, \phi')D(\frac{2h\rho}{2h+\rho}, \phi, 270^\circ)}{\sqrt{2h}\exp(j2kh) - D(h, 270^\circ, 270^\circ)} \right]. \quad (2.35)
$$

The above equation agrees with that of Soares and Giarola ([33], equation (5)). However, as the triple and higher order multiply diffracted fields are of limited accuracy and significance they are omitted in the calculated values presented. In the results which follow the total field is the sum of the incident and reflected fields, the singly diffracted fields and the doubly diffracted fields. However, examples of triple diffraction will be shown in both the time and frequency domains in order to compare with the single and double diffractions.

2.3 Frequency-Domain Results

Results of the last section are used to calculate the scattering field of a normal step discontinuity on an acoustic hard plane. Geometrical optics fields, single diffraction, double diffraction, and triple diffraction are shown separately. Numerical results show that the single and double diffraction are very important in getting a continuous total scattered field, while the triple diffractions are insignificant.

Figure 2.5 and figure 2.6 show the total and diffracted field patterns at a distance $\rho = 3\lambda$ from the edge of a 90° step discontinuity with $h = \lambda$ illuminated by a point
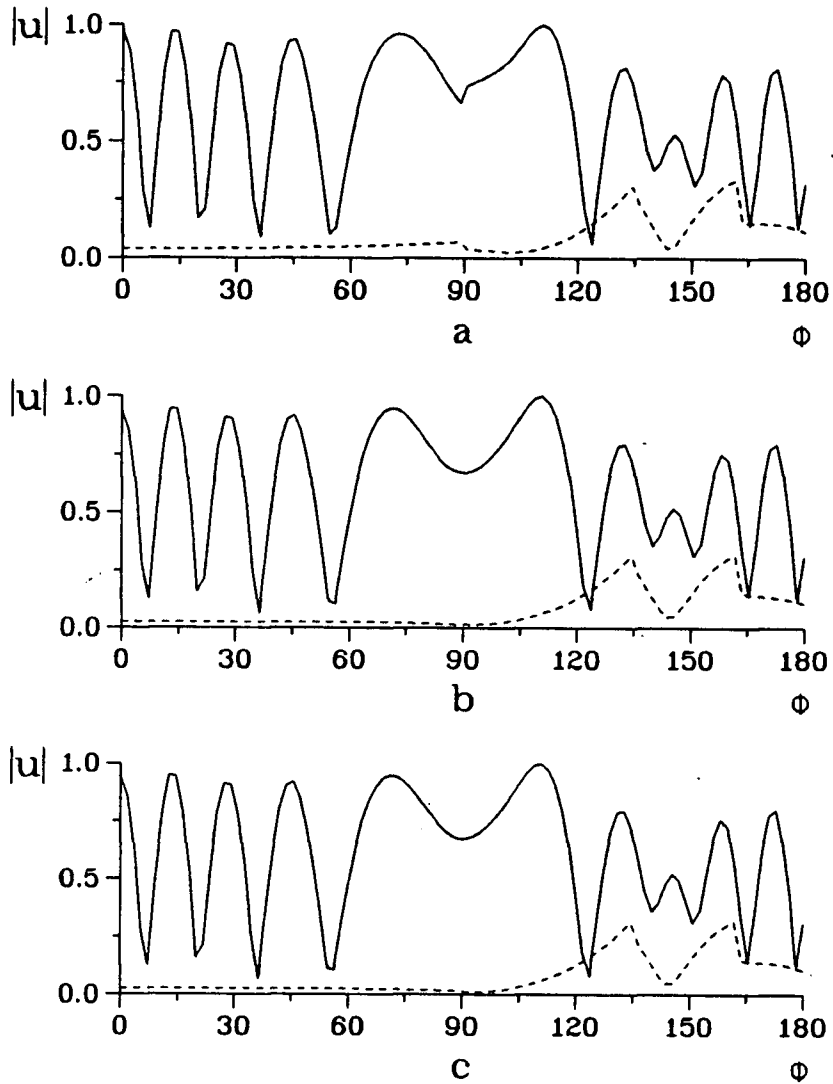
Figure 2.5: Total field and diffracted field from a step discontinuity with h=λ illuminated by a point source at $\rho' = 1000\lambda$ and $\phi' = 45°$. Solid curves represent the total field, dashed curves represent the diffracted field. a: single diffraction; b: single and double diffraction; c: single, double and triple diffraction.
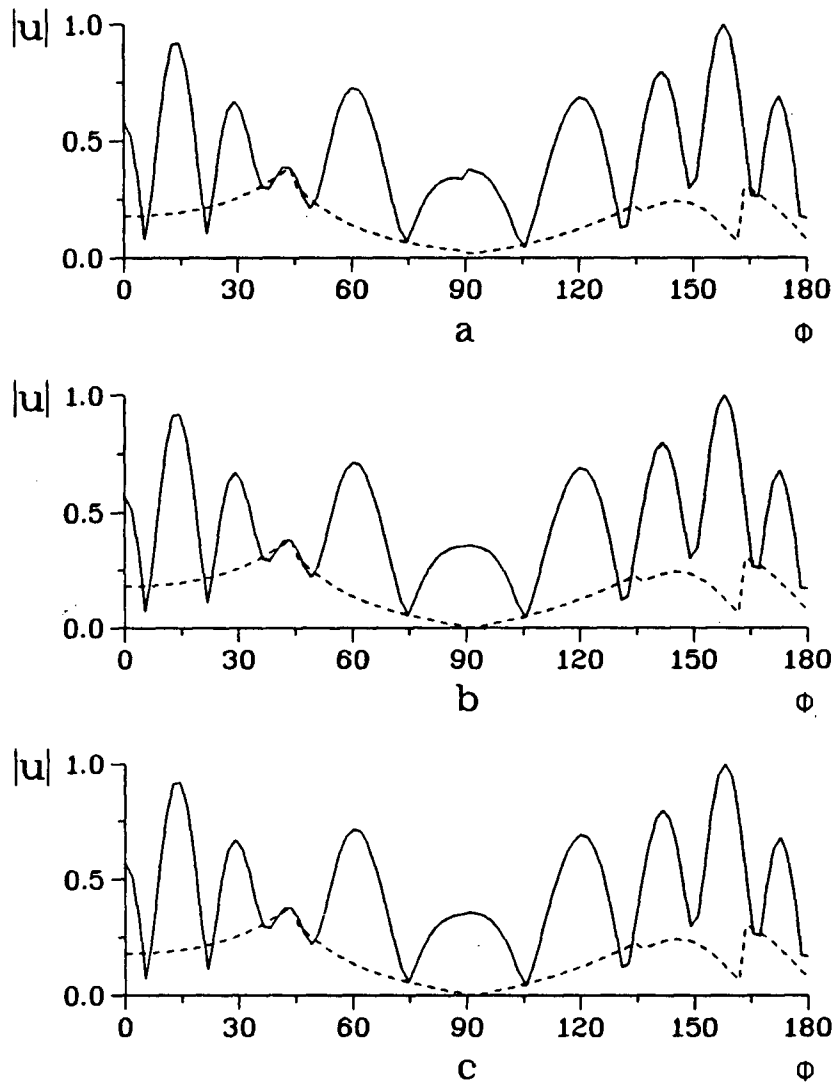
Figure 2.6: Total field and diffracted field from a step discontinuity of $h = \lambda$ illuminated by a point source at $\rho' = 1000\lambda$ and $\phi' = 135°$. Solid curves represent the total field, dashed curves represent the diffracted field. a: single diffraction; b: single and double diffraction; c: single, double and triple diffraction.

source at $\rho' = 1000\lambda$ for $\phi' = 45°$ and $\phi' = 135°$. In figure 2.5a, the total field includes geometrical optics fields and single diffractions; in figure 2.5b, the total field includes geometrical optics fields, single diffractions and double diffractions; in figure 2.5c, the total field includes geometrical optics fields, single, double and triple diffractions. In figure 2.5a, the total field has a discontinuity at $\phi = 90°$. When the doubly diffracted field is added, the total field is greatly improved, as shown in figure 2.5b. But triple diffraction is insignificant, as expected. The discontinuity at $\phi = 90°$ in figure 2.6a is caused by the shadow of the reflected single diffraction. On the right half plane, there are no reflections of singly diffracted field. On the left half plane, the singly diffracted field will be reflected by the lower boundary. This discontinuity is smoothed out by the doubly diffracted field emitted from the edge. Figure 2.5b and figure 2.5c is almost identical to each other. These results suggest that only singly and doubly diffracted fields are required here, triply diffracted fields are not significant. These results are for essentially plane wave incidence and thus may be compared with those of Soares and Giarola ([33], figures 3 and 4). Their results are virtually identical to figure 2.5a and figure 2.6a.

The behaviour of the diffracted field at shadow and reflection boundaries is also very interesting. In figure 2.5, the amplitude of the diffracted field reaches its maximum at the reflection boundary of the upper plane ($\phi = 135°$) and the reflection boundary of the lower plane ($\phi = 165°$). There are two components of singly diffracted fields. One is the diffraction directly from the edge and the other is the diffraction reflected by the lower plane. At the reflection boundary of the upper plane, the two diffractions are almost $90°$ out of phase (figure 2.7). Thus, the amplitude of the total single diffraction changes continuously across the reflection boundary. The two diffractions are almost $180°$ out of phase (figure 2.7) on the reflection boundary of the lower plane. This phase difference results in the amplitude discontinuity of the total diffraction on the reflection boundary.

Thus the total diffraction behaves differently on the two reflection boundaries.

Figure 2.8 shows the effect of step height h on the diffracted field at $\rho = 3\lambda$ for an essentially plane wave at normal incidence ($\rho' = 1000\lambda, \phi' = 90°$). In this situation, to the right of the edge, single diffraction from the edge is of equal magnitude but $180°$ out of phase of to doubly diffracted field. Thus, their sum to the right of the edge is zero. To the left of the edge, the diffraction is distant from the reflection boundary. Both single and double diffractions are very weak. For the same reason, the resultant total diffraction is zero to the left of the edge. From another point of view, the diffraction increases when the geometrical optics field has discontinuities. When h is one wavelength, the total reflection from the upper and lower planes is continuous (assuming the source is distant). Consequently, the total diffraction is very weak. But if 2h is not an integer of the wave length, the reflection to the right of the edge will be different in phase to the reflection to the left of the edge. Then, the diffraction will compensate for the difference of the total reflected fields. Thus, when $h = n\lambda/2 + \lambda/4$, $n = 1, 2 \cdots$, the diffraction is very weak, as in figure 2.8a (where n is an integer and $n\lambda/2 \ll \rho'$). But when $h = n\lambda/2$, $n = 1, 2 \cdots$, they are very strong, as in figure 2.8b. If the source is very close to the edge, the difference in amplitude of the reflections results in a difference in the total geometrical optics field, then the diffraction rises even with $h = \lambda$, figure 2.9c. For a given frequency then, the step height can have a major effect on the diffracted and total fields, particularly when the source and receiver are directly above it.

2.4 Time-Domain Results

For a time domain solution to this diffraction problem, the source must have weak low frequency components and be similar to sources used in the geophysical literature so that

comparisons may be made. A convenient source function is

$$f(t) = \frac{\sin[\omega_1(t - t_0)]}{\sqrt{|t - t_0|}} \exp[-a(t - t_0)^2], \tag{2.36}$$

which is illustrated in figure 2.10a for $\omega_1 = 20\sqrt{\pi}\mathrm{rad/s}$, $a = 2.2 \times 10^3$ and $t_0 = 0.1\mathrm{s}$. Its amplitude spectrum peaks at about 35 Hz and its low frequency amplitudes are small, figure 2.10b. The time domain solution is the convolution of the Fourier transformation of the incident, reflected and diffracted fields given earlier with the pulse signal $f(t)$.

The dimensions of the model chosen correspond to those of Hilterman [3] who obtained numerical results by Kirchhoff diffraction theory as well as experimental results for a scale model. The dimensions modeled are a step height of $h = 400m$ and source and receiver locations at a height of 4000m above the upper surface, figure 2.11. The velocity is 4000m/s.

Figure 2.12 shows results for source and receiver together at 200m intervals along the horizontal scale indicated by the 41 vertical traces. At $x = 0$, $\phi' = \phi = 90°$ and at $x = \pm 4000m$, $\phi = \phi' = 45°$ or $135°$. The two large amplitude horizontal events represent reflections from the upper the lower horizontal boundaries. The large amplitude event on the left side of figure 2.12, which appears to be hyperbolic, indicates reflections from the corner. The corresponding ray path is shown as S_3 in figure 2.2c for offset source and receiver. With zero offset the path is the line connecting the source and receiver pair and the corner.

The weaker hyperbolic events in figure 2.12 which decrease in amplitude with increasing time of arrival represent diffracted pulses. These diffracted pulses are reprinted in figure 2.13b to figure 2.13d. Single diffraction and double diffraction are shown in figure 2.13b and figure 2.13c. For the purpose of comparison, the triple diffraction is shown in figure 2.13d. From these results, diffraction events can easily be identified. The first to arrive in figure 2.13b are singly diffracted from the edge and are represented by the

upper hyperbolic event. This diffraction has a phase change at the reflection boundary at $\phi' = \phi = 90°$ in order to compensate for the discontinuity of the reflections. The next to arrive, which start to the left of the edge, are the sum of two events — the diffraction of the reflected pulse from the lower plane and the reflection of the edge diffracted pulse. These events merge with the corner reflections on the left side of figure 2.13a. The third diffraction is the one which experienced twice reflection from the lower boundary and once diffraction from the edge. The reflected single diffraction and singly diffracted reflection are discontinuous at the boundary $\phi' = \phi = 90°$. This discontinuity is compensated for by the double diffractions shown in figure 2.13c. The discontinuity of the second event in the double diffraction will be compensated for by the triple diffraction in figure 2.13d, which is very weak in figure 2.12. Higher order diffractions can be included, but they are insignificant. The triple diffraction shown here is not evident in Hilterman's measured results. In order to record the extremely weak triple diffraction, the test equipment must have a dynamic range greater than $80dB$. In figure 2.14, the amplitude is in dB scale with a dynamic range of $80dB$. In this image the triple diffraction on the left of the last event is quite visible but in practice, these weak triple diffractions will be buried in the background noise unless some special signal processing measure is taken.

A comparison of figure 2.12 with Hilterman's results ([3], figure 11) shows that our numerical model accounts for corner reflection and successive diffraction and reflections apparent in Hilterman's observations but absent from his calculated results. In addition, the relative amplitude of the singly diffracted field should be more accurately predicted. This cannot be observed from the data here as different pulses are used, but is known from the inherent limitations of the Kirchhoff approximation, which cannot reproduce its own boundary condition on the surface. The geometrical theory of diffraction can, to essentially any degree of accuracy required, by the inclusion of successive diffraction. Figure 2.15 shows the measured result of acoustic scattering by a step discontinuity by

Mellema [43]. A median filtered result is shown in figure 2.16. These results verified the theoretically predicated single and double diffraction. As discussed earlier, the triple diffraction does not appear in the measured result even with the help of the filtering technology.

Figure 2.18a shows results obtained when the vertical portion of the step in figure 2.11 is removed leaving two parallel half-planes with their edges aligned and separated by h=400m. For a half-plane the diffraction coefficient and consequently the singly diffracted fields in figure 2.18a are exact. Those from the upper edge are represented by the pulses with arrival times tracing a hyperbola with its apex coinciding with reflection from the upper edge in figure 2.17a. In figure 2.12 and figure 2.18a the pulses are asymmetric in amplitude about the axis of the hyperbola and reverse in phase as the source-receiver pair passes over the edge. Kirchhoff diffraction theory predicts pulse amplitudes symmetric about the hyperbola axis ([1], figure 13). Consequently, migration or inversion of the data of figure 2.12 and figure 2.18a with Kirchhoff theory will not collapse the diffraction hyperbolas and may give poor results. For real seismic data with elastic media and nonrigid boundaries, this may not be observed however.

As the source and receiver position moves to the left of the discontinuity in figure 2.17a the arrival times of diffracted pulses from the upper and lower edges converge, but as they differ in phase, here the amplitude of the resultant hyperbolic event is not noticeably increased. On the right side of figure 2.18a the second or lower hyperbolic event represents double diffraction by the two edges and therefore is weaker than the corresponding event on the left side.

The numerical results in figure 2.18b for zero offset between source and receiver are for the 30° incline to the step, figure 2.17b. To obtain these values the preceding theory must be modified to include a 150° wedge at the upper edge and a 210° wedge angle at the lower. Consequently, edge diffracted fields are weaker than in the previous examples, and

doubly diffracted fields, although they are included, are scarcely evident. Also a reflected pulse from the inclined step is apparent with source and receiver at $\phi' = \phi = 120°$. In Hilterman's numerical model for his case ([3] figure 12) these features also appear, but for $\phi' = \phi = 90°$ the diffracted pulse amplitudes appear to be weaker than those observed, and those in figure 2.13.

The parameters in figure 2.19 for a 90° step are the same as those in figure 2.13 but source and receiver are separated. In figure 2.19a the source is at $x' = 4000m$. and the receiver position is indicated by the horizontal coordinate. For $\phi < 135°$ a strong reflected pulse is received first, followed by weaker singly diffracted and still weaker doubly diffracted pulses from the edge. At $\phi = 135°$ (x=-4000m) the singly diffracted fields from the edge are reflected from the lower boundary producing an enhanced return which merges with the doubly diffracted field in figure 2.19a.

The source is directly above the edge in figure 2.19b and thus reflected and diffracted fields merge for $\phi = 90°$, but, as the receiver moves away from the edge, the arrival time of reflected as well as diffracted pulses increases. In figure 2.19c the source is at $x' = -4000m$, ($\phi' = 135°$) and when the receiver is nearby ($\phi = 135°$) corner reflected pulses are observed. Pulses which are successively reflected and diffracted are observed for $135° > \phi > 90°$. At $\phi = 45°$ reflection from the upper plane appears first as reflection from the lower plane is shadowed by the edge.

2.5 Conclusion

The uniform geometrical theory of diffraction has been applied to seismic modelling of acoustic pulse diffraction by planar structures with edges. Here, some defects in previous mathematical models based on the Kirchhoff method are noted. These include the omission of corner reflection and limited accuracy in the singly diffracted pulses.

Geometrical diffraction theory is ideally suited to the inclusions of these delayed returns. In addition, its use in inverting seismic data may avoid errors inherent in using Kirchhoff theory.

Computational efficiency is also a significant advantage to this approach. In Hilterman's paper [3], only the zero offset case can be calculated. The solution given here can handle the non-zero offset case without any computational difficulty. These uniform frequency domain solutions are in the form of Fresnel integral readily computed by efficient subroutines. Increased computational advantage is also possible because analytical expressions are available for the Fourier transforms of Fresnel integral. Geometries more complex than these may well require their use. Solutions for complex geometries can be constructed by superposition of solutions of simple structures. For example, a solution for the rectangular ridge would be the superposition of solutions for two vertical steps and interaction between the edges would be added for narrow ridges.
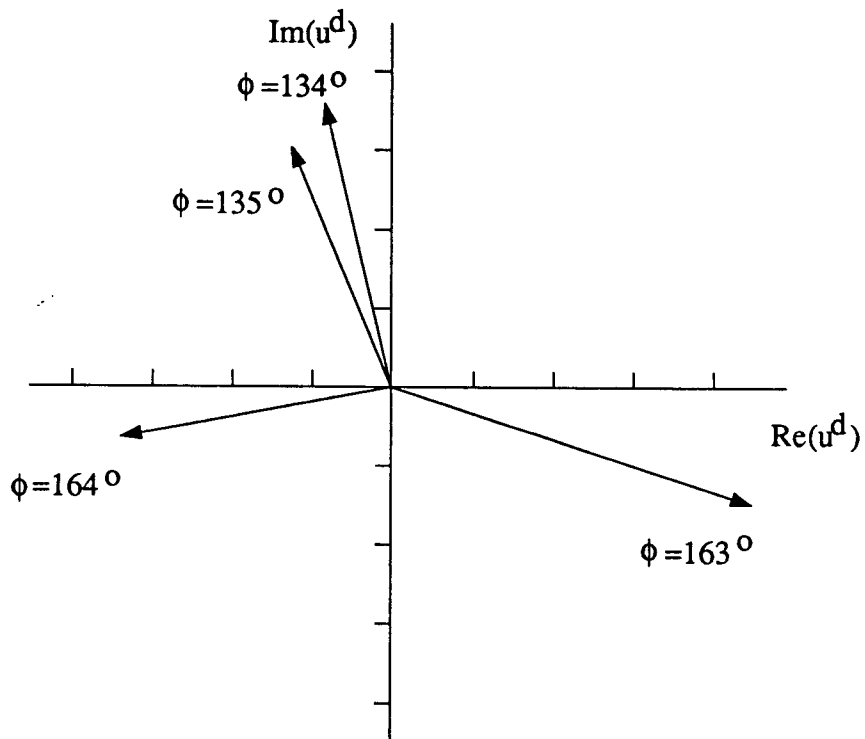
Figure 2.7: Single diffraction at and near reflection boundaries. The arrows show the amplitude and phase of the sum of the two components of singly diffracted fields for the parameters of figure 2.5.
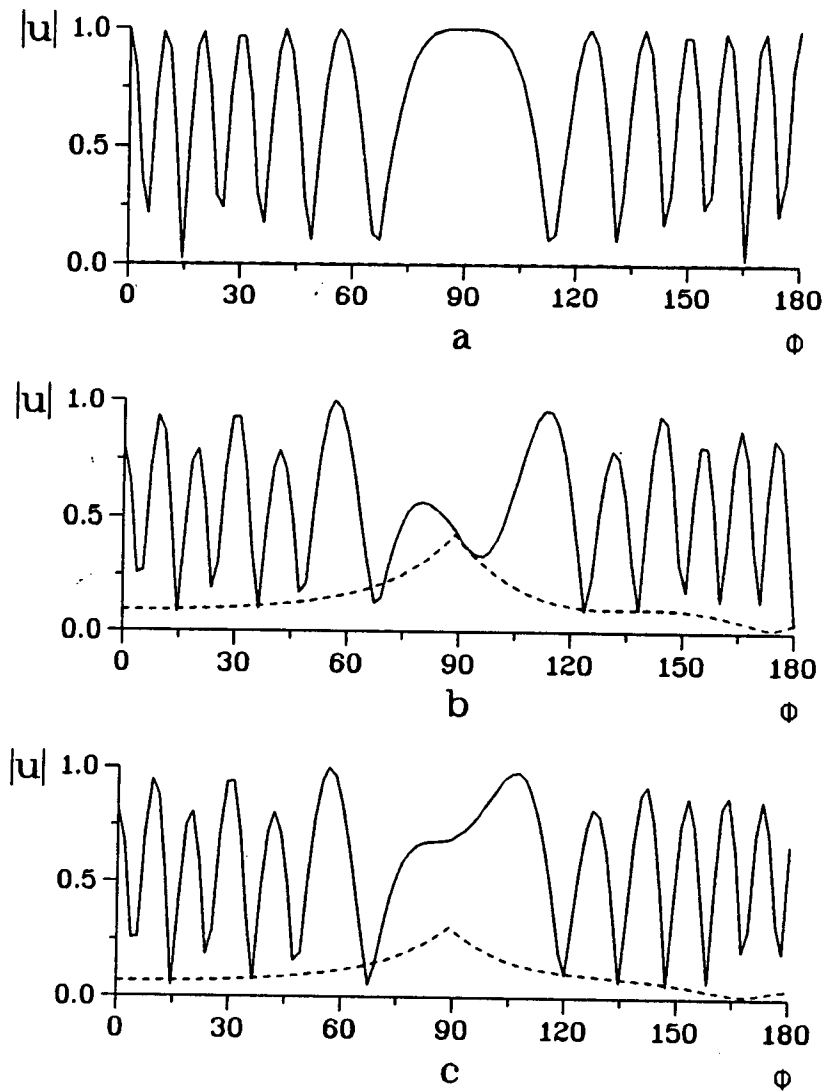
Figure 2.8: The effect of change of step height h on the diffractions. A point source is located at $\rho' = 1000\lambda$ and $\phi' = 90°$. Solid curves represent the total field; dashed curves represent the diffracted field. a: $h = 1\lambda$, b: $h = 0.75\lambda$, c: $h = 0.625\lambda$.
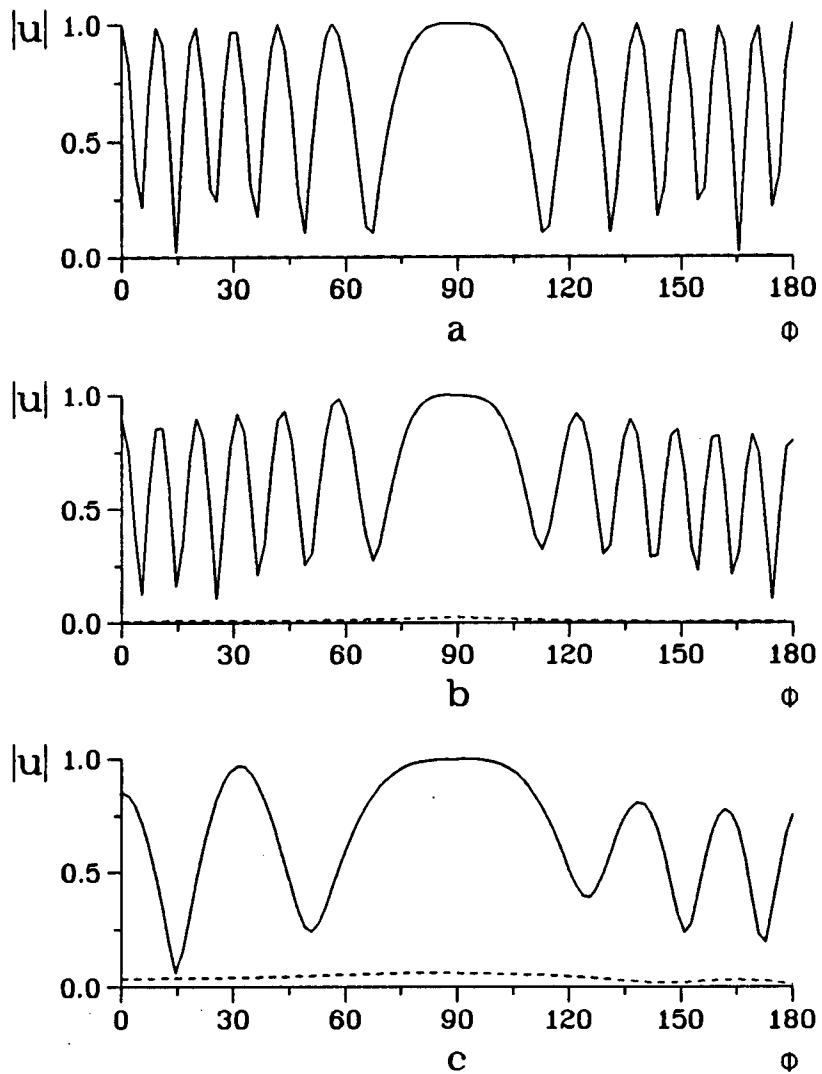
Figure 2.9: The effect of change of source position on the diffractions. Solid curves represent the total field; dashed curves represent the diffracted field. Step height h=λ, $\phi' = 90°$. a: $\rho' = 1000\lambda$, b: $\rho' = 10\lambda$, c: $\rho' = \lambda$.
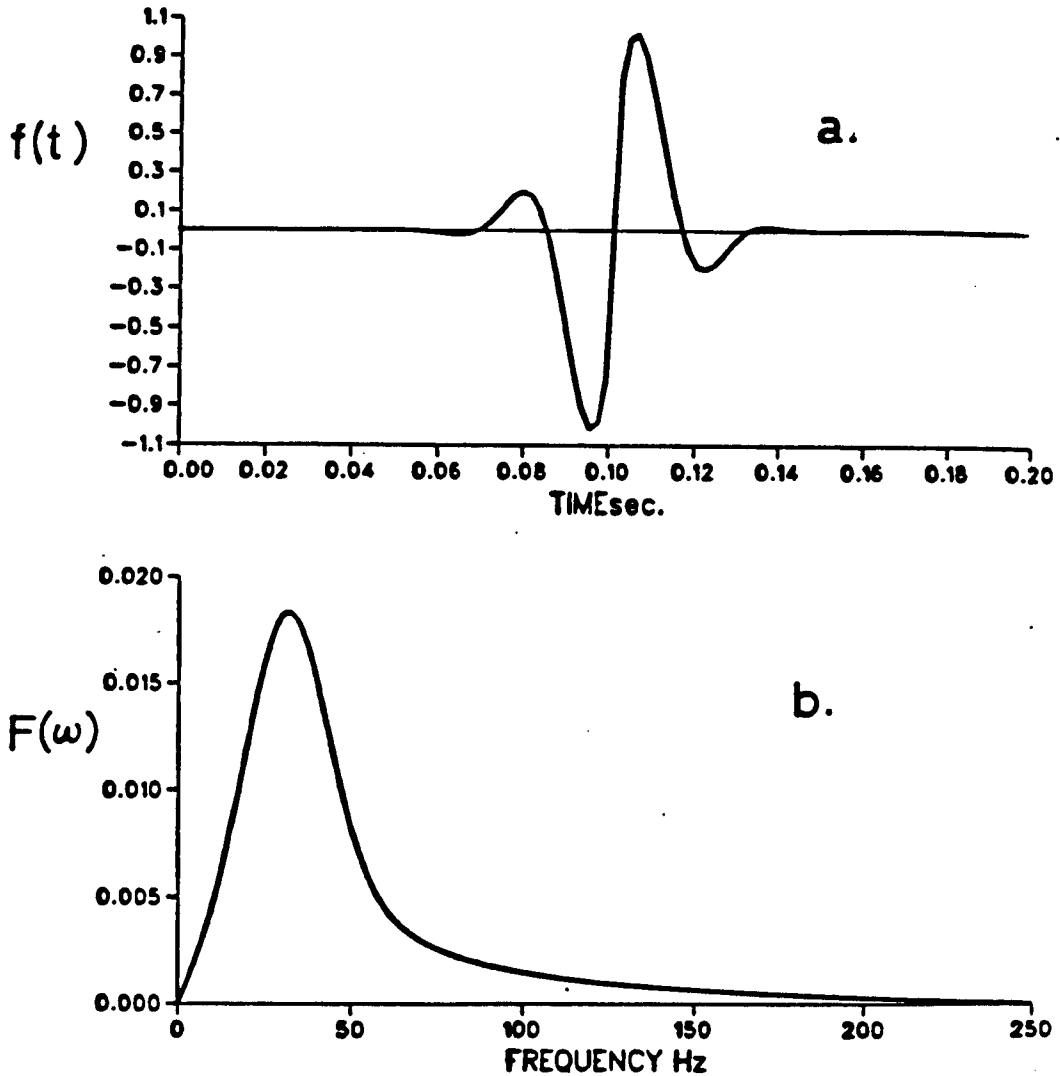
Figure 2.10: Pulse function used to construct the time-domain diffraction image. a: time-domain pulse; b: spectrum amplitude.
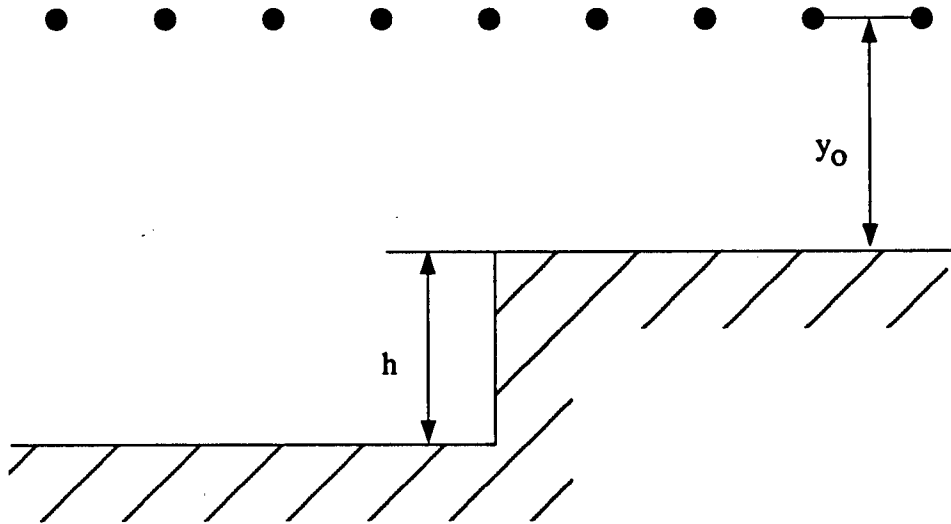
Figure 2.11: Source and receiver array over a step discontinuity.
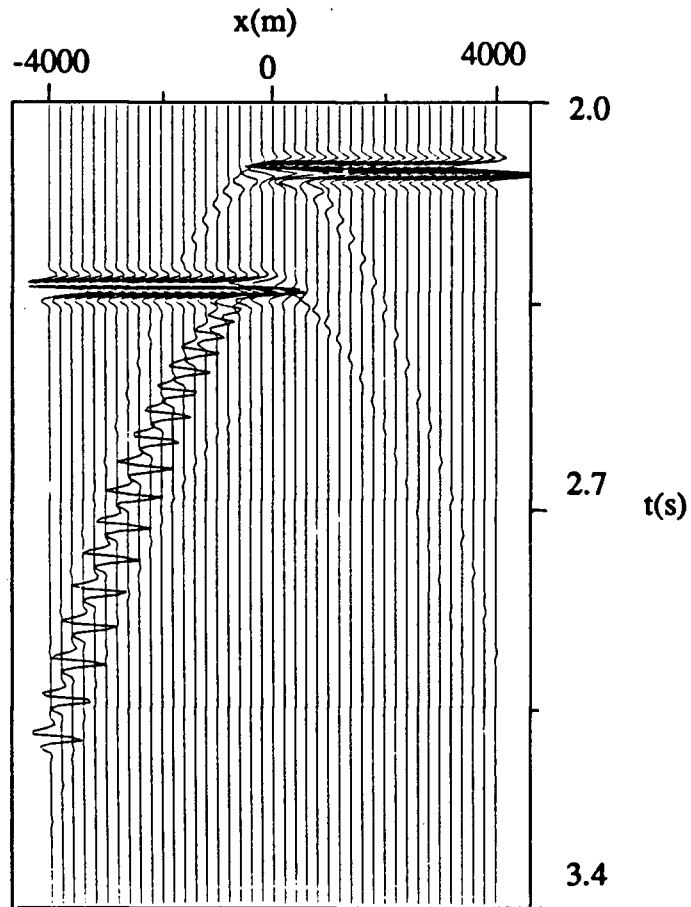
Figure 2.12: Pulse diffraction by a step discontinuity. Source and receiver array is located at $y_0 = 4000$m, from $\phi' = 45°$ to $\phi' = 135°$, with a 200m interval. The velocity of the pulse is 4000 m/s.
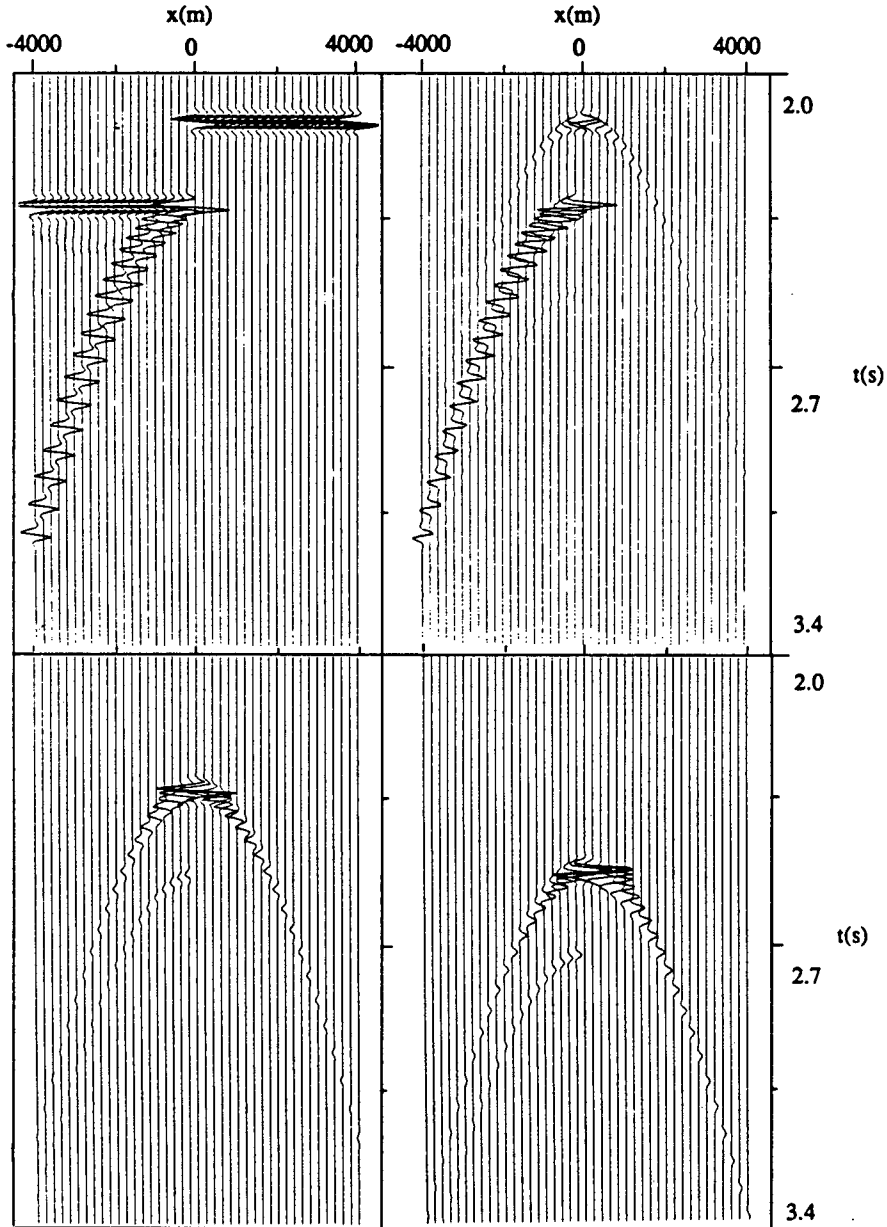
Figure 2.13: Reflection and diffraction from a step discontinuity normalized to maximum amplitude. a: reflection; b: single diffraction; c: double diffraction; d: triple diffraction. Parameters are same as figure 2.12.
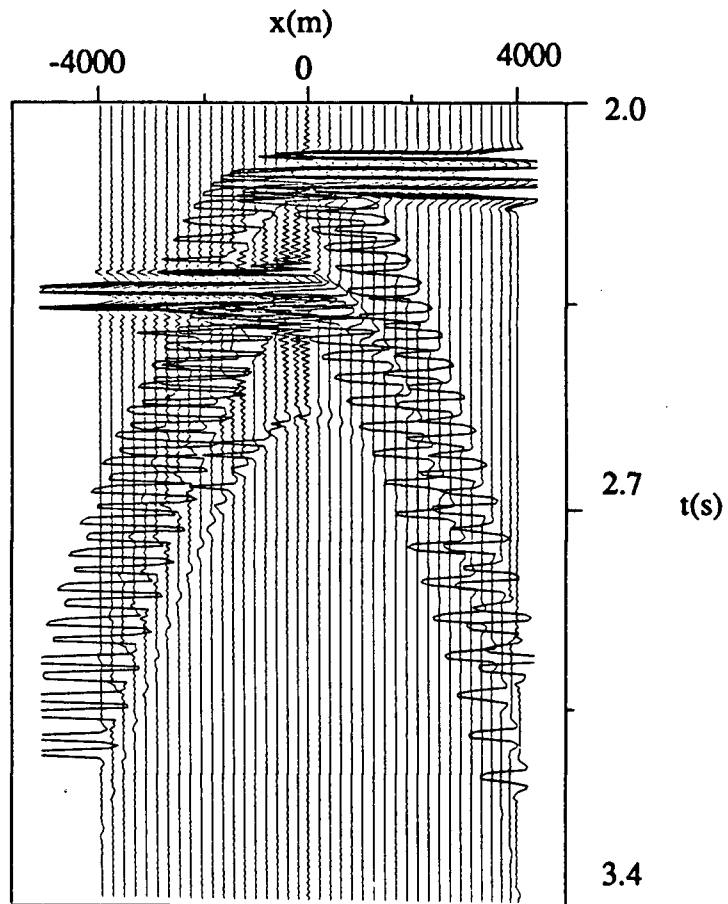
Figure 2.14: Pulse scattering by a step discontinuity in a logarithm scale. Parameters are same as figure 2.12.
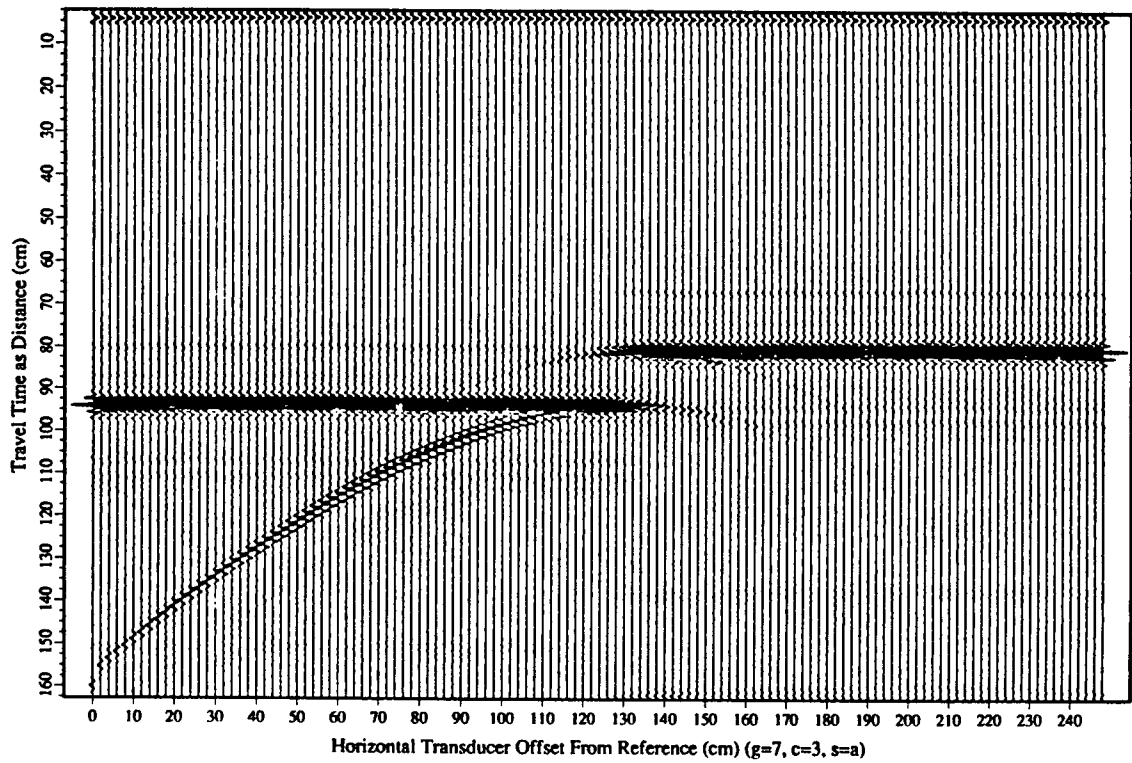
Figure 2.15: Measured acoustic scattering by a step discontinuity. Courtesy of Mellema [43].
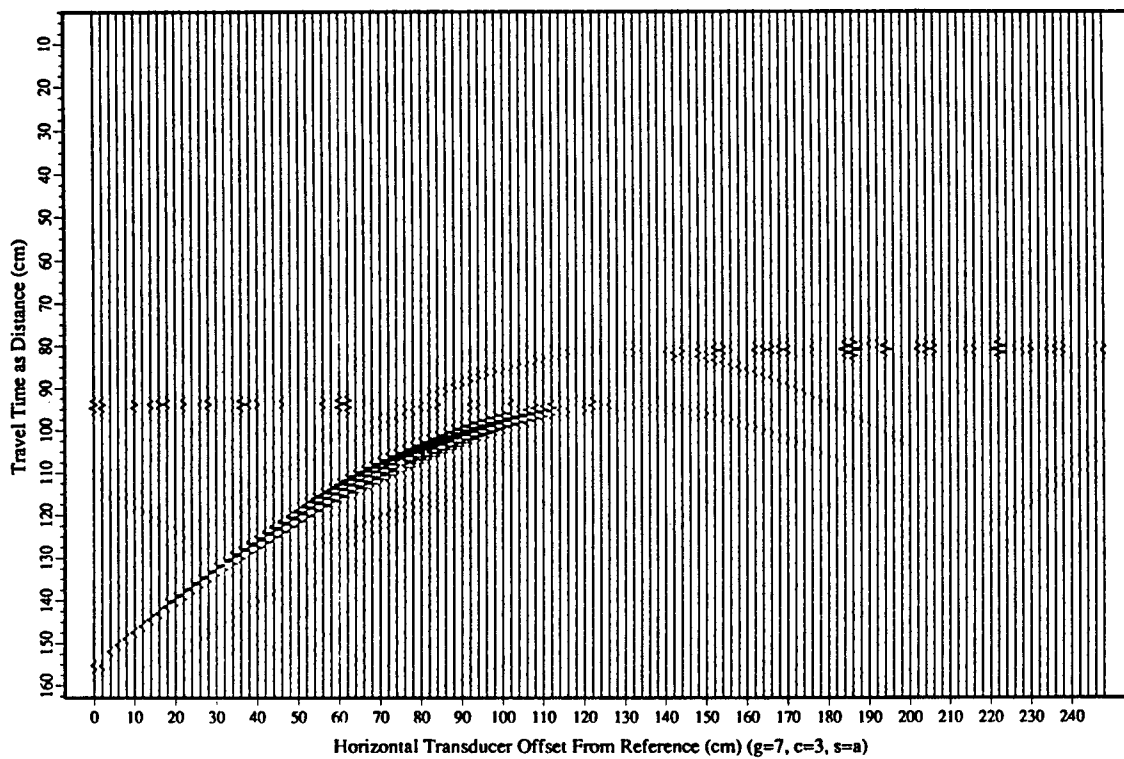
Figure 2.16: Median filtered results of figure 2.15 for acoustic scattering by a step discontinuity. Courtesy of Mellema [43].
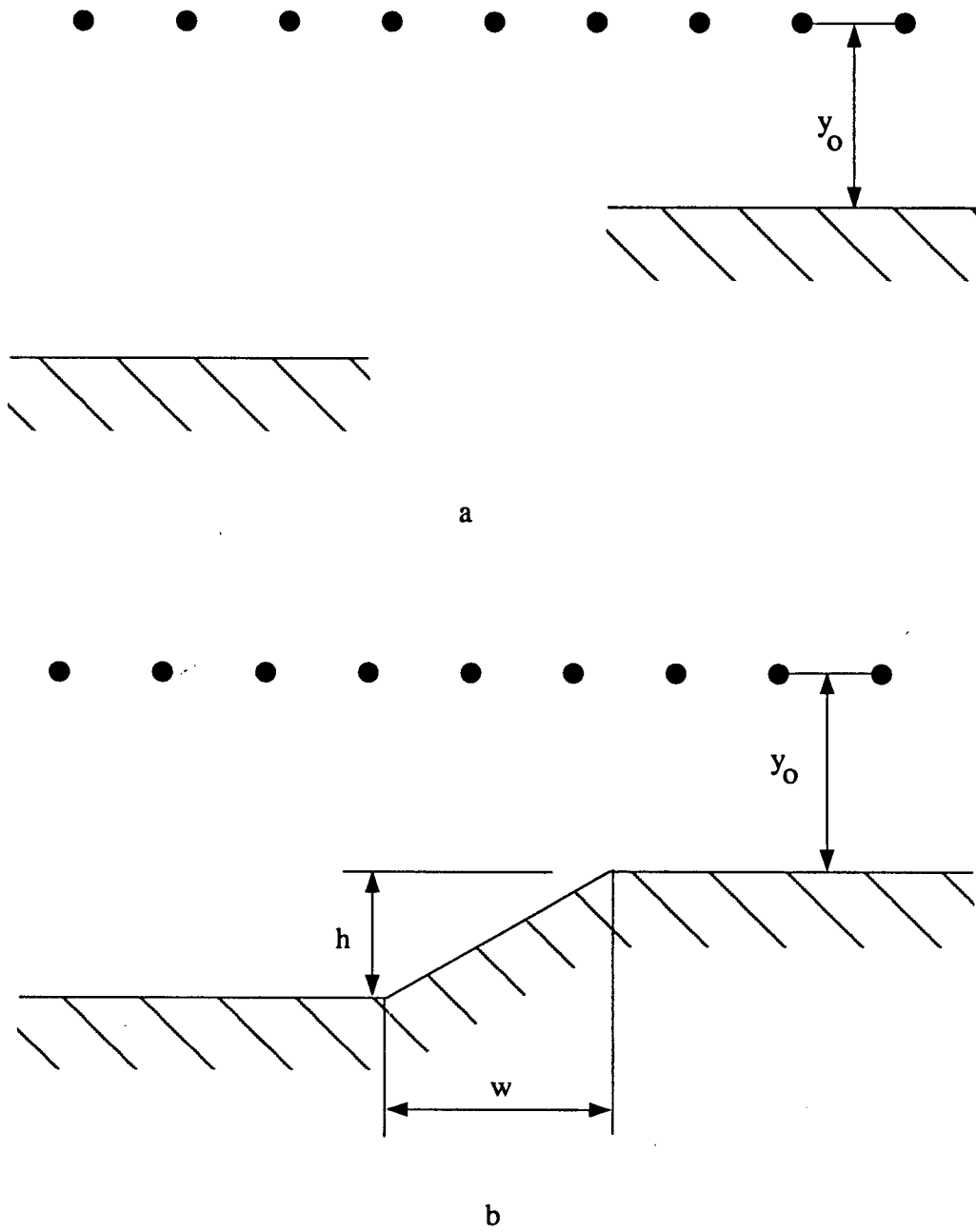
Figure 2.17: Two offset half-planes and an inclined step. a: two offset half-planes; b: a 30° inclined step.
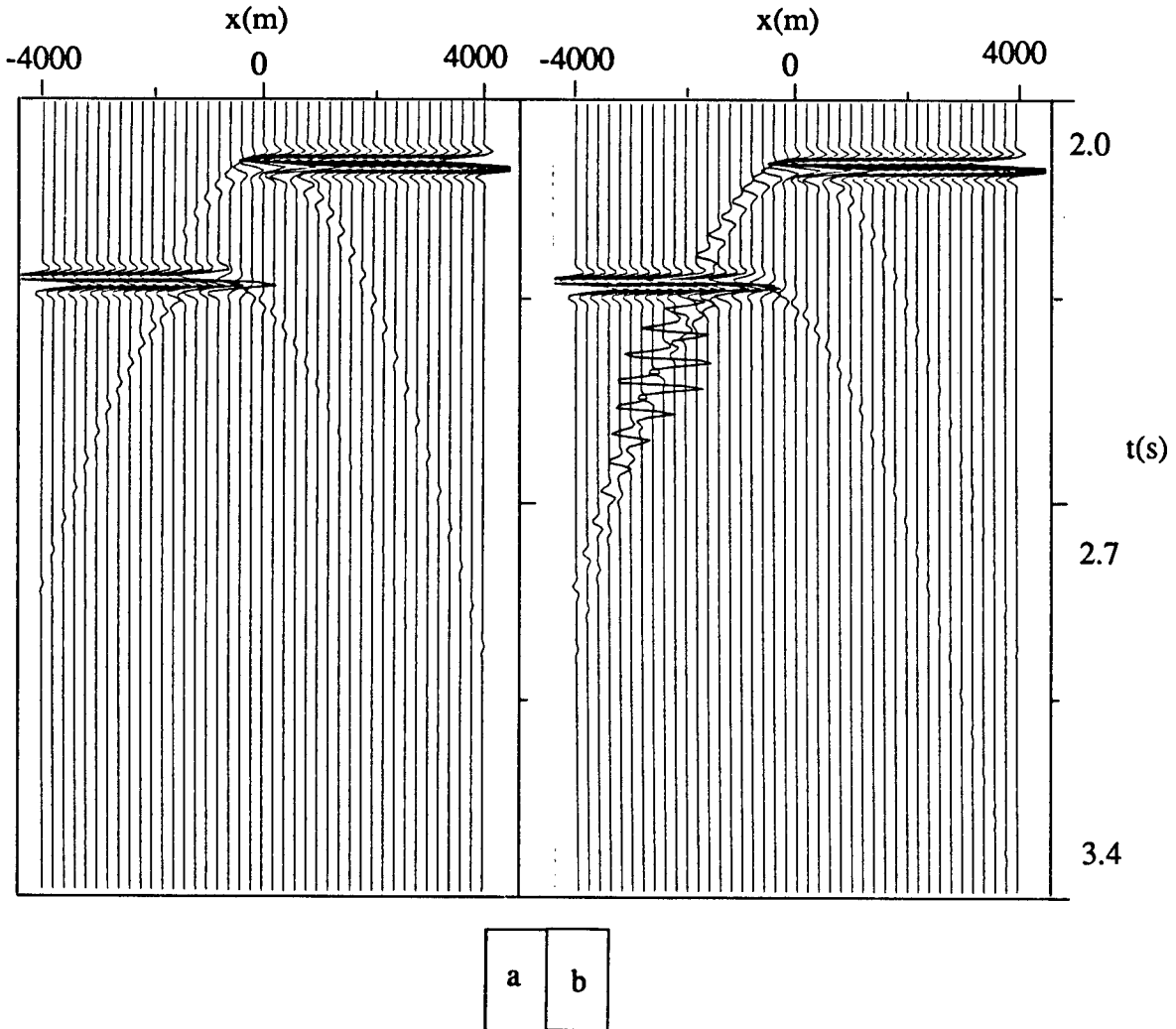
Figure 2.18: Reflection and diffraction from two offset half-planes and an inclined step. a: received pulse from above of two offset half-planes; b: received pulse from above of an inclined step. $h = 400m$, $w = 692m$.
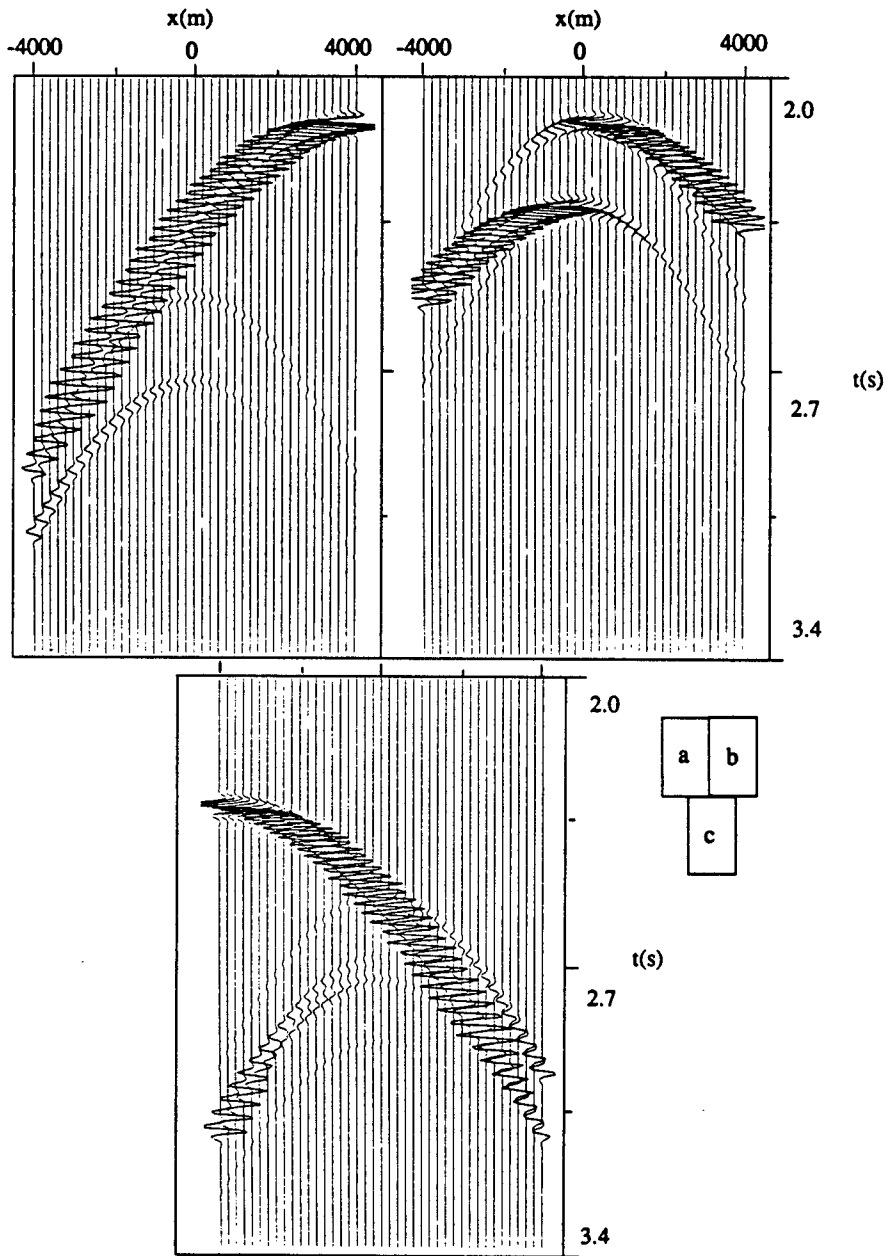
Figure 2.19: Received pulses for a non-zero offset source and receiver array over a normal step discontinuity. a: $\phi' = 45°$; b: $\phi' = 90°$; c: $\phi' = 135°$.

Chapter 3

BEAM DIFFRACTION BY A STEP DISCONTINUITY

3.1 Introduction

Beam sources are widely used in optics, antennas, acoustics and a Gaussian beam is the most frequently used representation of the main beam pattern. The propagation of the Gaussian beam can be tracked from the source to the observation point by the method of evanescent wave tracking. Examples of this are the study of Gaussian beam propagation through a lens-like medium by Choudhary and Felsen [51], and the complex ray tracing of an evanescent plane wave scattering by a conducting circular cylinder by Wang and Deschamps [52]. When dealing with spherical Gaussian beam diffraction by conducting edges, the wave tracing process is very complicated. However, using the complex source point method, beam solutions can be directly obtained from the solution for omnidirectional source. The beam can also be traced through propagation and scattering configurations by analytic extension into complex space of the rules pertaining to rays in real space. In this chapter, the complex source point method is used to generalize solutions of the step discontinuity diffraction. This approach dramatically simplifies the analysis of the problem. The behaviour of the diffracted field at and near the reflection boundary is also examined.

3.2 Complex Source Point Method

Complex rays were first used by Keller and Streifer [53] to study the propagation of

a beam with a Gaussian profile. They pointed out that the complex ray is also the

leading term in a high frequency asymptotic expansion of the exact field solution. The

comparison study of the complex ray method and the stationary phase method was

conducted with the conclusion that both methods yield the same result with the complex

ray method being much simpler. This complex ray representation of the beam source

greatly facilitates the analysis of the reflector antennas with tapered illumination. A

general representation of a Gaussian beam as a bundle of complex rays was given by

Deschamps [54]. He verified that a Gaussian beam can be described paraxially in terms of

a Green function in free space with a complex source position. Using this representation,

solutions of reflection, refraction and diffraction for a point source at a real location can

be transferred to solutions for a beam source. This method greatly simplifies the analysis

of beam scattering and extends the power of the various methods which are based on

the solutions of the real point sources. For a beam source, the focus and transition

region problem encountered by the ray method can also be avoided in some parameter

ranges [55]. A thorough study and some excellent examples of the beam patterns of the

complex position source have been given by Suedan and Jull [34]. An exact solution of

the wave equation in time-space coordinates with a complex source location was obtained

by Ziolkowski [56]. The extensions of this solution may yield other physically interesting

wave equation solutions. This space-time investigation was further carried out by Einziger

and Raz [57]. Their solutions can be used as basis functions for generalized space-time

field representations.

In the following applications of the complex source point method, the behaviour of the

transition function for the complex source is examined. Then the solution to a real source

diffraction by a step discontinuity is extended to the solution for a complex source. This extension includes modifying the program to handle the Fresnel integral with a complex argument and the recalculation of the reflection and shadow boundaries.

An incident wave from a point source at a complex location $\bar{\rho}'$ can be expressed as [58]

$$u^i = \frac{\exp(-jkR)}{R}, \tag{3.37}$$

where

$$R = |\bar{\rho} - \bar{\rho}'|. \tag{3.38}$$

If the beam axis is in the x-y plane, by using polar coordinates with β defining the orientation of the beam as shown in figure 3.20, it can be shown

$$\rho' = \sqrt{(\rho_r{}')^2 + 2\rho_r'(-jb)\cos(\beta - \phi_r') - b^2} \tag{3.39}$$

and

$$\phi' = \arccos\left[\frac{\rho_r' \cos \phi_r' - jb \cos \beta}{\rho'}\right], \tag{3.40}$$

where ρ' and ϕ' are complex now. The original real ϕ' and ρ' are denoted by ϕ_r' and ρ_r'. When $|\rho| \gg |\rho'|$,

$$R \doteq \rho - \rho' \cos(\phi - \phi'), \tag{3.41}$$

the incident wave can be simplified to

$$u^i = \frac{\exp\{-jk[\rho - \rho_r' \cos(\phi - \phi_r')]\}}{\rho} \exp[kb \cos(\phi - \beta)]. \tag{3.42}$$

The directivity of the beam is determined by the factor kb and the direction of the beam axis is determined by the angle β. The 3dB beam band width is given by

$$HPBW = 2 \arccos(1 - \tfrac{ln2}{2kb}), \qquad kb \geq \tfrac{ln2}{4}. \tag{3.43}$$

The beam patterns for different *kb*s are shown in figure 3.21. Since the directivity of
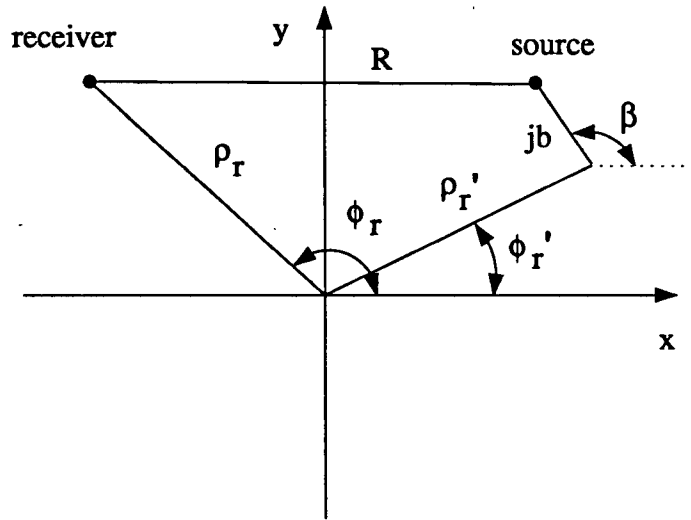
Figure 3.20: A point source at a complex location.
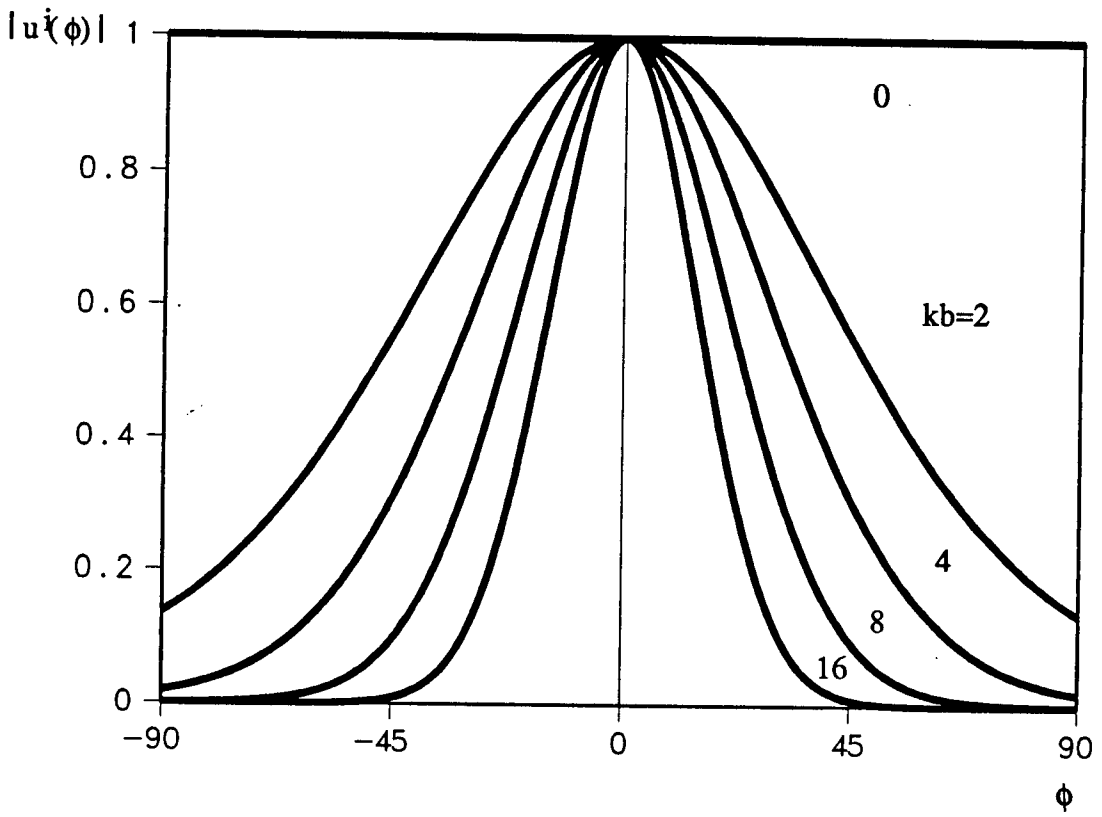
Figure 3.21: Normalized beam patterns for kb=0, 2, 4, 8, 16 from (3.42) with $\beta=0$. After Suedan [58].

the beam generated by a complex position source is determined by the factor kb, Special attention must be paied to the fact that the beam pattern is a function of frequency. The influence on the beam pattern by the propagation constant k and the parameter b is the same. For a narrow band signal, this will not present any significant difference, but for a wide band pulse this can not be overlooked. Most antenna feeders and acoustic sources have higher directivity at higher frequency and lower directivity at lower frequency. In any case, care must be taken when the complex source point method is used to model real beam sources. The parameter b should always match the beam pattern at the operating the frequency. In the following studies, the real source directivity will not be concerned. It can be incorporated into solutions by assigning a different parameter b at a different frequency.

3.3 Shadow and Reflection Boundary

A beam generated by a complex position source has distinct properties. The shadow and reflection boundary positions are different from their positions for a real source. The boundaries are straight lines for a real position source, while they are curved lines for a source in a complex position. This property has been investigated by Green et al [55]. The shadow and reflection boundaries can be found from the saddle point contribution in the integral representation of the wave equation solution. Here these results are adopted for a complex point source with a conducting wedge.

The shadow boundary cast by an edge is located by $\text{Re}(W_s) = 0$ [55], [34], where

$$W_s = -2 \exp(j\frac{\pi}{4})\sqrt{\frac{k\rho\rho'}{\rho + \rho' + R}} \cos(\frac{\phi - \phi'}{2}). \qquad (3.44)$$

In the lit region $\text{Re}(W_s) < 0$ and in the shadow region $\text{Re}(W_s) > 0$. The reflection

boundary is given by $\text{Re}(W_r) = 0$ with

$$W_r = -2\exp(j\frac{\pi}{4})\sqrt{\frac{k\rho\rho'}{\rho + \rho' + R}}\cos(\frac{\phi + \phi'}{2}). \tag{3.45}$$

In the lit region $\text{Re}(W_r) < 0$ and in the shadow region $\text{Re}(W_r) > 0$. Thus, the step functions in equation 2.12 to equation 2.15 can be replaced by the following equations. For the shadow boundary,

$$\begin{aligned} U(\pi + \phi' - \phi) &= U[-\text{Re}(W)] \\ W &= -2\exp(j\pi/4)\sqrt{\frac{k\rho\rho'}{\rho + \rho' + R}}\cos(\frac{\phi - \phi'}{2}). \end{aligned} \tag{3.46}$$

And for the reflection boundary of the upper half-plane,

$$\begin{aligned} U(\pi + \phi' + \phi) &= U[-\text{Re}(W_1)] \\ W_1 &= -2\exp(j\pi/4)\sqrt{\frac{k\rho\rho'}{\rho + \rho' + R_1}}\cos(\frac{\phi + \phi'}{2}). \end{aligned} \tag{3.47}$$

The reflection boundary of the lower half-plane is given by

$$\begin{aligned} U(\pi - \Phi_1) &= U[-Re(W_2)] \\ W_2 &= \begin{cases} 1, & \text{if } \phi \text{ and } \phi' < \frac{\pi}{2} \\ -2\exp(j\pi/4)\sqrt{\frac{k\rho_i\rho'}{\rho_i + \rho' + R_2}}\cos(\frac{\Psi_2 - \phi'}{2}), & \text{if } \phi > \frac{\pi}{2} \text{ and } \phi' < \frac{\pi}{2} \\ -2\exp(j\pi/4)\sqrt{\frac{k\rho\rho'}{\rho + \rho' + R_2}}\cos(\frac{\frac{3}{2}\pi - \phi - \Psi_2'}{2}) & \text{if } \phi' > \frac{\pi}{2}. \end{cases} \end{aligned} \tag{3.48}$$

The reflection from the corner is bound by three factors, they can be put together as

$$U(\phi' - \frac{\pi}{2})U(\phi - \Phi_2)U(\Phi_3 - \phi) = U[-Re(W_{31})]U[-Re(W_{32})]$$

$$W_{31} = -2\exp(j\pi/4)\sqrt{\frac{k\rho\rho_i'}{\rho + \rho_i' + R_3}}\cos(\frac{\Psi_{31} + \Psi_{31}'}{2})$$

$$W_{32} = -2\exp(j\pi/4)\sqrt{\frac{k\rho_i\rho'}{\rho_i + \rho' + R_3}}\cos(\frac{\Psi_{32} + \Psi_{32}'}{2}). \tag{3.49}$$

In the above equations, the angles are defined below

$$\Psi_2 = \sin^{-1}(\frac{y + 2H}{\rho_i}) \quad \Psi_2' = \sin^{-1}(\frac{y' + 2H}{\rho_i'})$$

$$\Psi_{31}' = \cos^{-1}(\frac{y' + 2H}{\rho_i'}) \quad \Psi_{31} = \frac{3}{2}\pi - \phi$$

$$\Psi_{32}' = \frac{3}{2}\pi - \phi' \quad \Psi_{32} = \cos^{-1}(\frac{y + 2H}{\rho_3}). \tag{3.50}$$

The distance parameters R, S_1, S_2 and S_3 are still given by equations 2.19 to 2.22, but they are complex. ρ_i and ρ_i' are given by equations 2.25 and 2.28. Here, ρ_i' is also complex. The complex coordinates of the source point are given by

$$x' = \rho' cos\phi'$$

$$y' = \rho' \sin \phi'. \tag{3.51}$$

In the above representation, the form used for a real source position is still kept. In this way changes of the formula of the diffraction solution for a real source position can be avoided. However, it should always be kept in mind that these complex variables have a different content from those of the real source position.

3.4   Transition Function F(w)

By analytic continuation into complex space, the UTD method can be extended to the case of a complex source position. The parameters in equation 1.5 should be extended to include a complex source position. In equation 1.8 and equation 1.9,

$$2n\pi N^{\pm} - \text{Re}(\phi \pm \phi') = \pm\pi. \tag{3.52}$$

Substituting the above equations into equations 2.23, 2.24 and 2.27, the solution of a beam source diffraction by a step discontinuity can be obtained.

Before the UTD method is applied to the step discontinuity diffraction with a beam source, the behaviour of the transition function $F(w)$ (defined by equation 1.6) will be examined inside and outside of transition regions. For a real position source, the transition function $F(w)$ provides a zero point at $w = 0$ to compensate for the singularity in the GTD diffraction coefficients at the shadow or reflection boundary. Away from the shadow and reflection boundaries, $F(w)$ approaches to unity as w approaches to infinity.

At the reflection and shadow boundaries, the GTD formula is not valid because of singularities in the GTD diffraction coefficient. When the source position is complex, the incident angle ϕ' also becomes complex (if the source is not pointed to the edge) and the singularity in the GTD diffraction coefficient is removed [55]. For some parameters, the GTD diffraction coefficient can be used in the transition regions, but for most applications the complex source position does not ensure the accuracy of the GTD diffraction coefficient in the transition regions [34]. The accuracy is determined by the orientation and the directivity of the incident beam. The transition function $F(w)$ can be used to show the difference between the GTD and UTD.

In figure 3.22 for different values of kb and incident angle β, a three dimensional plot of the transition function $F(w)$ is shown in the region $0 \leq \phi \leq \pi/2$, for a point source at $\phi_r' = 135^o$ and $\rho_r' = 50\lambda$. The reflection boundary is $\phi = 45^o$ for a real positioned source. In figure 3.22, the source is pointed in the y-direction, with different values of kb. When $kb = 0$, ϕ' and ρ' are real. $F(w)$ is zero at $\phi = 45^o$. This zero will compensate for the singularity in the GTD formula. $F(w)$ approaches unity when the receiver is distant from the reflection boundary. If the surface of $F(w)$ is cut by planes parallel to the x-y plane, the contours obtained will be parabolas with foci at the edge and axis along the reflection boundary. With $kb > 0$ the source position is complex, $|F(w)| \neq 0$ and the locus of min $|F(w)|$ becomes a curve about which the above parabolas are bent. Figure 3.23 shows the transition functions when the beam is pointed in the x direction
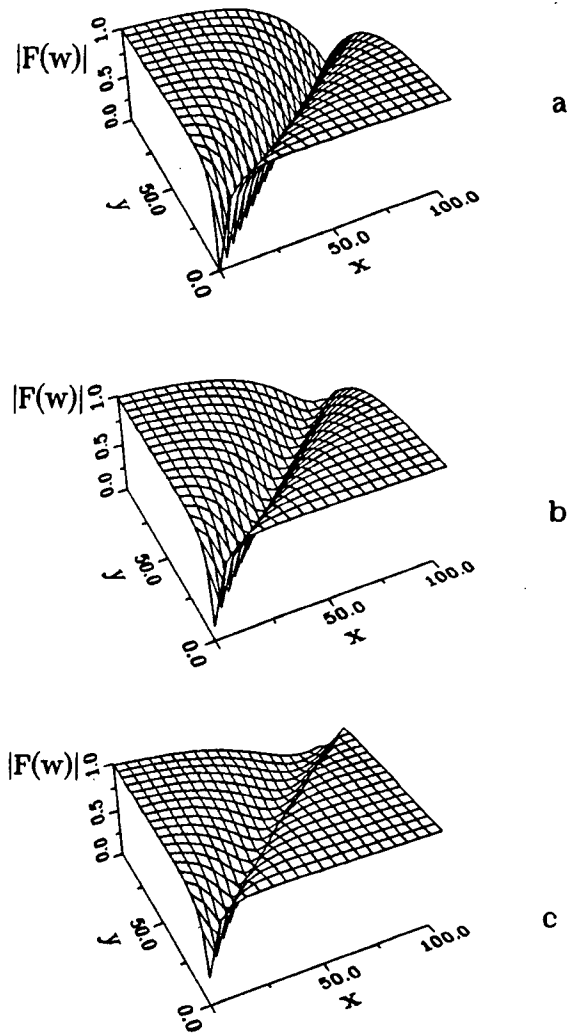
Figure 3.22: The transition function with the source located at $\rho'_r = 50\lambda$, $\phi'_r = 135°$ and $\beta = -90°$. a: kb=0; b: kb=4; c: kb=8.
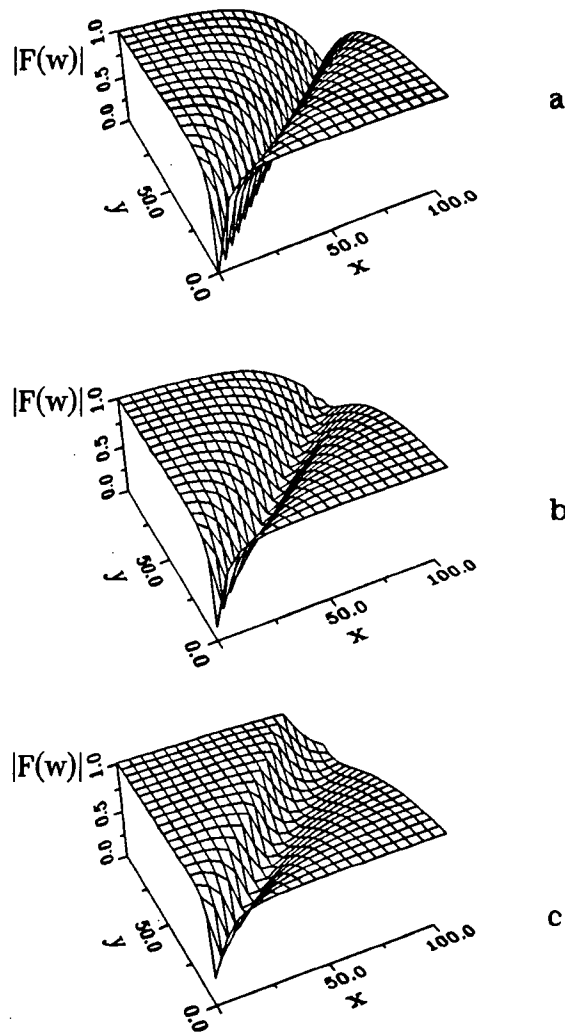
Figure 3.23: The transition function with the source located at $\rho'_r = 50\lambda$, $\phi'_r = 135°$ and $\beta = 0°$. a: kb=0; b: kb=4; c: kb=8.

($\beta = 0°$). Here, when kb is large, the valley in the transition function, figure 3.23c, shifts in the opposite direction to that of figure 3.22c.

Figure 3.24 and 3.25 shows the effect of the change of a beam direction on the transition function $F(w)$. Here, $kb = 8$, β changes from $30°$ to $-120°$. When the beam axis is close to the edge, as in figures 3.24c and 3.25a the transition function still has a deep valley near the reflection boundary. In this circumstance, the GTD diffraction coefficients will be inaccurate. When the beam is directed away from the edge, the deep valley in $|F(w)|$ will disappear. Only in those regions where the transition function is close to unity, UTD and GTD give a similar result.

In general, when kb is large and the beam axis does not pass through the edge, the diffraction is very weak, because only a very small amount of energy strikes the edge and is being diffracted. In this situation, GTD can be used to save the computing time without the loss of accuracy. Otherwise, UTD should be used to ensure the accuracy of the result. This conclusion agrees with Suedan and Jull [34], where they studied a half-plane and a wedge diffraction with a line source incidence.

3.5 Frequency-Domain Solution

In this section, the complex source point method is used to solve beam pulse diffraction by a hard step discontinuity. The geometrical optics field can still be obtained from images and the direct incident field, but reflection and diffraction boundaries are different from the real source case as discussed above. Thus the incident field and reflected fields from the upper boundary, lower boundary and the corner are given by equations 2.12 to 2.15, with appropriate substitutions of the angles and distances discussed in last section. The same is true for the diffractions, where equations 2.23, 2.24, 2.27 and 2.30 can still be used with appropriate substitutions.
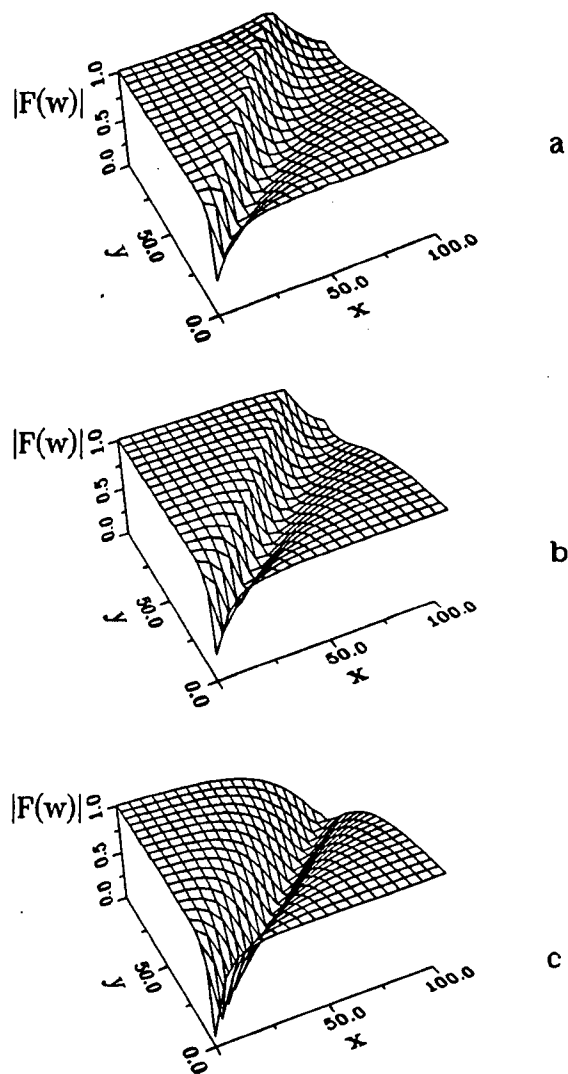
Figure 3.24: The transition function with $\rho'_r = 50\lambda$, $\phi'_r = 135°$ and $kb = 8$. a: $\beta = 30°$; b: $\beta = 0°$; c: $\beta = -30°$.
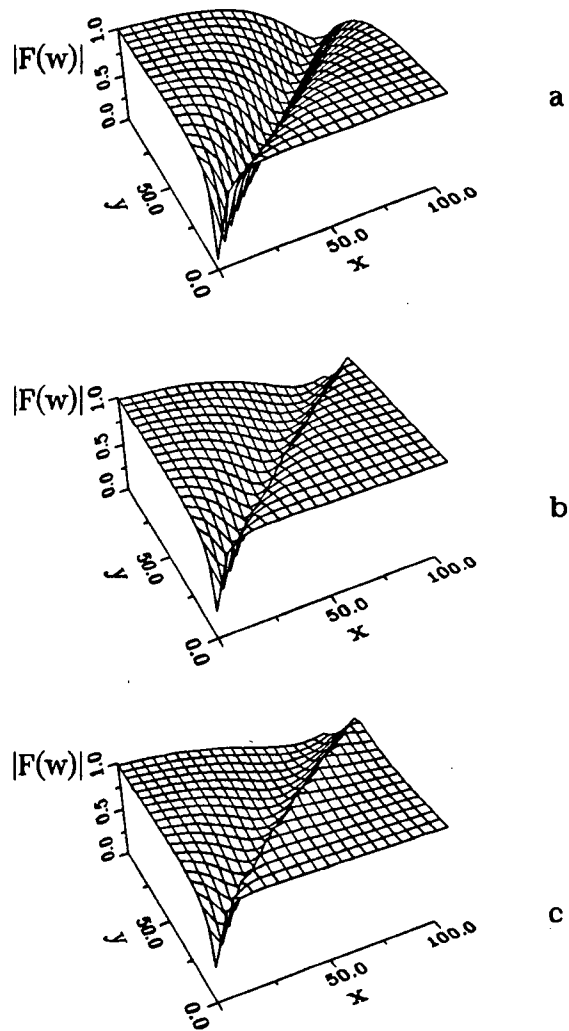
Figure 3.25: The transition function with $\rho'_r = 50\lambda$, $\phi'_r = 135°$ and $kb = 8$. a: $\beta = -60°$; b: $\beta = -90°$; c: $\beta = -120°$.
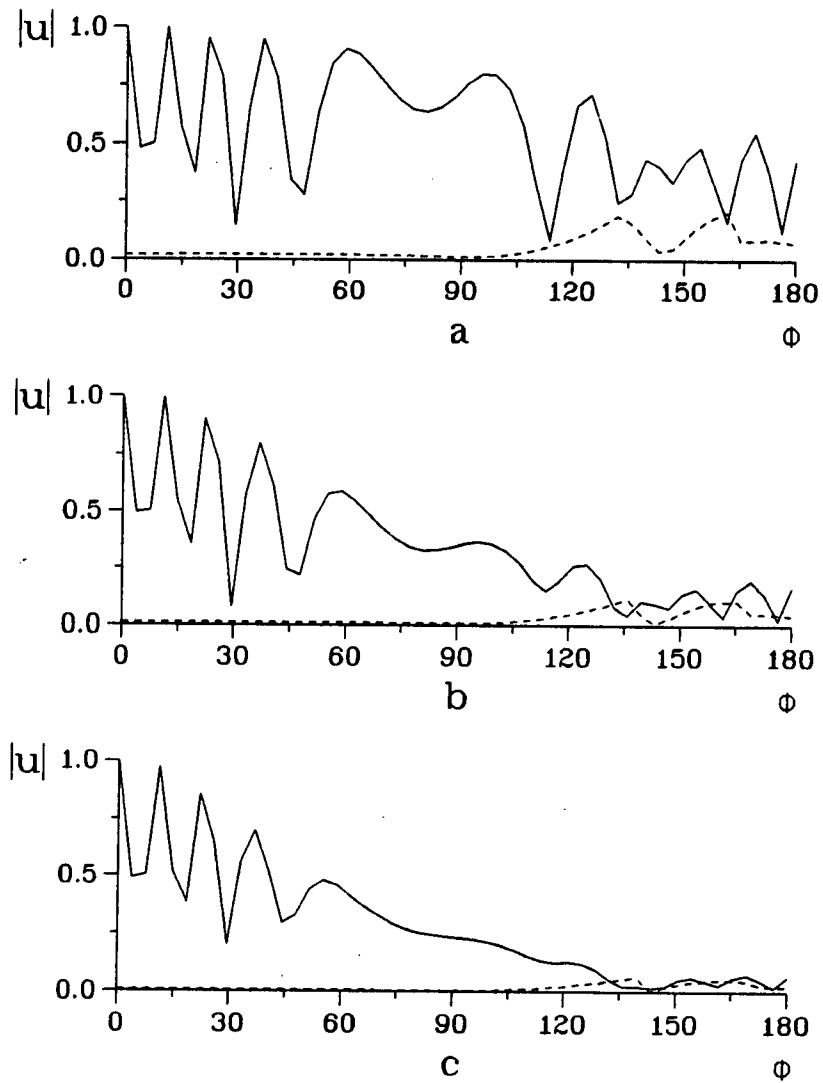
Figure 3.26: Diffraction patterns of a $90°$ step discontinuity with a point source at a complex location. $h = \lambda$, $\rho = 3\lambda$, $\rho'_r = 10\lambda$, $\phi'_r = 45°$ and $\beta = 270°$. a: $kb = 0$, b: $kb = 4$, c: $kb = 8$.
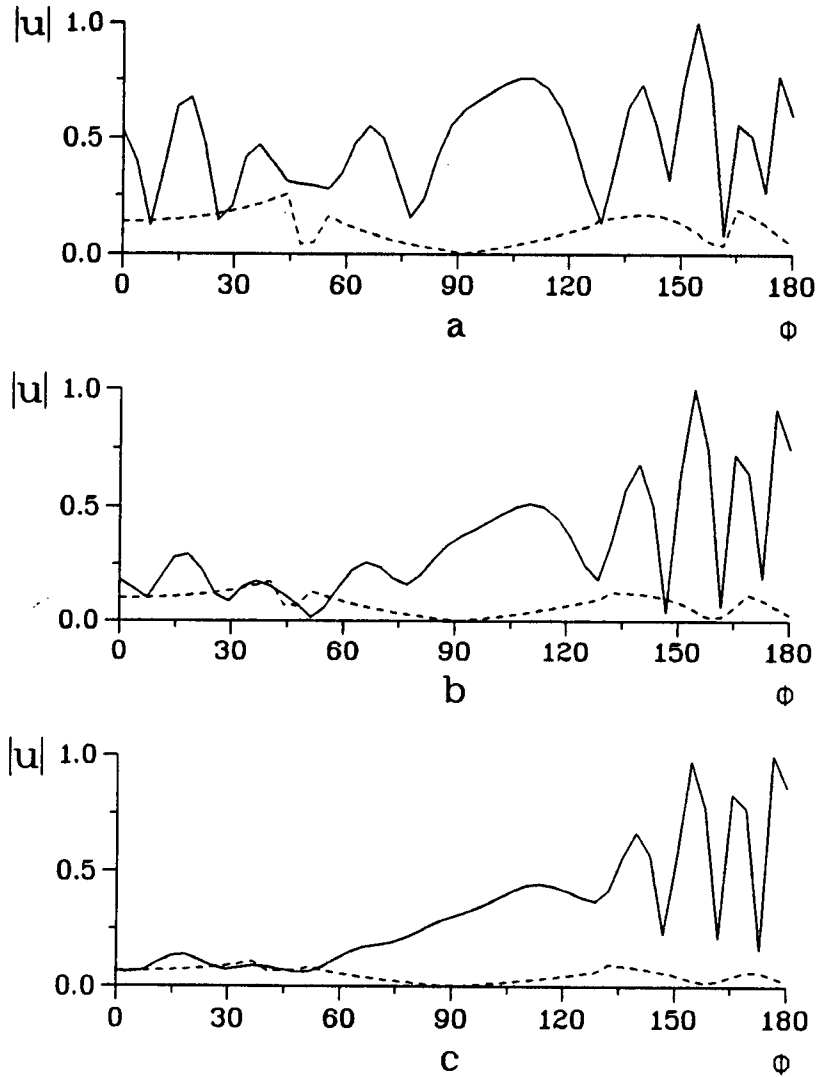
Figure 3.27: Diffraction patterns of a 90° step discontinuity with a point source at a complex location. $h = \lambda$, $\rho = 3\lambda$, $\rho'_r = 10\lambda$, $\phi'_r = 135^{\circ}$ and $\beta = 270^{\circ}$. a: $kb = 0$, b: $kb = 4$, c: $kb = 8$.

The numerical diffraction results are presented in figure 3.26 and 3.27, where diffraction patterns are calculated for $kb = 0$, 4, 8, with h=λ, $\rho'_r = 10\lambda$, $\rho = 3\lambda$ and $\beta = 270°$ for $\phi'_r = 45°$ and $\phi'_r = 135°$. In this case, the direction of the main beam is pointed away from the edge. The field striking the edge become weaker, as kb becomes larger. Therefore, the diffraction as well as the total field away from the main beam becomes weaker as kb changes from 0 to 8.

In figure 3.28, the directivity of the beam is fixed at $kb = 8$ and the beam incident angle is changed from $\beta = -90°$ to $\beta = -135°$. When the beam is aimed at the edge ($\beta = -135°$), the diffraction from the edge is very strong. When the beam is aimed away from the edge, the diffraction is obviously very weak.

3.6   Time-Domain Diffraction

The signal used in this section is the same as equation 2.36, but with different directivities. The source directivity is changed from $kb = 0$ to $kb = 8$, and the beam is directed down to the boundary plane. Thus, when the source-receiver pair is distant from the edge, the diffraction is weak. This effect shows on the diffraction hyperbolic events in figure 3.29. These reflection and diffraction events have been analyzed before. Here, with a beam source incident, the major difference is the magnitude of the corner reflection and edge diffraction, which diminish more rapidly as the source-receiver pair moves away from the top of the edge. The non-zero offset results are presented in figure 3.30 and figure 3.31. These results show similar effects of the beam source on corner reflection and edge diffractions.
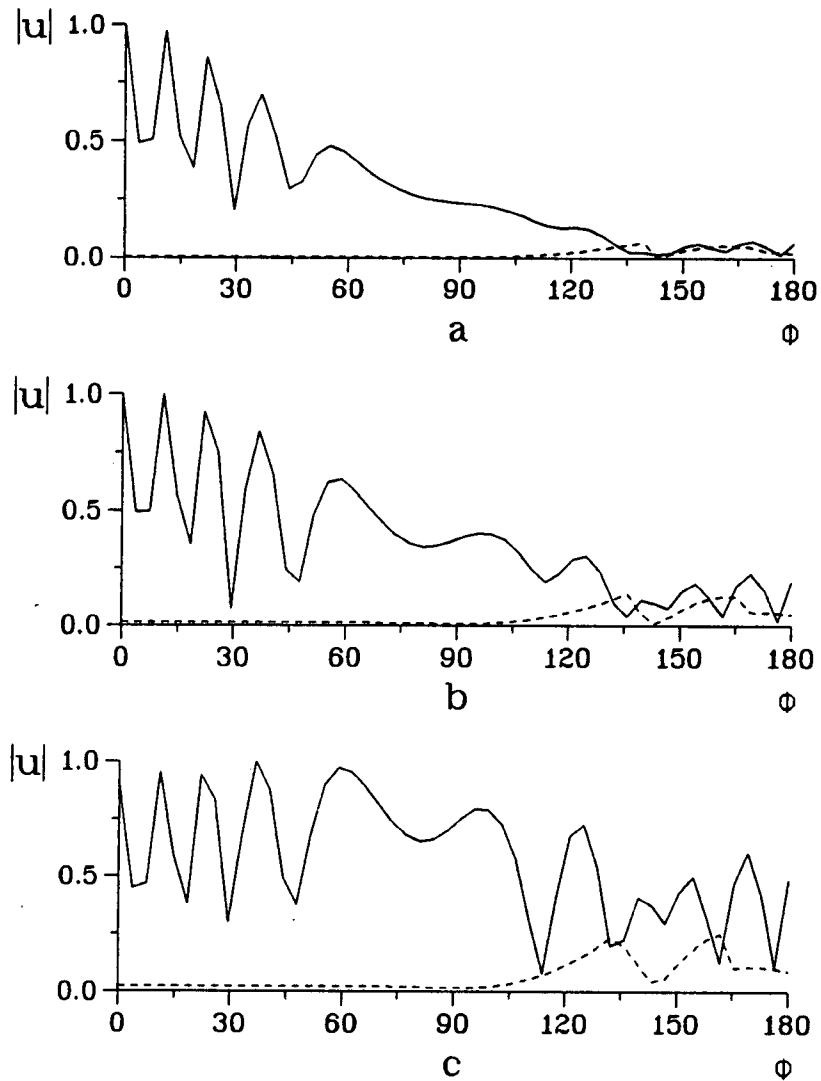
Figure 3.28: Diffraction patterns by a 90° step discontinuity of a point source at a complex location with h=λ, $\rho = 3\lambda$, $\rho'_r = 10\lambda$, $\phi'_r = 45°$ and $kb = 8$. a: $\beta = -90°$, b: $\beta = -115°$, c: $\beta = -135°$.
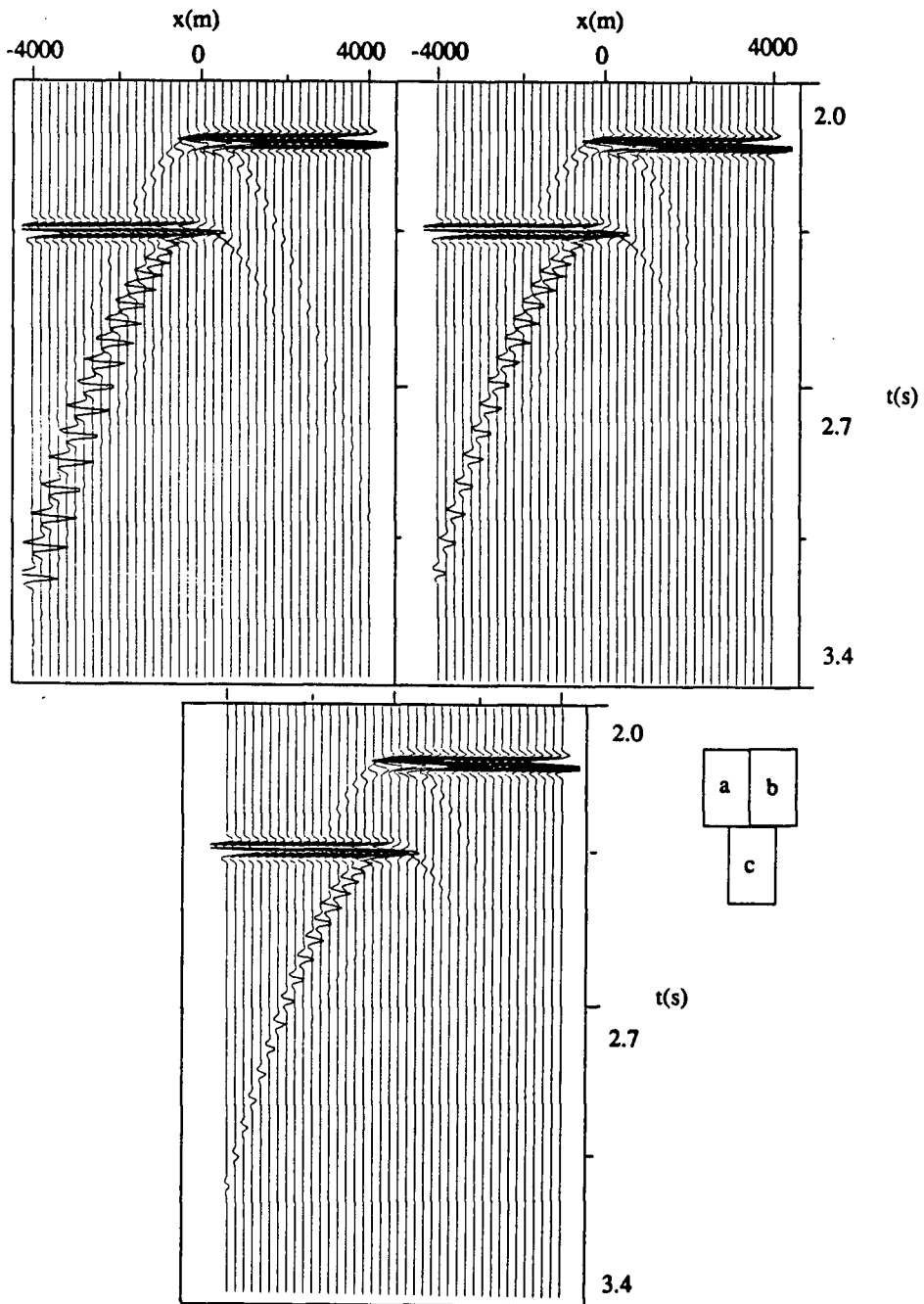
Figure 3.29: Pulse diffraction by a step discontinuity with a beam source. The source and receiver array is positioned at $y_0 = 4000$m with a step height $h = 400m$. The beam is pointed at $\beta = 270°$. a: $kb = 0$, b: $kb = 4$, c: $kb = 8$. Pulse velocity is 4000m/s.
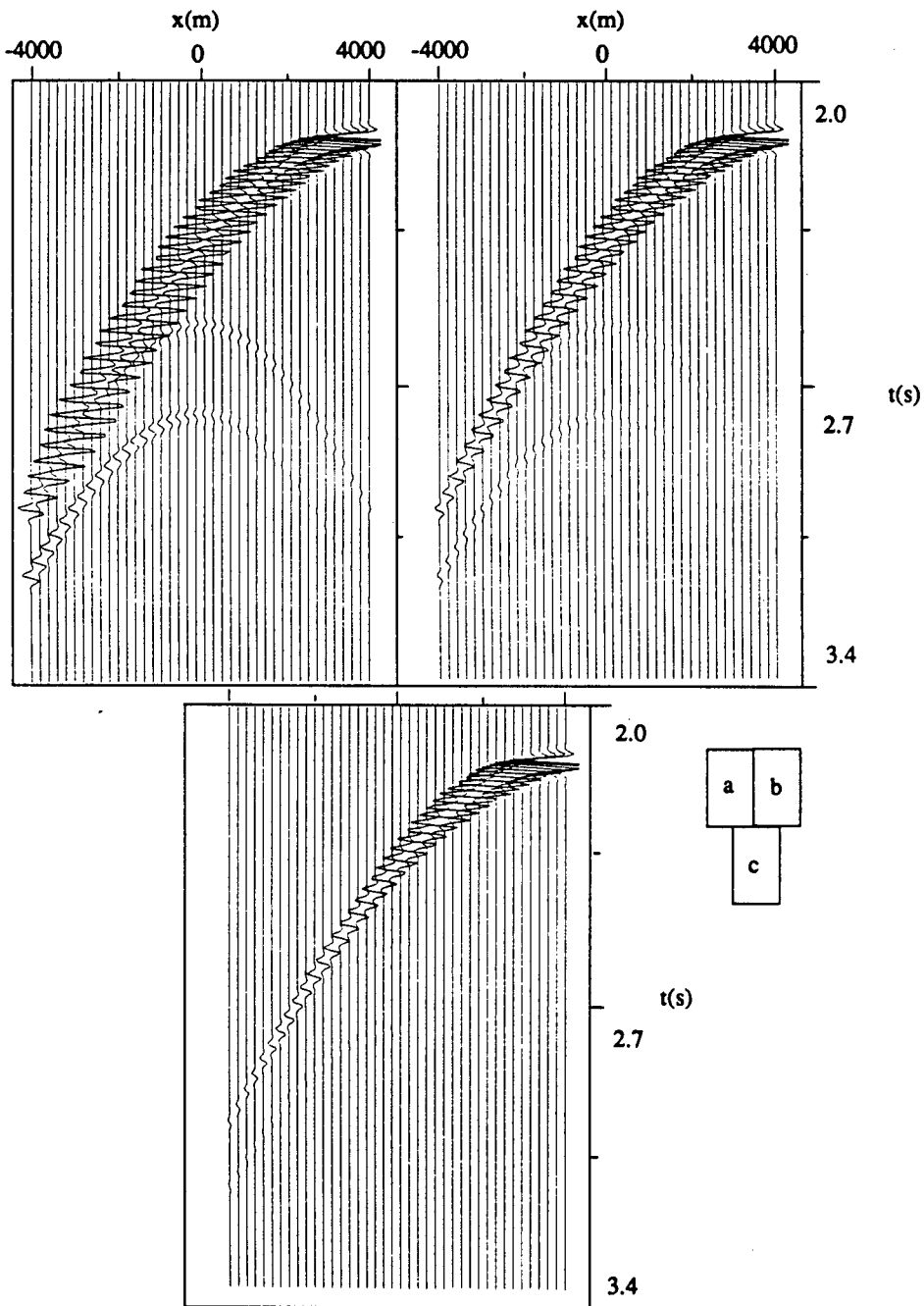
Figure 3.30: Pulse diffraction by a step discontinuity with a beam source. The receiver array is positioned at $y_0 = 4000$m with a step height h=400m. The beam is pointed at $\beta = 270°$ with $\phi'_r = 45°$. a: $kb = 0$, b: $kb = 4$, c: $kb = 8$. Pulse velocity is 4000m/s.
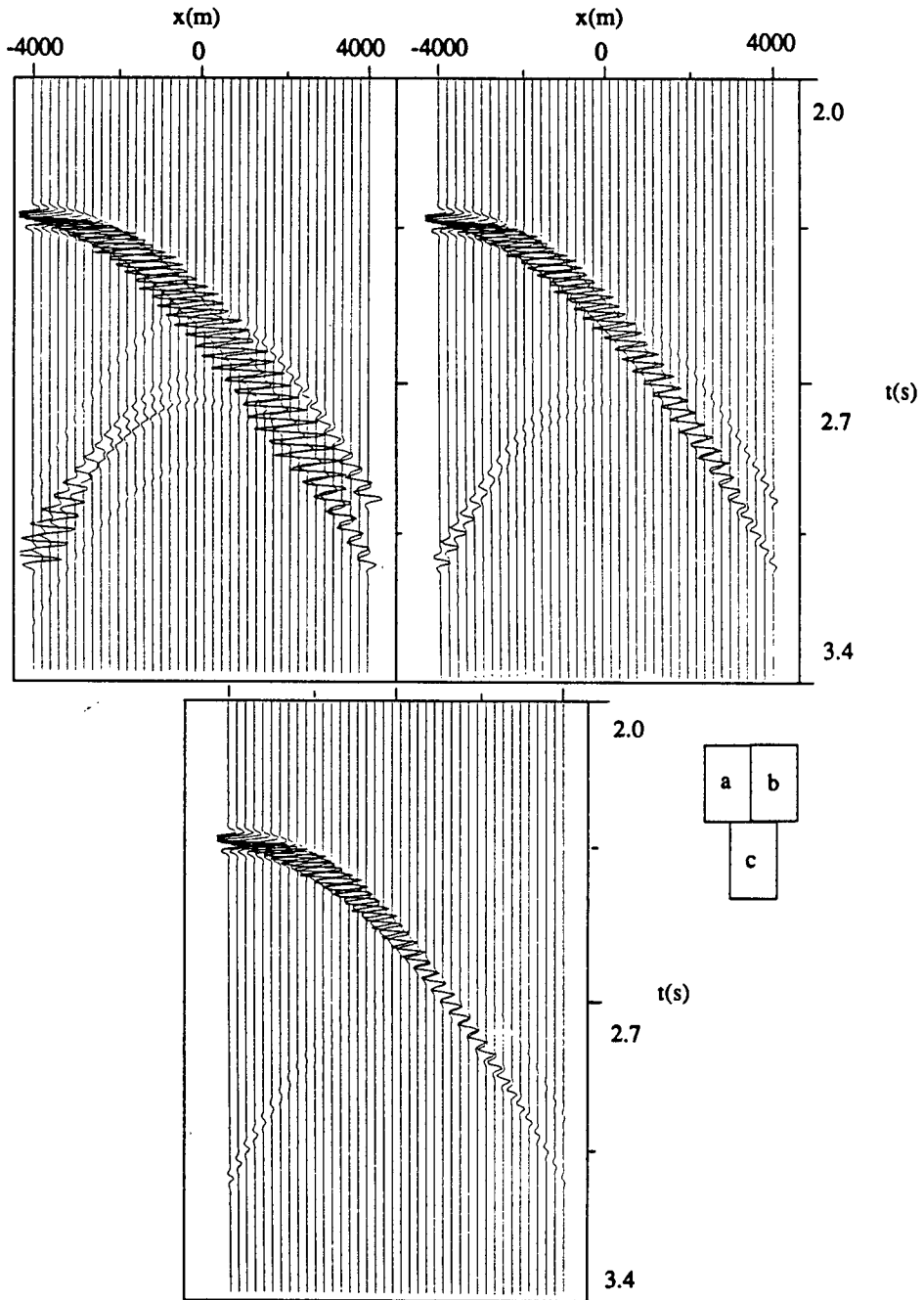
Figure 3.31: Pulse diffraction by a step discontinuity with a beam source. The receiver array is positioned at $y_0 = 4000$m with a step height $h = 400m$. The beam is pointed at $\beta = 270°$ with $\phi'_r = 135°$. a: $kb = 0$, b: $kb = 4$, c: $kb = 8$. Pulse velocity is $4000m/s$.

3.7 Conclusion

Beam diffractions by a step discontinuity are obtained by the method of complex source point in this chapter. The difference between GTD and UTD formulas are examined through the study of the behaviour of the transition function $F(w)$. It is noted that the transition function $F(w)$ is necessary even for highly directive beam.

Chapter 4

TIME-DOMAIN IIR FILTER METHOD

4.1 Introduction

Calculation efficiency is one of the important features of this thesis. In previous chapters, the ray method was used to seek high frequency solutions of the field scattering problem. This asymptotic approach makes it possible to investigate the scattering properties of a complex shape, but for a pulse of certain wavelet, the time consuming fast Fourier transformation (FFT) is still needed to generate the diffraction image. To avoid FFT, a direct time-domain approach can be used, and this requires the impulse response of the diffracted field.

Time-domain solutions of diffraction by a half-plane and a wedge were given by Wait [35] and Felsen and Marcuvitz [36] respectively. Time-domain half-plane diffraction was studied by inverse Fourier transformation of the frequency-domain solution by Dalton and Yedlin [38], [37]. A general pulse response can be obtained from the solutions given in [35], [36], [38], but convolution must be used and it is more time consuming than the FFT procedure. Dalton and Yedlin [37] used an infinite impulse response (IIR) filter to calculate the pulse diffraction by a half-plane, a procedure which eliminates the convolution and accelerates the numerical calculation.

IIR filters, also known as recursive filters, have been recognized as a very efficient and powerful implementation of convolution and many signal processing procedures [39]. Instead of the conventional convolution, an IIR filter can be designed to carry out the

task of transforming the impulse response to a general wavelet response in a recursive way. IIR filtering can be considerably faster than the conventional convolution and very accurate with a properly designed filter. Shanks [39] has shown in one example that the recursion filter is about 45 times faster than simple convolution. He pointed out that it is not unusual to find recursion filter savings of four or five times over conventional convolution in terms of computer CPU time.

The time-domain diffraction results in [35], [36] and [38] are for a half-plane or a wedge only and limited to single diffractions. Here general uniform diffraction coefficients in the time-domain for single and double diffractions are presented. First, the inverse Fourier transformation of the uniform diffraction coefficient is performed. Then, a procedure used by Dalton and Yedlin [37] is adapted with improved efficiency. The convolution of the impulse response with an arbitrary wavelet is digitized. A recursive filter is designed to match the impulse response. The wavelet response is calculated recursively. In this way a substantial amount of computer processing time is saved.

4.2 Inverse Fourier Transformation of the Diffraction Coefficient

The time-domain diffraction coefficient is given by inverse Fourier transforming the frequency-domain coefficient. There are four similar terms in the UTD diffraction coefficient for a wedge. The inverse Fourier transformation will be performed on one term. The rest of the terms can be easily obtained by proper substitution of the corresponding variables and signs.

The UTD diffraction coefficient for a wedge with hard boundary condition can be written as

$$D(\omega) = \sum_{i=1}^{4} 2D_0^i \exp\left[j(\omega T^i + \pi/4)\right] \int_{\sqrt{|\omega T^i|}}^{\infty} \exp\left(-j\tau^2\right)d\tau, \qquad (4.53)$$

where

$$T^{1,2} = \frac{L}{c} a^{\pm}(\phi - \phi'),$$ (4.54)

$$T^{3,4} = \frac{L}{c} a^{\pm}(\phi + \phi'),$$ (4.55)

and

$$D_0^{1,2} = \frac{-1}{2n\sqrt{2\pi/c}} \cot[\frac{\pi \pm (\phi - \phi')}{2n}],$$ (4.56)

$$D_0^{3,4} = \frac{-1}{2n\sqrt{2\pi/c}} \cot[\frac{\pi \pm (\phi + \phi')}{2n}],$$ (4.57)

in which $a^{\pm}(\beta)$ and L are given by equations 1.7 and 1.10. Taking an inverse Fourier transformation of the first term,

$$\tilde{D}^1(t) = \frac{1}{\pi} \text{Re} \int_0^\infty D^1(\omega) \exp(j\omega t) d\omega,$$ (4.58)

where $D^1(\omega)$ is the first term in the uniform diffraction coefficient $D(\omega)$. This can be written as

$$\tilde{D}^1(t) = 2D_0^1 \frac{\sqrt{T^1}}{\pi} Re \int_0^\infty \int_{\sqrt{\omega T^1}}^\infty \exp[j(\omega T^1 + \omega t - \tau^2 + \frac{\pi}{4})] d\tau d\omega.$$ (4.59)

Interchanging the order of integration, $\tilde{D}^1(t)$ can be expressed as

$$\tilde{D}^1(t) = 2D_0 \frac{\sqrt{T^1}}{\pi} Re \int_0^\infty \int_0^{\frac{\tau^2}{T^1}} \exp\left\{ j[\omega(T^1 + t) - \tau^2 + \frac{\pi}{4}] \right\} d\omega d\tau.$$ (4.60)

Using the well known result

$$\int_0^\infty \sin \tau^2 d\tau = \int_0^\infty \cos \tau^2 d\tau = \frac{1}{2}\sqrt{\frac{\pi}{2}},$$ (4.61)

An explicit expression can be obtained,

$$\tilde{D}^1(t) = \frac{D_0^1}{\sqrt{\pi}} \frac{T^1}{(T^1 + t)\sqrt{t}} U(t).$$ (4.62)
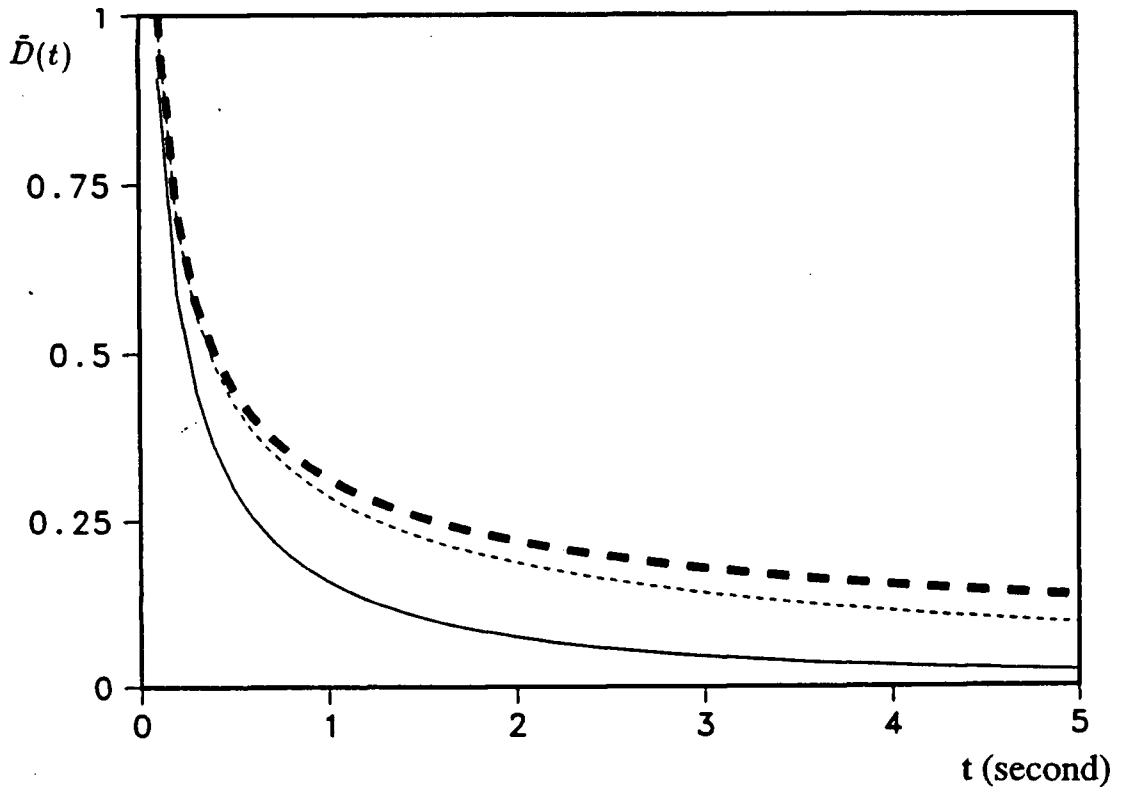
Figure 4.32: The impulse response (4.62) of part of a wedge diffraction coefficient (4.63) normalized to 1 at t=0.1 second. The solid curve represents T^1=1 second; the thin dashed curve represents T^1=10 seconds; the thick dashed curve represents T^1=100 seconds, with $\phi = \phi' = 45^\circ$.

The rest of $\tilde{D}^i(t)$ can be obtained by the proper superscript substitution. The total time-domain UTD diffraction coefficient is given by the inverse Fourier transforming the sum of the four terms in the UTD diffraction coefficient,

$$\tilde{D}(t) = \sum_{i=1}^{4} \tilde{D}^i(t). \tag{4.63}$$

For $T^1 = 1$, 10 and 100 seconds, the impulse response is plotted in figure 4.32, where the maximum has been normalized to 1 at $t = 0.1$ second. When T^1 is large, the impulse response behaves like $1/\sqrt{t}$. While when T^1 is small, the impulse response becomes sharp. Also most of the energy concentrates in the early response for small T^1. It can be shown that for $T^1 \rightarrow 0$, the $\tilde{D}^1(t)$ will approach $\delta(t)$, where $\delta(t)$ is the Dirac delta function. Generally speaking, in the physical world, when $T^i \rightarrow 0$, the receiving point is on the shadow or reflection boundary, where the diffracted field is half of the incident or reflected field. Thus, the diffracted wavelet has the same shape as the incident or reflected wavelet with half its amplitude. The receiver will be well away from the shadow or reflection boundary, when T^i is large. For an early time response, $\tilde{D}^i(t)$ can be simplified to

$$\tilde{D}^i(t) \approx \frac{D_0^i}{\sqrt{\pi t}} U(t). \tag{4.64}$$

The above result is identical to the inverse Fourier transformation of Keller's diffraction coefficient [11].

For double diffraction, if the two edges do not lie in each other's transition region, in the frequency-domain the double diffraction coefficient is just the product of the two single diffraction coefficients. In the time-domain, double diffraction is the autocorrelation of equation 4.62 with different parameters.

Let $D_1(\omega)$, $D_2(\omega)$ denote the first and the second diffraction coefficients respectively. The double diffraction coefficient $D^d(\omega)$ can be written as

$$D^d(\omega) = D_1(\omega)D_2(\omega)$$

$$= \sum_{k=1}^{4}\sum_{i=1}^{4}\{2D_{01}^{k}\exp\left[j(\omega T_1^k + \pi/4)\right]\int_{\sqrt{|\omega T_1^k|}}^{\infty}\exp\left(-j\tau^2\right)d\tau\}$$

$$\{2D_{02}^{i}\exp\left[j(\omega T_2^i + \pi/4)\right]\int_{\sqrt{|\omega T_2^i|}}^{\infty}\exp\left(-j\tau^2\right)d\tau\}, \qquad (4.65)$$

where D_{01}^i, D_{02}^i, T_1^i and T_2^i have the same definition as equation 4.54 and equation 4.56 with the subscript 1 and 2 refer to the first and second edges respectively. Inverse Fourier transforming the above diffraction coefficient gives the time-domain double diffraction coefficient for two wedges as

$$\tilde{D}_d(t) = \sum_{k=1}^{4}\sum_{i=1}^{4}D_{01}^{k}D_{02}^{i}\frac{T_1^k T_2^i}{T_1^k + T_2^i + t}\left[\frac{1}{\sqrt{(t+T_1^k)T_1^k}} + \frac{1}{\sqrt{(t+T_2^i)T_2^i}}\right]U(t), \qquad (4.66)$$

There are no singular points at the origin in double diffraction. This means that the doubly diffracted pulse, generally speaking, is smoother than the singly diffracted pulse and even smoother than the input signal. There are two cases where equation 4.66 can be simplified for its early time response. For example, taking the first term, when T_1^1 and T_2^1 both are much larger than t, then

$$\tilde{D}^{d1}(t) \approx D_{01}^{1}D_{02}^{2}U(t). \qquad (4.67)$$

When only one of the T_{01}^1, T_{02}^1 is large, say T_1^1 is much larger than $T_2^1 + t$,

$$\tilde{D}^{d1}(t) \approx D_{01}^{1}D_{02}^{1}\frac{\sqrt{T_2^1}}{\sqrt{t+T_2^1}}U(t). \qquad (4.68)$$

These two approximations give us a clear picture of the early response of the double diffractions. Because D_{01}^1 and D_{02}^1 are not functions of t, initially, the double diffraction impulse response is simply a step function.

The time-domain result of the single diffraction is the convolution of the incident wavelet with the weighting function $1/\sqrt{t}$ or $T^i/[(T^i + t)\sqrt{t}]$ exactly. In this way the output of a diffraction pulse is different in shape from the input signal. The low frequency

content of the wavelet is emphasized and the high frequency portion is depressed. As a result, the diffraction pulse is flattened. This effect can be easily understood from the fact that single diffraction acts like a low pass filter with a characteristic $1/\sqrt{\omega}$ behaviour. For double diffraction, the diffraction output is just the integral of the input wavelet. This means that the high frequency component in the wavelet is further depressed.

In geophysical applications, diffraction has been treated, most of the time, as noise and been filtered out as much as possible. It is necessary to design a bandpass filter in this case to suppress the diffraction. With the knowledge of this chapter, the diffracted seismic pulse shape can be predicted. Thus a more effective depressing or shaping filter can be designed.

4.3 Digitization of the Convolution

The time-domain diffraction coefficient has been given explicitly in the last section. For an arbitrary wavelet $f(t)$, the single diffraction can be obtained by convoluting the wavelet with equation 4.62 and proper phase and amplitude parameters. In this section, the convolution will be first put into a form which eliminates the singular point in the integrand. Then, this convolution will by digitized.

For simplicity, only one of the four terms in single diffraction by a wedge are considered and the superscript and subscript are neglected to avoid any confusion. It is assumed that the wavelet satisfies two conditions: $f(0) = 0$ and $f(t)$ has weak low frequency content. From chapter 2 and the previous sections, the impulse response for single diffraction for spherical wave incidence can be written as

$$\tilde{u}_\delta(t) = A\frac{D_0}{\sqrt{\pi}}\frac{T}{(T + t - t_0)\sqrt{t - t_0}}U(t - t_0), \qquad (4.69)$$

where

$$A = \frac{1}{\sqrt{\rho \rho'(\rho + \rho')}} \qquad (4.70)$$

and

$$t_0 = \frac{\rho + \rho'}{c}. \qquad (4.71)$$

Thus, the output of a general wavelet $f(t)$ is

$$
\begin{aligned}
\tilde{u}_d(t) &= \tilde{u}_\delta(t) * f(t) \\
&= A \frac{D_0 T}{\sqrt{\pi}} \int_{-\infty}^{\infty} f(\tau) U(\tau) \frac{U(t - \tau - t_0)}{(T + t - \tau - t_0)\sqrt{t - \tau - t_0}} d\tau \\
&= A \frac{D_0 T}{\sqrt{\pi}} \int_{0}^{t - t_0} f(\tau) \frac{d\tau}{(T + t - \tau - t_0)\sqrt{t - \tau - t_0}}.
\end{aligned}
\qquad (4.72)
$$

The integrand is singular at the end point. It is difficult to directly carry out the digitization. To avoid the singular point, integrating by parts with the condition $f(0) = 0$ gives

$$\tilde{u}_d(t) = 2AD_0 \sqrt{\frac{T}{\pi}} \int_{t_0}^{t} f'(t - \tau) \tan^{-1} \sqrt{\frac{\tau - t_0}{T}} d\tau. \qquad (4.73)$$

If $f'(t)$ has no singular point, equation 4.73 can be easily calculated numerically. Let

$$
\begin{aligned}
t_i &= t_0 + i\Delta t, \quad i = 0, \ 1, \ 2, \ \cdots \ (I - 1) \\
\tau_j &= t_0 + j\Delta t, \quad j = 0, \ 1, \ 2, \ \cdots \ (J - 1).
\end{aligned}
\qquad (4.74)
$$

Using summation instead of the integration gives

$$g_i = \bar{D}_0 \sum_{j=0}^{i} f'_{i-j} h_j, \qquad (4.75)$$

where

$$\bar{D}_0 = \frac{2D_0 \sqrt{T} \Delta t}{\sqrt{\pi} \sqrt{\rho \rho'(\rho + \rho')}}, \qquad (4.76)$$

$$g_i = \tilde{u}_d(t_0 + i\Delta t), \qquad (4.77)$$

$$f'_i = f'(i\Delta t) \qquad (4.78)$$

and

$$h_j = \tan^{-1} \sqrt{\frac{j \Delta t}{T}}. \tag{4.79}$$

Equation 4.75 is a standard numerical convolution. The direct calculation is more time consuming than the FFT procedure used in the previous chapters. In the next section, an IIR filter approximation will be used to implement the digital convolution.

4.4 IIR Filter Design and Convolution

In this section, the method discussed by Shanks [39], Burrus and Parks [40] is used to design the IIR filter. This method was also used by Dalton and Yedlin [37] in their study of the half-plane diffraction. In their approach, the matrix β_1 in equation 4.95 is not given explicitly. Here the elements of β_1 is given through a recursion formula which is much more efficient than the matrix inversion.

For two z-transformation functions

$$f(z) = f_0 + f_1 z^{-1} + f_2 z^{-2} + \cdots + f_n z^{-n} \tag{4.80}$$

$$h(z) = h_0 + h_1 z^{-1} + h_2 z^{-2} + \cdots + h_n z^{-n}, \tag{4.81}$$

the product of $f(z)$ and $h(z)$ is given by

$$
\begin{aligned}
g(z) &= f(z) \times h(z) \\
&= (f_0 + f_1 z^{-1} + f_2 z^{-2} + \cdots + f_n z^{-n}) \times \\
&\quad (h_0 + h_1 z^{-1} + h_2 z^{-2} + \cdots + h_m z^{-m}) \\
&= g_0 + g_1 z^{-1} + g_2 z^{-2} + \cdots + g_{m+n} z^{-m-n} \tag{4.82}
\end{aligned}
$$

where

$$g_i = \sum_{j=0}^{i} f_j h_{i-j} \quad i = 0, 1, 2, \cdots, m+n. \tag{4.83}$$

If the system response h_i can be written in a closed form, the convolution can be carried out by recursive calculation and the number of multiplications and summations can be greatly reduced. Assume

$$h_0 + h_1 z^{-1} + h_2 z^{-2} + \cdots + h_{m+n} z^{-m-n} \approx \frac{\sum_{i=0}^{N} a_i z^{-i}}{\sum_{j=0}^{M} b_j z^{-j}} \qquad (4.84)$$

$$= \frac{A(z)}{B(z)}, \qquad (4.85)$$

then

$$(f_0 + f_1 z^{-1} + f_2 z^{-2} + \cdots + f_n z^{-n}) \frac{\sum_{i=0}^{N} a_i z^{-i}}{\sum_{j=0}^{M} b_j z^{-j}} \qquad (4.86)$$

$$\approx g_0 + g_1 z^{-1} + g_2 z^{-2} + \cdots + g_{m+n} z^{-n-m}. \qquad (4.87)$$

By rearranging, this can be written as

$$(f_0 + f_1 z^{-1} + f_2 z^{-2} + \cdots + f_n z^{-n})(\sum_{i=0}^{N} a_i z^{-i}) \qquad (4.88)$$

$$\approx (g_0 + g_1 z^{-1} + g_2 z^{-2} + \cdots + g_{n+m} z^{-n-m})(\sum_{j=0}^{M} b_j z^{-j}) \qquad (4.89)$$

Without loss of generality, assuming $b_0 = 1$, g_i can be obtained by the following recursive formula

$$g_i \approx \sum_{j=0}^{i} f_j a_{i-j} - \sum_{j=0}^{i-1} g_j b_{i-j} \qquad (4.90)$$

If M and N are small integers, which usually is the case, the saving of the computing time is phenomenal. But for the problem of the last section, the impulse response is not in the form of a closed rational function. An approximate rational function has to be designed, which should give the same coefficient when expanded into z^{-i} series. This filter design procedure is rather time consuming. There are several approaches to the IIR filter design. Generally speaking, different approaches give different results. One design procedure may give a better result than the other in one occasion, while another algorithm may be more suitable itself in a different situation. Here, the method, which

was first discussed by Shanks [39] and later by Burrus and Parks [40] is used and an efficient design equation is derived to implement the recursive filter.

The computation method used in IIR filter design is very important. Numerical approximation by the computer results in errors. The accumulation of errors in the numerical result can prevent accurate filter design. By optimizing the design formulas, computer round off errors can be reduced. Here an optimized IIR filter design formula is given.

Applying the Burrus and Parks' notation [40], the coefficients b_1, b_2, $\cdots$, b_M in equation 4.90 can be obtained from the matrix equation

$$H_3^T H_3 B = H_3^T H^1, \tag{4.91}$$

where

$$B = \begin{bmatrix} b_1 \\ b_2 \\ \vdots \\ b_M \end{bmatrix}. \tag{4.92}$$

The elements of matrix H_3 are given by

$$h_{ij}^3 = h_{N-1+i-j} \tag{4.93}$$

and the column matrix H^1 is

$$H^1 = \begin{bmatrix} h_N \\ h_{N+1} \\ \vdots \\ h_{K-1} \end{bmatrix}. \tag{4.94}$$

The coefficients a_i in equation 4.90 can be found from

$$A = \left[\beta_1^T \beta_1 \right]^{-1} \beta_1^T h \tag{4.95}$$

with

$$A = \begin{bmatrix} a_1 \\ a_2 \\ \vdots \\ a_M \end{bmatrix} \tag{4.96}$$

and

$$h = \begin{bmatrix} h_0 \\ h_1 \\ \vdots \\ h_{K-1} \end{bmatrix}, \tag{4.97}$$

where h_j is given by equation 4.79. β_1 is a K by M matrix, the elements of β_1 are given by

$$\beta_{1i,j} = \begin{cases} 0, & i < j \\ 1, & i = j \\ \beta_{i-j}, & i > j \end{cases} \tag{4.98}$$

and β_i is given recursively

$$\begin{aligned} \beta_0 &= 1 \\ \beta_i &= -\sum_{j=0}^{i-1} \beta_j b_{i-j}, \quad i = 1, 2, \cdots, K-1. \end{aligned} \tag{4.99}$$

This method is used to calculate the diffraction coefficients of different incident angles, $\phi = \phi' = 25°$, $45°$ and $88°$. For $\phi = \phi' = 88°$, the wave is almost vertically incident on the reflection surface and the diffraction coefficient approaches a delta function. This case represents the most difficult situation in the design. Different values of $N = M$ are tested ranging from 2 to 15. Here the lowest $N = M$, which can ensure that the absolute error is less than one percent, is chosen. It is found that for $N = M$ less than 10 all the diffraction coefficients can be easily approximated. The results are shown in figure 4.33.
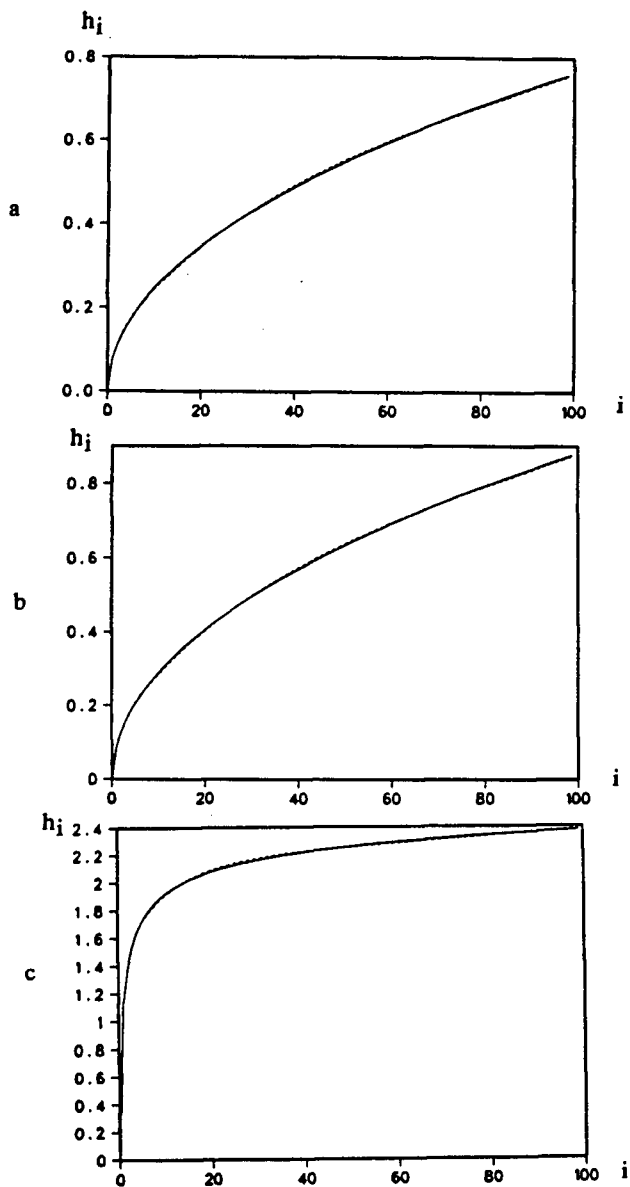
Figure 4.33: Impulse responses of the filters designed by Shanks' method. Solid curve represents the exact impulse response; dashed curve represents ·the approximated filter impulse response. a: $\phi = \phi' = 25°$; b: $\phi = \phi' = 45°$; c: $\phi = \phi' = 88°$.

In the following section this method will be used in the IIR filter design. In the calculation, it is found that most of the computing time is used by the filter design. Calculation shows that it is unnecessary to search for the best values of N and M every time. $N = M$ can be chosen large enough to handle the most difficult case. Thus, in the following calculation $M = N$ is set equal to 9.

Once the IIR filter is obtained in the form of a rational function of z variables, the convolution of the equation 4.75 can be carried out by the following recursive formula

$$g_i = \tilde{D}_0 \sum_{j=0}^{min[i,\ N-1]} a_j f'_{i-j} - \sum_{j=1}^{min[j,\ M-1]} b_j g_{i-j}, \tag{4.100}$$

where $\tilde{D}_0$ and f'_i are given by equations 4.76 and 4.78 respectively.

4.5 Numerical Example for Single Diffraction

Next the single diffraction by a hard step discontinuity is obtained via time-domain convolution and IIR filter method. In order to compare the speed, the same response is calculated in frequency-domain and FFT is used to convert the result back to the time-domain.

A Berlage wavelet [41] is used here with $f(t) = U(t)t^3 \exp(-190t)\sin(60\pi t)$ and velocity $c = 4 \times 10^3 m/s$, step height $h = 4 \times 10^3 m$, source and receiver positions $y_0 = 4 \times 10^3 m$, $K = I = J = 100$. The results are shown in figure 4.34. The two diffraction patterns virtually identical, but the computer CPU time used by the different methods is different. To generate these diffraction images, the CPU time for the IIR filter method is 6 seconds while the CPU time for the FFT method is 24 seconds on an Amdahl 5850 computer. Figure 4.34 includes only single diffractions. If double diffractions are included, sixteen IIR filters have to be designed for every doubly diffracted ray. Thus it is evident that this approach is less efficient for double diffraction.
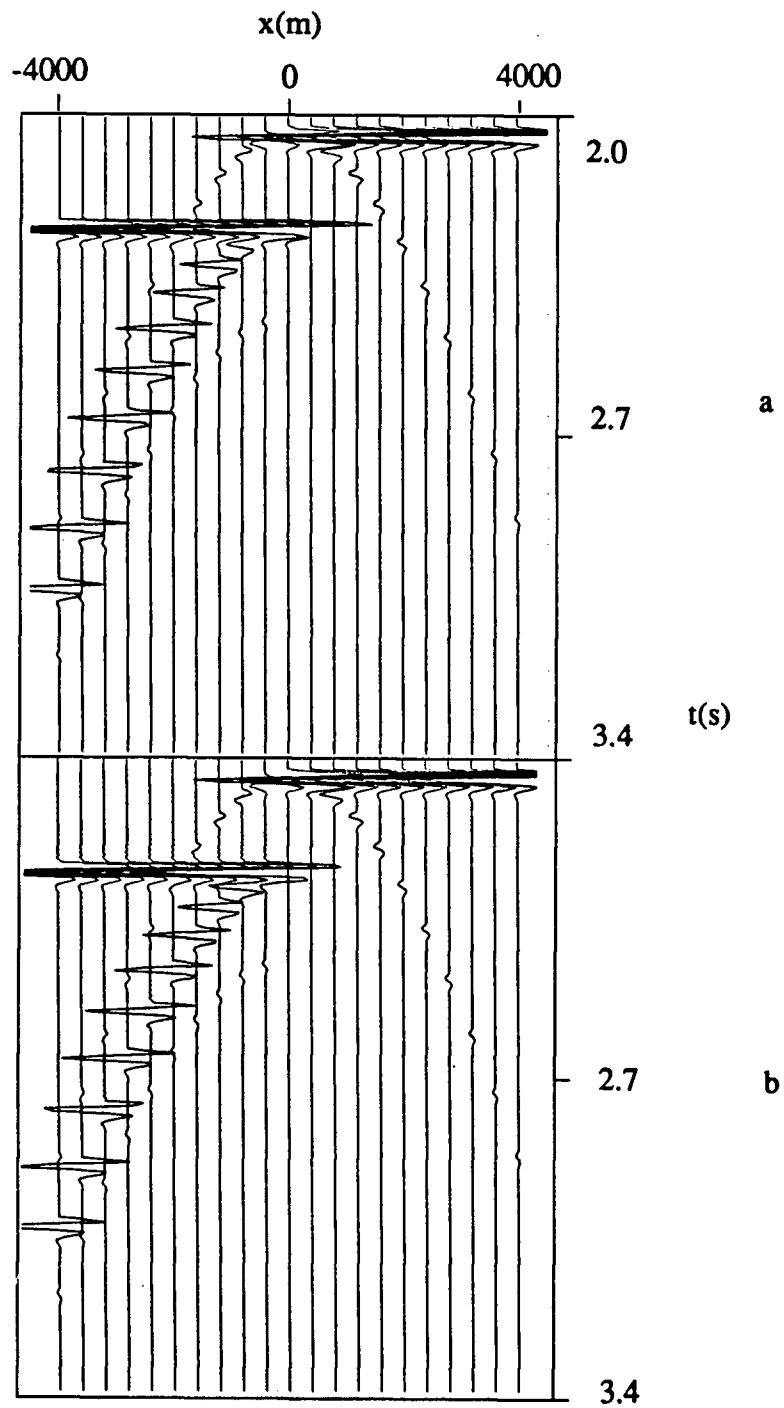
Figure 4.34: Scattering from a step discontinuity. Step height $h = 4 \times 10^3$ meters, source and receiver array is positioned at $y_0 = 4 \times 10^3$ meters. a: result by IIR filter approach; b: result by FFT approach.

4.6 Conclusion

In this chapter, calculation of pulse diffraction by a hard step discontinuity is approached differently. The inverse Fourier transformation results are used to derive time-domain diffraction. An IIR filter is designed to carry out the numerical convolution recursively. Because the order of the filter is very small ($M = N = 9$), the IIR filter method is very efficient. For single diffraction, one scattering image shown in figure 4.34 can save 75 percent of the computer CPU time.

The IIR filter method can also be used in the calculation of the double diffraction. The time-domain double diffraction coefficient is given by equation 4.66. Because of the complex nature of the double diffraction, the implementation of the IIR filter method will be difficult. In the time-domain, convolution has to be performed for each single diffraction and double diffraction but only one FFT is needed by the frequency-domain approach.

Both impulse responses of single diffraction and double diffraction are given explicitly in this chapter. This information can be used in the filter design either to subtract the diffraction signal or to suppress the diffraction.

Chapter 5

DIFFRACTION BY A CURVED HALF PLANE

5.1 Introduction

High frequency solutions of electromagnetic scattering from simple shapes have been extensively studied in the past and widely reported in the open literature, but results for complex structures which can be constructed from the simple shapes are relatively few. Although some experimental results have been reported [3], the theoretical analysis of diffraction is often not satisfactory. The study of the diffraction by complex shapes is important in itself. First, when simple shapes are combined, new diffraction mechanisms are created. Generally, new problems cannot be treated by classical methods and an approximate approach has to be adopted. Also, the solution of complex shapes constitutes a central step in constructing solutions of scattering objects of practical interest in radar and seismic applications.

In this chapter, spherical wave diffraction by a convex side of a cylindrically curved sheet tangential to a half-plane is studied. The geometry of the problem is shown in figure 5.35. A similar configuration has been studied by Chuang [60] for a plane wave at grazing incidence. By the extension of Weston's [30] result, he obtained diffracted fields in both shadow and lit regions. Here an asymptotic solution for general spherical wave incidence from an arbitrary point above the perfectly hard surface is obtained. This solution, which includes the geometric optics field, the edge diffracted creeping wave and space ray, the second order edge diffracted space ray and uses GTD, UTD, physical optics
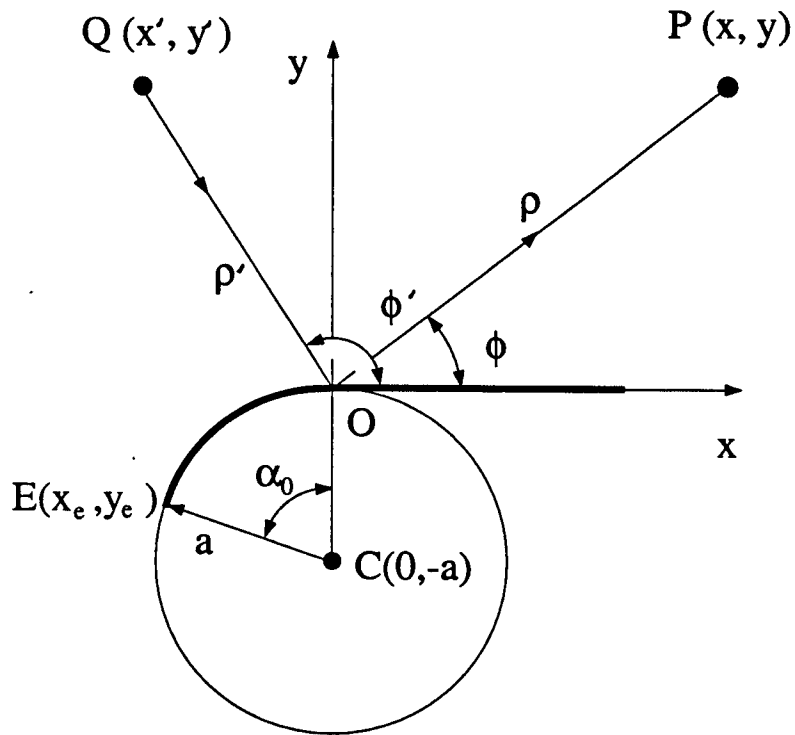
Figure 5.35: Geometry of a curved half-plane.

and the creeping wave diffraction coefficient for an edge on a curved surface by Idemen and Erdogan [23], is presently the most complete high frequency solution to the problem. This result can serve as a building block for the solution of more complicated structures.

Here a hard boundary is assumed; that is, the normal derivative of the total field equals zero on the scattering body. The radius of the curvature of the cylinder must be large in wavelengths with high frequency approximations (ka≫1) and far field conditions (kr≫1) satisfied. It is also assumed that the field point P and the source point Q are always in the upper half of the x-y plane, so that only the convex side of the cylinder is illuminated. It is quite easy to generalize the current result to a soft boundary and oblique incidence.

In figure 5.35, the total field at a receiving point consists of reflection from the boundary surface and diffractions from the two edges. The first order edge at $E(x_e, y_e)$ gives rise to the edge diffracted space ray and an edge diffracted creeping wave. These two rays are of the order $1/\sqrt{k}$, where $k = 2\pi/\lambda$ is the propagation constant, which is assumed to be large. Here, the whispering gallery mode is neglected, because its contribution to the total field at receiving point is of higher order $(1/k)$. The second order edge at $O(0, 0)$ also gives rise to space rays and creeping waves, but the creeping wave which is much weaker than the space ray is neglected.

The edge diffraction at $E(x_e, y_e)$ makes the total field continuous across the reflection boundary generated by the discontinuity of the cylindrical sheet. The diffracted creeping wave extends this diffraction to the shadow region where the diffracted space ray is blocked by the curved surface. The second order edge diffraction compensates for the discontinuity of the geometrical optics field because of the change of the surface curvature. Away from the reflection boundary, the second order edge diffraction is of higher order compared with the first order edge diffraction, and is negligible. But the second order edge diffraction is significant when the field point is near the reflection boundary. There

are also higher order multiple diffractions because of the interaction between the two edges. They are less important than the field discussed above. In the time-domain, these multiple diffractions are later arrivals. The inclusion of these diffractions does not improve the early response which is most important. Thus, these multiple diffractions are neglected.

The method used in this chapter is Keller's geometrical theory of diffraction and the theory of physical optics. The uniform diffraction coefficients given by UTD are used to calculate the space ray diffracted by an edge. These diffraction coefficients are still valid when the edge is formed by a curved surface. This extension is justified by the argument of the local effect of the diffraction phenomenon.

Apart from the space rays, there are creeping waves on the cylinder. This creeping wave has been largely neglected in high frequency antenna analysis, because of the lack of an appropriate diffraction coefficient. Albertsen and Christiansen [22] constructed some creeping wave hybrid diffraction coefficients from a set of elementary diffraction coefficients. Idemen and Erdogan [23] solved the second order canonical problem of GTD–diffraction by a curved sheet. They used generalized cylindrical coordinates to construct a Hilbert problem and found a high frequency asymptotic solution. From this solution, they extracted the various diffraction coefficients (or transformation coefficients) for the creeping wave. With these diffraction coefficients, the creeping wave can be handled in the same way as the space ray. The launching coefficient and the attenuation coefficient associated with the smooth part of the cylinder were given by Levy and Keller [21] in 1959.

There is a transition region of angular width the order of m^{-1} radians $[m = (ka/2)^{1/3}]$ near grazing incidence. In this region, both Kouyoumjian and Pathak's UTD [15] and the diffraction coefficient given by Serbest [24] based on [23] fail. Michaeli [25] [26] [27] derived a solution valid in this transition region. He multiplied the UTD diffraction

coefficient by the Fock function to give a uniform diffraction coefficient. On the dark side of the edge diffraction, the solution was also given in term of the Fock function, which gives the same results of Idemen and Serbest if enough higher order terms in [24] are included.

At the junction of the cylinder and the half-plane, a second order edge (after Kaminetsky and Keller [61]) is created. A second order edge is an edge at which the second derivative of the surface has a discontinuity while the first order derivative is continuous. The diffraction phenomenon by the second order edge on a conducting surface was first studied by Weston [30] and Hong and Weston [42]. By an extension of Weston's method, Senior [31] derived the first diffraction coefficient for the second order edge. Later, Kaminetsky and Keller [61] generalized this diffraction coefficient to include impedance boundary conditions by a different approach. All these results are invalid in the vicinity of the reflection boundary where they are of vital importance.

There are two major methods to obtain a uniform version of the second order edge diffraction coefficient. First, in Keller's approach, a uniform asymptotic expansion formula by Bleistein [62] can be used when the stationary point close to the second order edge. Second, using the theory of physical optics, a uniform diffraction coefficient can be obtained by the uniform asymptotic evaluation of the end point contribution from the surface integral. The second approach, which is simple in conception, has been used by James [32] for the edge formed by smoothly joined cylinders. This diffraction coefficient enables the total field to change continuously in the transition region at the reflection boundary and retains Senior's result away from the reflection boundary. James' method is used here to derive the second order edge diffraction coefficient.

Once the frequency-domain solution is obtained, the time-domain solution is constructed by Fourier transformation. A measured result of acoustic pulse diffraction by the same object is given. A quantitative comparison is not possible at this stage, but a

qualitative comparison shows good agreement between theoretical prediction and experimental observation.

5.2   Geometric Optics Field

There are three species of the geometric optics fields: direct incident field from the source, reflection from the half-plane and reflection from the cylinder, as shown in figure 5.36 and figure 5.37. It is straight forward to find the incident field from the source and reflected field from the half plane. For the reflection from the cylinder, the formulas given by [63] are used and appear below.

For a point source at (x', y'), and the incident field is given by

$$u^i = \frac{\exp(-jkr)}{r}, \qquad (5.101)$$

where

$$r = \sqrt{(x - x')^2 + (y - y')^2} \qquad (5.102)$$

and x, y are the coordinates of the field point. The reflection from the half-plane can be obtained by the source image,

$$u^r = \frac{\exp(-jkr_r)}{r_r} U[\pi - (\phi - \phi')], \qquad (5.103)$$

where

$$r_r = \sqrt{(x - x')^2 + (y + y')^2} \qquad (5.104)$$

and

$$U(x) = \begin{cases} 1, & x > 0 \\ 0, & x < 0 \end{cases}, \qquad (5.105)$$

the angles ϕ and ϕ' are defined in figure 5.36.

For the cylindrical segment, the reflected field in the illuminated region is

$$u^r = \left\{ f^2 (1 + \sqrt{\tfrac{g}{f}})[1 + \tfrac{g}{f} + \tfrac{2g}{a\cos(\psi_1 + \beta)}] \right\}^{-\frac{1}{2}} \qquad (5.106)$$

$$\times \exp[-jk(f + g)]. \qquad (5.107)$$
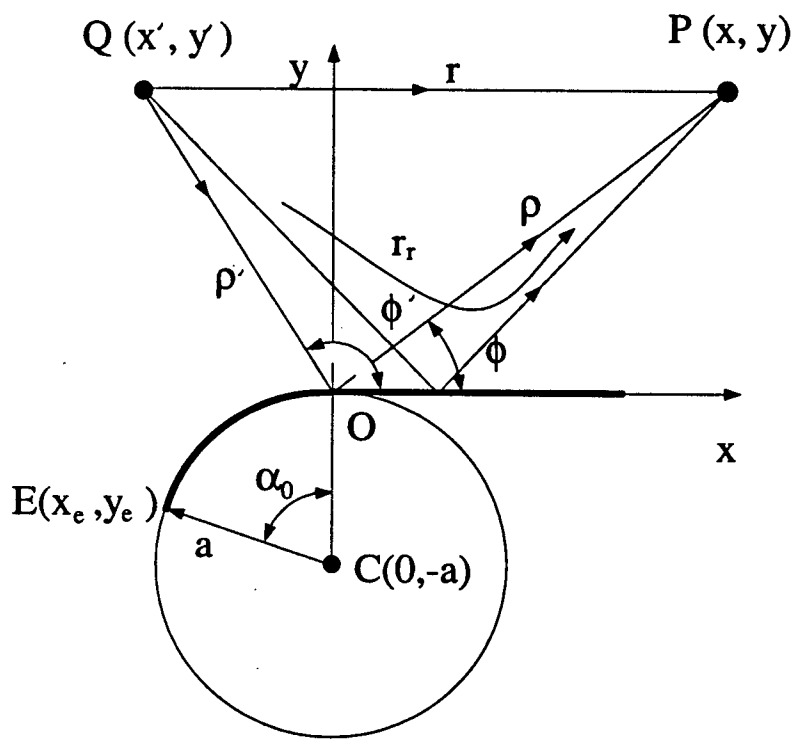
Figure 5.36: Coordinates for reflection from the half-plane.
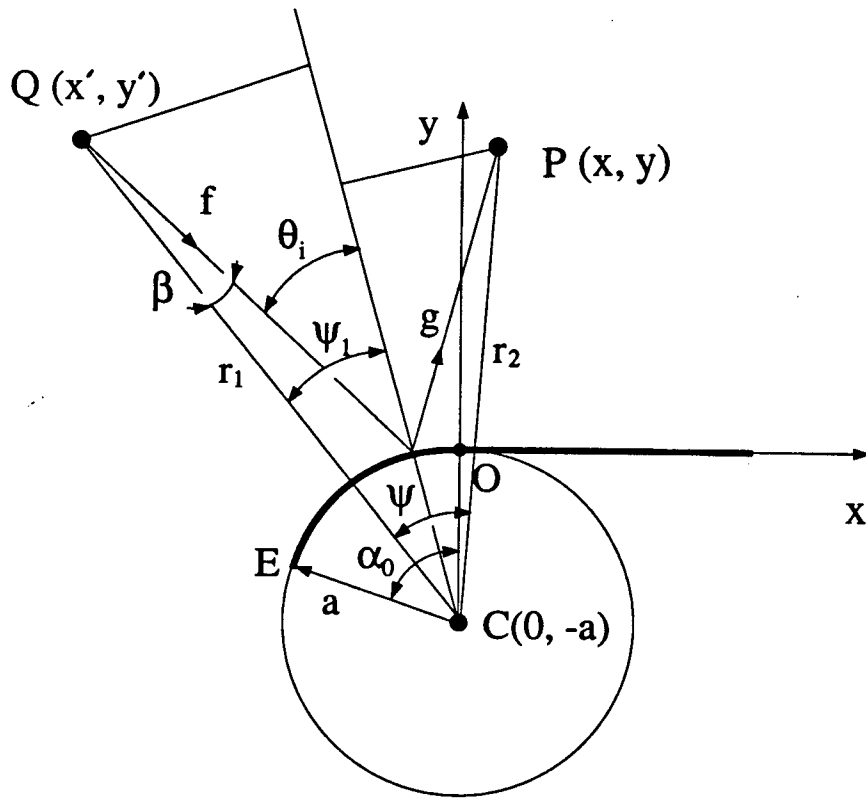
Figure 5.37: Coordinates for reflection from the circular cylinder.

With the aid of figure 5.37, the parameters can be found as:

$$f = \sqrt{r_1{}^2 + a^2 - 2ar_1 \cos \psi_1}, \tag{5.108}$$

$$g = \sqrt{r_2{}^2 + a^2 - 2ar_2 \cos(\psi_1 - \psi)}, \tag{5.109}$$

$$\beta = \arcsin(\frac{a}{f} \sin \psi_1), \tag{5.110}$$

where $\psi_1 < \pi/2$, is the root of

$$\frac{r_1}{f} \sin \psi_1 + \frac{r_2}{g} \sin(\psi_1 - \psi) = 0, \tag{5.111}$$

and

$$\psi = \arctan(\frac{y + a}{x}) - \arctan(\frac{y' + a}{x'}), \tag{5.112}$$

$$r_1 = \sqrt{x'^2 + (y' + a)^2}, \tag{5.113}$$

$$r_2 = \sqrt{x^2 + (y + a)^2}. \tag{5.114}$$

For zero offset, $\rho = \rho'$, $\phi = \phi'$, reflection simplifies to:

$$u^r = \frac{\exp(-2jkr_r)}{2r_r} \sqrt{\frac{a}{a + r_r}} U(x - x_{max})U(-x), \tag{5.115}$$

where

$$x_{max} = -(y + a) \tan \alpha_0 \tag{5.116}$$

and

$$r_r = r_1 - a. \tag{5.117}$$

5.3 Edge Diffracted Space Ray

By the theory of GTD, high frequency diffraction, like high frequency reflection, is a local phenomenon. Locally an edge of a curved surface can thus be replaced by a half-plane tangent to the curved surface at edge. Therefore, the edge diffracted space ray, if away

from the edge and grazing incidence region, is the same as the space ray diffracted by a half plane which is tangent to the edge of the curved sheet. Here, the uniform GTD formula [15] is used to calculate the edge diffracted space ray.

For a source at $Q(x', y')$ and field point at $P(x, y)$, as shown in figure 5.38, the diffracted field is

$$u^d = \frac{\exp(-jkr_i)}{r_i}\sqrt{\frac{r_i}{r_d(r_i + r_d)}}D(\psi, \psi')\exp(-jkr_d), \qquad (5.118)$$

where

$$r_i = \sqrt{(x_e - x')^2 + (y_e - y')^2}, \qquad (5.119)$$

$$r_d = \sqrt{(x_e - x)^2 + (y_e - y)^2}. \qquad (5.120)$$

The coordinates of the edge E are given by

$$x_e = -a\sin\alpha_o, \qquad (5.121)$$

$$y_e = a(\cos\alpha_o - 1). \qquad (5.122)$$

The UTD edge diffraction coefficient for a curved half-plane is

$$D(\psi', \psi) = \frac{-\exp(-j\frac{\pi}{4})}{\sqrt{8k\pi}}\left\{ F[kL^i a(\psi - \psi')]\frac{1}{\cos\frac{\psi-\psi'}{2}} \right. \qquad (5.123)$$

$$\left. +F[kL^r a(\psi + \psi')]\frac{1}{\cos\frac{\psi+\psi'}{2}} \right\}. \qquad (5.124)$$

The distance parameters L^i and L^r are determined from the continuity of the total field at the reflection or shadow boundaries. The general forms are

$$L^i = \frac{r_d(\rho_e^i + r_d)\rho_1^i\rho_2^i}{\rho_e^i(\rho_1^i + r_d)(\rho_2^i + r_d)}, \qquad (5.125)$$

$$L^r = \frac{r_d(\rho_e^r + r_d)\rho_1^r\rho_2^r}{\rho_e^r(\rho_1^r + r_d)(\rho_2^r + r_d)}, \qquad (5.126)$$

wherein ρ_e^i (ρ_e^r) is the radius of the curvature of the incident (reflected) wavefront at E taken in the plane containing the incident (reflected) ray and unit vector tangent to
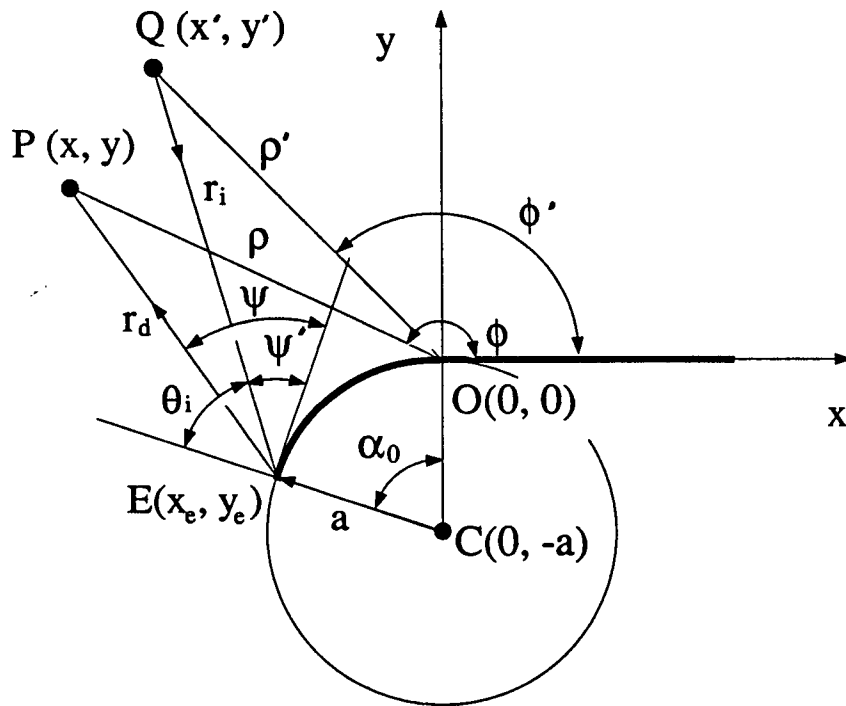
Figure 5.38: Coordinates for diffraction from the first order edge $E(x_e, y_e)$ of a curved half-plane.

the edge at E, $\rho_1^i(\rho_1^r)$, $\rho_2^i(\rho_2^r)$ are the principal radii of the curvatures of the incident (reflected) wavefront at the diffraction point. For a straight edge (as in the present case), the curvature of the edge is infinite, consequently

$$\rho_e^i = \rho_e^r = \rho_c, \tag{5.127}$$

where ρ_c is the distance between the caustic at the edge and a second caustic of diffracted rays which equals to r_i, as illustrated in figure 5.39 for a general edge. For spherical wave incidence, with the substitutions of $r_1 = a$, $r_2 = \infty$, $s' = r_i$, and $\theta_1 = \frac{\pi}{2} - \theta_i$ in equation (A-9) of [15], the principal radii are

$$\rho_1^r = \frac{r_i + a}{a + 2r_i \cos \theta_i}, \tag{5.128}$$

$$\rho_2^r = r_i. \tag{5.129}$$

This gives

$$L^i = \frac{r_i r_d}{r_i + r_d} \tag{5.130}$$

and

$$L^r = \frac{\rho_1^r r_d}{\rho_1^r + r_d}. \tag{5.131}$$

In the diffraction coefficient,

$$a(\psi \pm \psi') = 2\cos^2(\frac{\psi \pm \psi'}{2}) \tag{5.132}$$

and

$$F(x) = 2j\sqrt{x}\exp(jx)\int_{\sqrt{x}}^{\infty}\exp(-j\tau^2)d\tau. \tag{5.133}$$

The incident angle and diffraction angle are given by

$$\psi = \arctan\frac{x_e - x}{y - y_e} + \frac{\pi}{2} - \alpha_o, \tag{5.134}$$

$$\psi' = \arctan\frac{x_e - x'}{y' - y_e} + \frac{\pi}{2} - \alpha_o \tag{5.135}$$
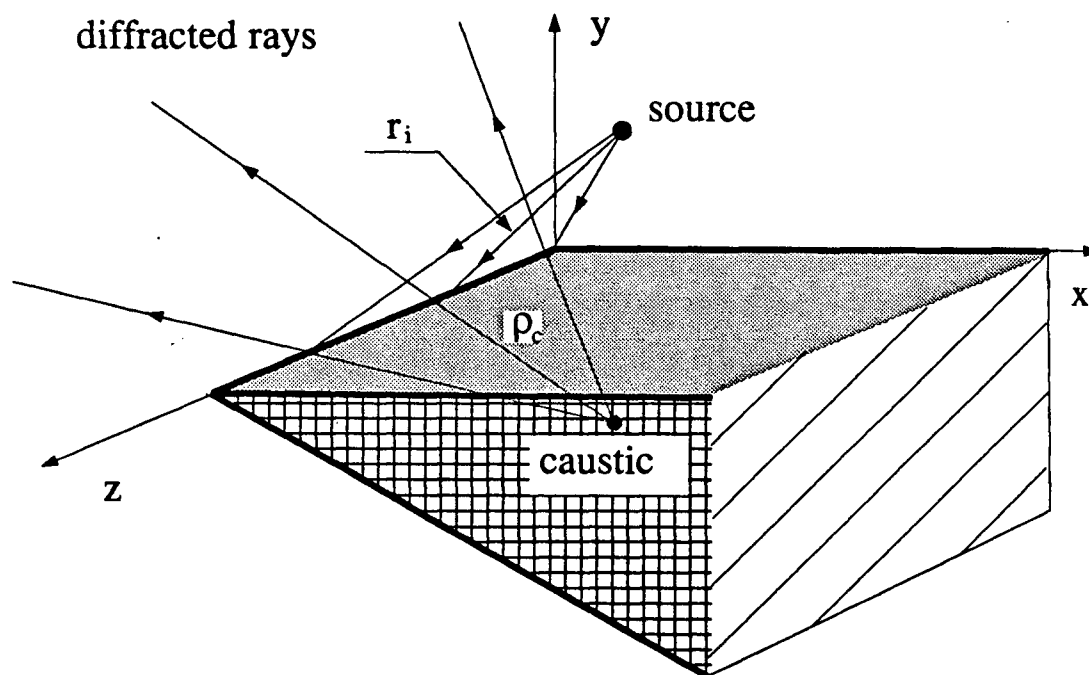
Figure 5.39: Geometry of the second caustic of the diffracted rays.

and

$$\theta_i = |\frac{\pi}{2} - \psi'|. \tag{5.136}$$

When x is small,

$$F(x) \approx \sqrt{\pi x} \exp[-j(\frac{\pi}{4} + x)]. \tag{5.137}$$

Using the above equations, it can be shown that the diffracted field is one half of the reflected field and changes its sign across the reflection boundary. This property makes the total field continuous across the reflection boundary.

Near grazing incidence, $\psi' \to 0$, and equation 5.124 cannot be used. Under this circumstance, the diffraction coefficient equation 5.124 should be multiplied by the transition coefficient $C(\sigma)C(\sigma')$ which is given by [26]

$$C(\sigma) = \frac{1}{2} \exp(-j\sigma^3/3)g(\sigma), \tag{5.138}$$

where $g(x)$ is the well-known Fock function [28] and $\sigma = ms/a$. Here a is the radius of the curved surface and $m = (ka/2)^{1/3}$. s is given by the following equations:

$$y_{Q_1} = \frac{-[x^2a + ay(a+y)] + xa\sqrt{x^2 + 2y^2a + y^2}}{x^2 + (a+y)^2}, \tag{5.139}$$

$$x_{Q_1} = -\sqrt{-2ay_{Q_1} - y_{Q_1}{}^2}, \tag{5.140}$$

$$\varphi = \arctan \frac{a + y_{Q_1}}{-x_{Q_1}} - \arctan \frac{a + y_e}{-x_e}, \tag{5.141}$$

$$s = \varphi a. \tag{5.142}$$

The Fock function $g(x)$ is tabulated in [28], but it is inconvenient in the computer program to use a table. Here a least-squares polynomial approximation is used instead. Figure 5.40 shows the amplitude and phase of the Fock function $g(x)$ along with the approximations.
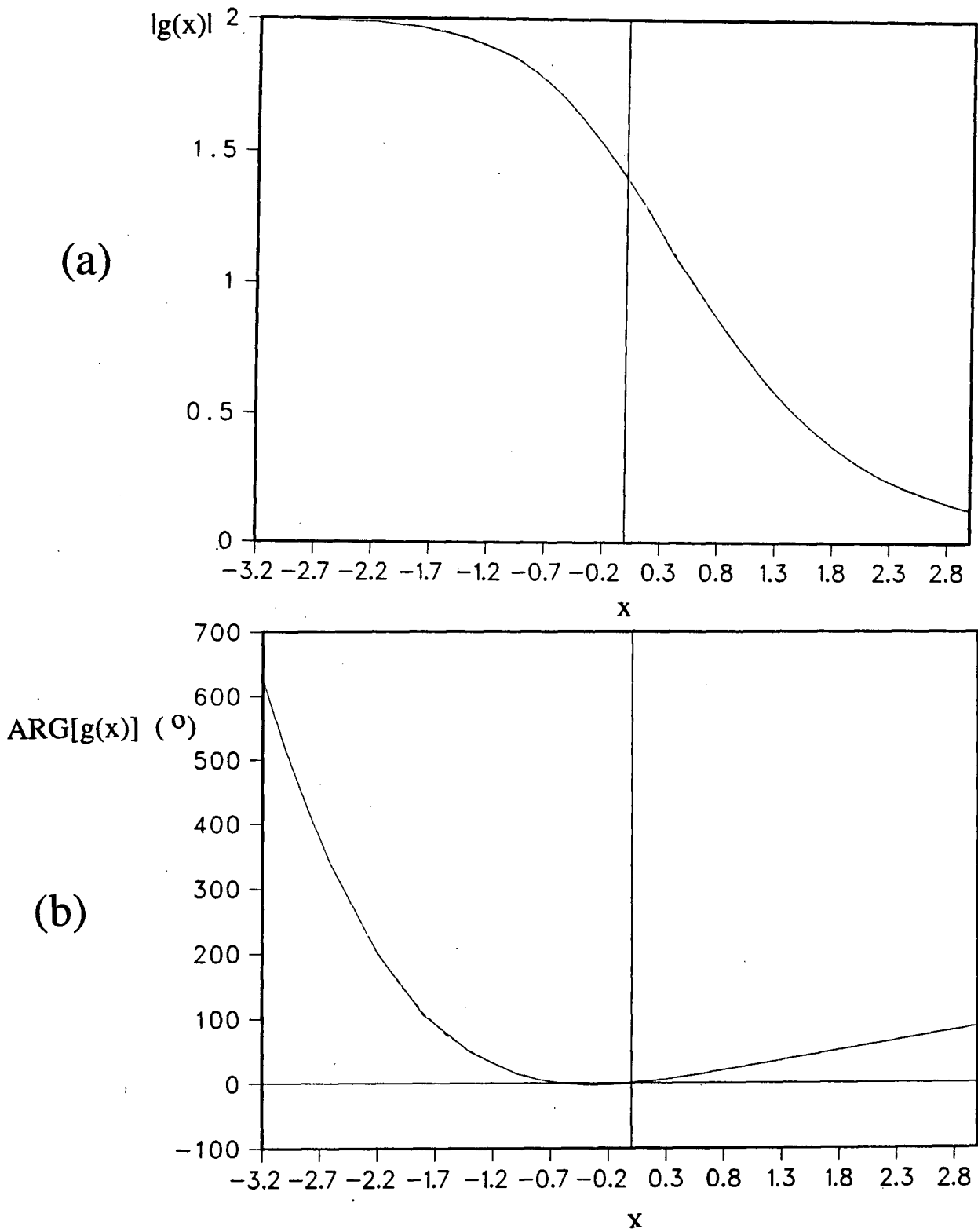
Figure 5.40: Approximation of the Fock function $g(x)$. Solid curves are data from Logan's table, dashed curves are the polynomial approximations. a: amplitude of $g(x)$; b: phase of $g(x)$.

5.4 Creeping Wave Diffraction

The study of creeping wave diffraction by the GTD method was carried out by Levy and Keller [21] in 1959. By comparing the GTD result and the high frequency asymptotic expansion of the rigorous solution of diffraction by cylinder and sphere, they obtained the diffraction coefficient and attenuation constant of the creeping wave. With these diffraction coefficients and attenuation constants, the high frequency diffraction problems for smooth scattering objects can be solved.

Diffraction at an edge of a curved surface has been studied by Idemen and Erdogan [23] extensively. By solving a second order canonical diffraction problem, they rigorously derived diffraction coefficients necessary to determine the excitation of the diffracted space ray and creeping wave by the edge of cylindrically curved surface. Whenever comparison is possible, these diffraction coefficients are identical to the previously derived ones.

In this section the results of Levy and Keller [21], Idemen and Erdogan [23] are combined to determine creeping wave diffraction by the curved segment. Because only the convex side of the curved screen is considered, whispering gallery modes may be neglected. There are three types of diffraction at the edge E; that is, creeping wave to creeping wave diffraction, creeping wave to space ray diffraction and space ray to creeping wave diffraction, as illustrated in figures 5.41, 5.43 and 5.44 respectively.

First considering the case in figure 5.41, the space ray is incident tangentially on the diffraction point Q_1, and is transformed to the infinite modes of a creeping wave. The creeping wave modes travel along the surface of the cylinder and shed space rays tangentially. At the edge E, the incident creeping wave modes are diffracted back with a diffraction coefficient. As diffracted creeping waves travel back to the point P_1, they are shed again tangentially to the observation point P.
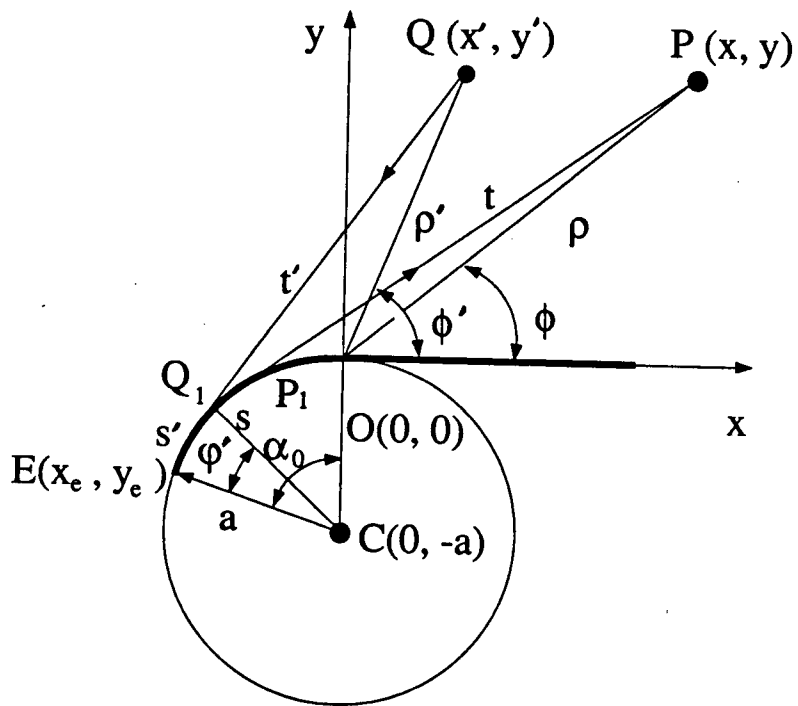
Figure 5.41: Coordinates for creeping wave diffraction.
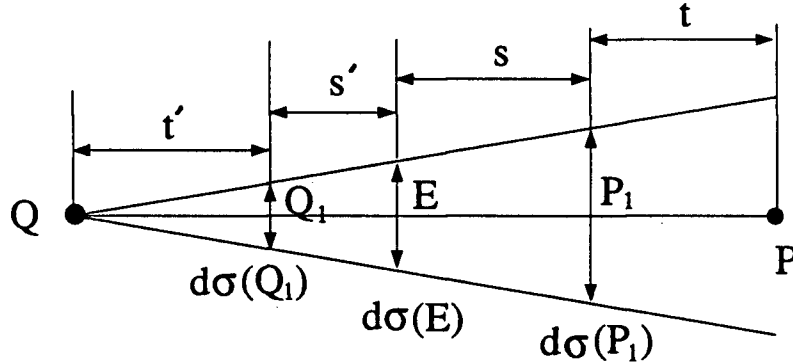
Figure 5.42: The diffracted ray tube.

In the following, only the leading mode in the series is considered. Its result easily can be generalized to higher order modes. According to GTD [21], the diffracted field can be expressed as:

$$u^{cdc} = u^i(Q_1)D'(Q_1)D''(E)D'(P_1)\sqrt{\frac{d\sigma(Q_1)}{d\sigma(E)}}\sqrt{\frac{d\sigma(E)}{d\sigma(P_1)}} \tag{5.143}$$

$$\times \sqrt{\frac{\rho_1}{t(\rho_1+t)}} \exp\left[-jk(s'+s+t)-A(s+s')\right] \tag{5.144}$$

where $u^i(Q_1)$ is the incident field at Q_1, $d\sigma$ is the cross-sectional area of the diffracted ray tube, as illustrated in figure 5.42, and ρ_1 is the principal radius of the curvature of the incident wavefront through P_1. s, s' and t, t' are indicated in figure 5.44 The diffraction coefficients depend on the nature of the field, the properties of the object at the diffraction point and the propagation constant k. The diffraction coefficient of the space ray to creeping ray and the attenuation constant are given by Levy and Keller [21]. The edge diffraction coefficient is given by Idemen and Erdogan [23].

With the same incident field and some geometrical manipulations, the GTD solution of the diffracted creeping wave is

$$u^{cdc}(P) = D'(Q_1)D''(P_1)D'(E)\exp[-A(s+s')]\frac{\exp[-jk(s'+t'+s+t)]}{\sqrt{tt'}\sqrt{(s'+t'+s+t)}}, \qquad (5.145)$$

where

$$t' = \sqrt{x'^2 + (y'+a)^2 - a^2}. \qquad (5.146)$$

s' can be determined by the following set of equations:

$$y_{Q_1} = \frac{-[x'^2 a + ay'(a+y')] + x'a\sqrt{x'^2 + 2y'^2 a + y'^2}}{x'^2 + (a+y')^2}, \qquad (5.147)$$

$$x_{Q_1} = -\sqrt{-2ay_{Q_1} - y_{Q_1}{}^2}, \qquad (5.148)$$

$$\varphi' = \arctan\frac{a+y_{Q_1}}{-x_{Q_1}} - \arctan\frac{a+y_e}{-x_e}, \qquad (5.149)$$

$$s' = \varphi'a, \qquad (5.150)$$

t and s can be obtained by replacing x', y' with x and y in equations 5.146 to 5.150. The diffraction coefficients of the smooth surface are given by [21]

$$D'^2(Q_1) = D'^2(P_1) = \frac{-\exp(-j\frac{\pi}{12})}{\sqrt{2\pi ka_1'}A_i^2(a_1')}(\frac{ka}{2})^{\frac{1}{3}}, \qquad (5.151)$$

and the edge diffraction coefficient for creeping wave is [23]

$$D''(E) = \frac{jka}{4v_1'(v_1' - ka)}, \qquad (5.152)$$

with

$$v_1' = ka - a_1'(\frac{ka}{2})^{\frac{1}{3}}\exp(-j\frac{\pi}{3}), \qquad (5.153)$$

where a_1' satisfies $A_i'(a_1') = 0$ and $A_i(x)$ is the Airy function and $A_i'(x) = dA_i'(x)/dx$. $u(P)$ equals zero, when

$$\arctan\frac{x-x_e}{y-y_e} \geq \alpha_o. \qquad (5.154)$$
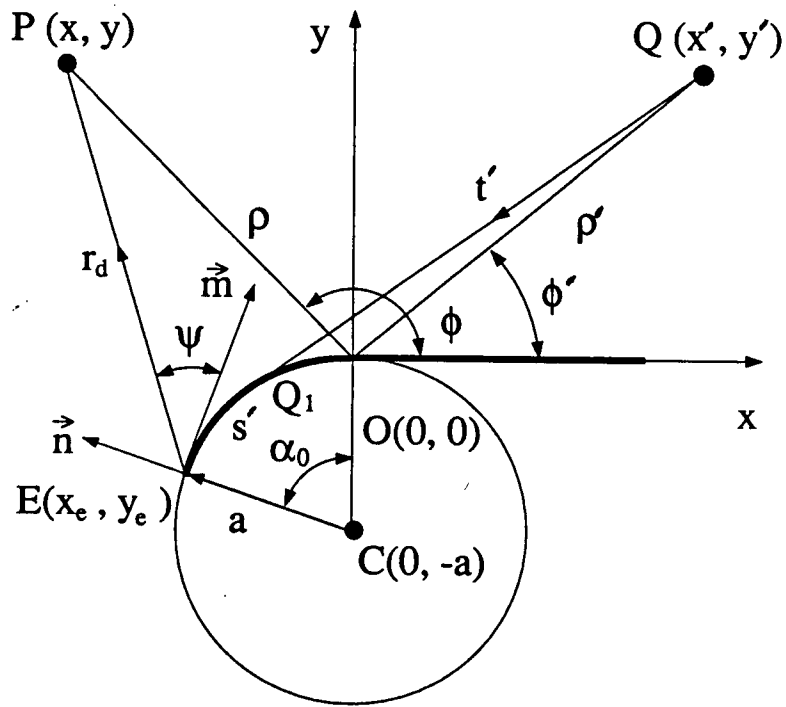
Figure 5.43: Coordinates for the edge diffracted space ray.

The attenuation constant A is given by

$$A = -\frac{a_1}{a}\left(\frac{ka}{2}\right)^{\frac{1}{3}}\exp(j\frac{\pi}{6}).$$ (5.155)

Similarly for the case in figure 5.43, the diffracted creeping wave is

$$u(P) = D'(Q_1)D''(E)\exp\left(-As'\right)\frac{\exp[-jk(s'+t'+r_d)]}{\sqrt{t'r_d(t'+s'+r_d)}},$$ (5.156)

where

$$D''(E) = -\frac{\exp(-j\frac{3\pi}{8})}{(8\pi)^{\frac{1}{4}}}\frac{ka\sqrt{1+\cos\psi}}{(v_1'+ka\cos\psi)\sqrt{v_1'-ka}}$$ (5.157)

$$r_d = \sqrt{(x-x_e)^2+(y-y_e)^2},$$ (5.158)

$D(Q_1)$ is the same as equation 5.151 and ψ is shown in figure 5.43.

For figure 5.44, reciprocity can be used and the result is

$$U(P) = D'(P_1)D(E)\exp\left(-As\right)\frac{\exp[-jk(s+t+r_i)]}{\sqrt{tr_i(t+s+r_i)}},$$ (5.159)

with

$$r_i = \sqrt{(x'-x_e)^2+(y'-y_e)^2},$$ (5.160)

and $D(P_1)$ is the same as given by equation 5.151.

Equations 5.151 and 5.152 give the leading order of the diffraction coefficients. Away from the grazing incidence, these leading order terms are sufficient. But close to the grazing incidence, higher order terms must be included. These higher order terms can be obtained by the replacement of a_1' and v_1' in equations 5.151 and 5.152 by a_n' and v_n' with $n = 1, 2, \cdots$, where a_n' satisfies $A_i'(a_n') = 0$, and v_n' is given by 5.153 with subscript 1 being replaced by n.

Near grazing incidence, using Michaeli's [25] result, the following solution in term of the Fock function can be obtained:

$$u(P) = -\frac{\exp(-j\pi/4)}{4\sqrt{2\pi k}}g(\sigma')g(\sigma)\frac{\exp[-jk(s'+t'+s+t)]}{\sqrt{tt'}\sqrt{(s'+t'+s+t)}}.$$ (5.161)
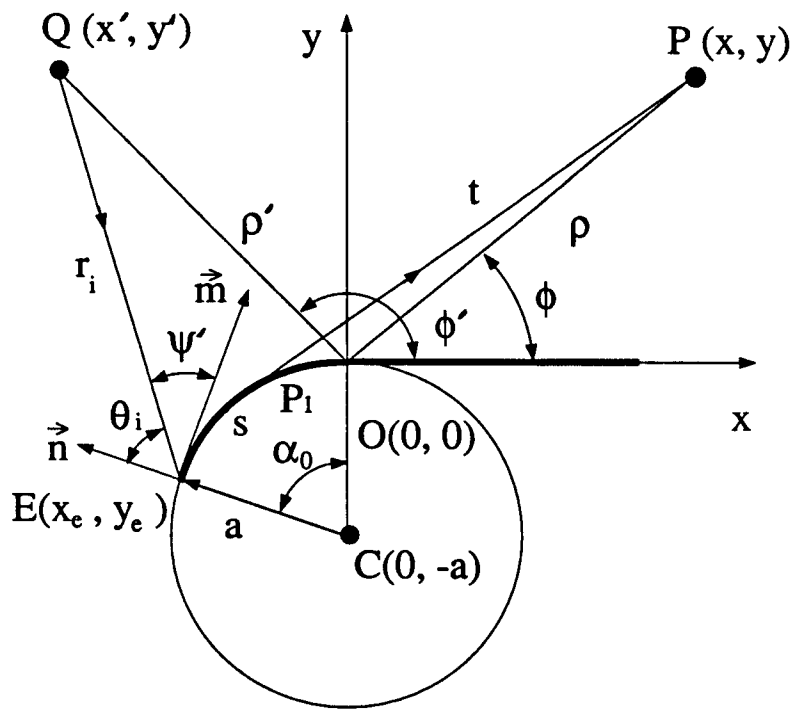
Figure 5.44: Coordinates for the edge diffracted creeping wave.

In order to examine diffraction in the transition region, the diffracted fields near grazing incidence are ploted in figure 5.45 for both GTD and Fock function solutions. For $a/\lambda =2, 20, 100$, the corresponding angular transition regions are approximately equal to $31°$, $14°$ and $8°$. The GTD results are represented by the solid curves and the solutions in term of the Fock function are dashed curves. The GTD solution gives finite diffracted fields, but has a discontinuity in the transition region. The Fock function solution changes smoothly from the edge diffracted space ray to the creeping wave diffracted space ray. On the boundaries of the transition region, the two solutions are identical. It is interesting to notice that the creeping wave diffraction converges even in the transition region. Here 15 terms are included in the calculation of the creeping wave diffraction.

5.5 Diffraction by the Second Order Edge

The diffraction by the second order edge, where the radius of the surface curvature has a discontinuity, is of higher order of the inverse power of the propagation constant, but it is still significant near the reflection boundary. Weston [30] first studied the effect of a discontinuity in curvature on the high frequency scattering. He modelled the problem by the conjunction of two parabolic cylinders and solved the current distribution asymptotically. Senior extended Weston's work by extracting the diffraction coefficient from the asymptotic expansion. Senior's result is non-uniform and invalid in the vicinity of the reflection boundary where diffraction plays a vital role. Later, James [32] derived a uniform version of the diffraction coefficient for the edge formed by smoothly joined cylinders based on both the theory of physical optics and Senior's result. James' result gives correct diffraction on the reflection boundary and retains Senior's result away from the reflection boundary. In this section, the diffraction coefficient derived by James' method is used to construct the diffracted field by the second order edge.
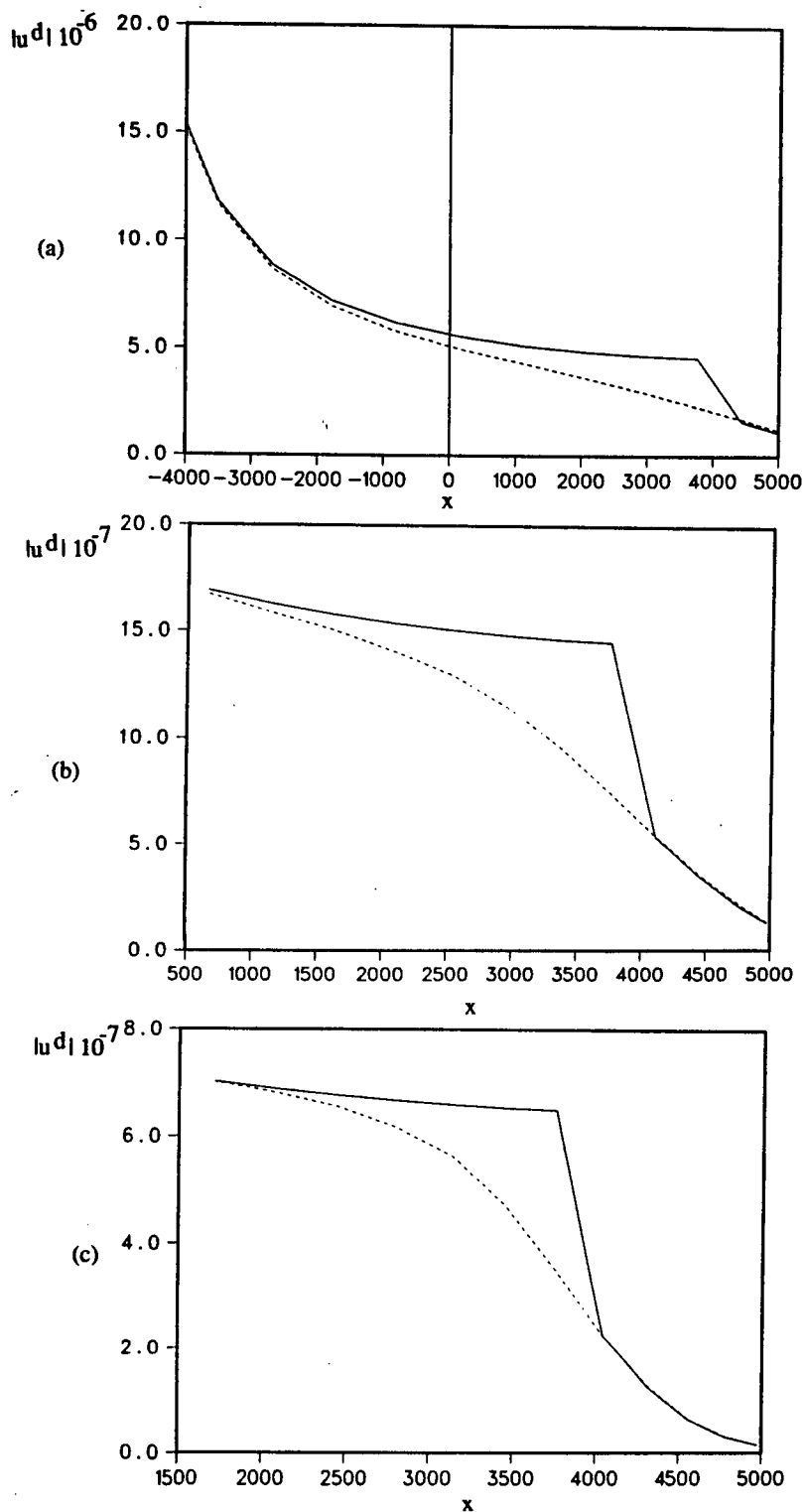
Figure 5.45: Diffraction in the transition regions for grazing incidence. The solid curves are GTD solutions and the dashed curves are Fock function solutions. a: $a/\lambda = 2$; b: $a/\lambda = 20$; c: $a/\lambda = 100$.

Using GTD and figure 5.35, the diffraction of the second order edge is given by

$$u^{ds} = u^i D_s \sqrt{\frac{\rho'}{(\rho + \rho')\rho}} \exp(-jk\rho), \qquad (5.162)$$

where the incident field is the same as before. The diffraction coefficient is obtained by James' method and is given by

$$D_s = \frac{-4(1 + \cos\phi\cos\phi')\exp(-j\frac{\pi}{4})}{jka\sqrt{8\pi k}(\cos\phi + \cos\phi')^3}, \qquad (5.163)$$

if $v_{h,c} > 3$,

$$D_s = (D_h - D_c)\frac{2(1 + \cos\phi\cos\phi')}{1 + \cos(\phi - \phi')}, \qquad (5.164)$$

if $v_{h,c} < 3$, where

$$\begin{aligned}
D_h \;=\; & \frac{-\exp(-j\frac{\pi}{4})}{\sqrt{8\pi k}}\{j\,\mathrm{sgn}(\cos\phi' + \cos\phi) \\
& \times [2\sin\phi + 3\cot\phi(\cos\phi' + \cos\phi)]\exp(jv_h^2) \\
& \times\sqrt{2Lk}\frac{F_n(v_h)}{\sin\phi} - 3\cot\phi\,\}
\end{aligned} \qquad (5.165)$$

$$\begin{aligned}
D_c \;=\; & \frac{-2\exp(-j\frac{\pi}{4})}{\sqrt{8\pi k}}\{\,j\,\mathrm{sgn}(\cos\phi' + \cos\phi)\sqrt{2ka} \\
& \times [\sin\phi + \frac{\cos\phi(1 + \frac{3a}{2L}\sin\phi)(\cos\phi' + \cos\phi)}{\sin\phi' + \sin\phi(1 + \frac{a}{L}\sin\phi)}] \\
& \times \exp(jv_c^2)\frac{F_n(v_c)}{\sqrt{\sin\phi' + \sin\phi(1 + \frac{a}{L}\sin\phi)}} \\
& -\frac{\cos\phi(1 + \frac{3a}{2L}\sin\phi)}{\sin\phi' + \sin\phi(1 + \frac{a}{L}\sin\phi)}\,\},
\end{aligned} \qquad (5.166)$$

in which the Fresnel integral is defined by

$$F_n(x) = \int_x^\infty \exp(-jt^2)dt \qquad (5.167)$$

and the distance parameters are given by

$$L = \frac{\rho\rho'}{\rho + \rho'}, \qquad (5.168)$$

$$v_h = \sqrt{\frac{kL}{2}} \frac{|\cos\phi' + \cos\phi|}{\sin\phi}, \tag{5.169}$$

$$v_c = \sqrt{\frac{ka}{2}} \frac{|\cos\phi' + \cos\phi|}{\sqrt{\sin\phi' + \sin\phi(1 + \frac{a}{L}\sin\phi)}}. \tag{5.170}$$

5.6 Time-Domain Solution

Single pulse diffraction by the curved half-plane can be easily constructed by Fourier transforming the frequency-domain solution. The pulse is shown in figure 2.10. This pulse has a weak low frequency content; to minimize errors originating from the high frequency assumption of GTD. The parameters are $a = 8 \times 10^2 m$, $h = 4 \times 10^3 m$, $\alpha_o = 45°$ and the pulse velocity equals $4 \times 10^3 m/s$. The source and field point are changing from $\phi' = \phi = 30°$ to $150°$, as shown in figure 5.46. The results of the total field and the diffracted field are shown in figure 5.47 and 5.48 respectively. In order to test the above theoretical predication, an acoustic model of a curved half-plane was designed. The model was constructed in the departmental shop. The test equipment set up and the measurement was done by Mellema [43]. The measured acoustic pulse incidence response is shown in figure 5.49 and a median filtered result is shown in figure 5.50. The median filtered result revealed a continued response of the edge diffracted space ray and creeping wave as predicated by the theory. The second order diffraction at the joint of the half-plane and the quarter of the circular cylinder is not evident in these result, but traces of the diffraction might be found with more selective apparatus and filtering of interaction between source and target. It is very difficult to distinguish the diffraction from the noise in figures 5.49 and 5.50. At this stage, direct quantitative comparison is not possible, but these results show that the theoretical predication of the creeping wave and second order edge diffraction is in agreement with the experimental results.

In figure 5.47, the earliest arriving pulses of traces 1 to 21 are reflections from the
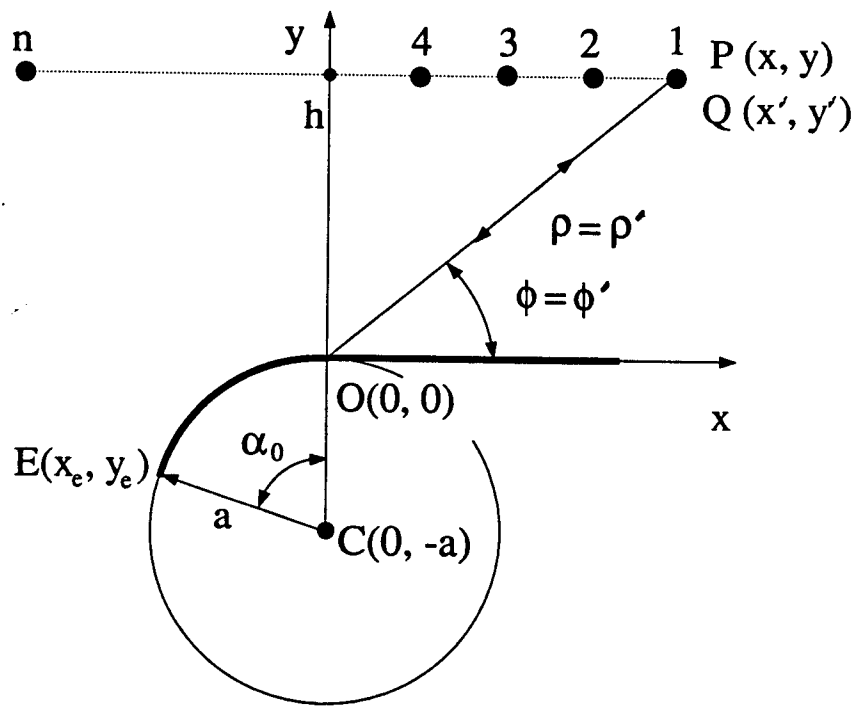
Figure 5.46: Coordinates of a source and receiver array over a curved half plane.
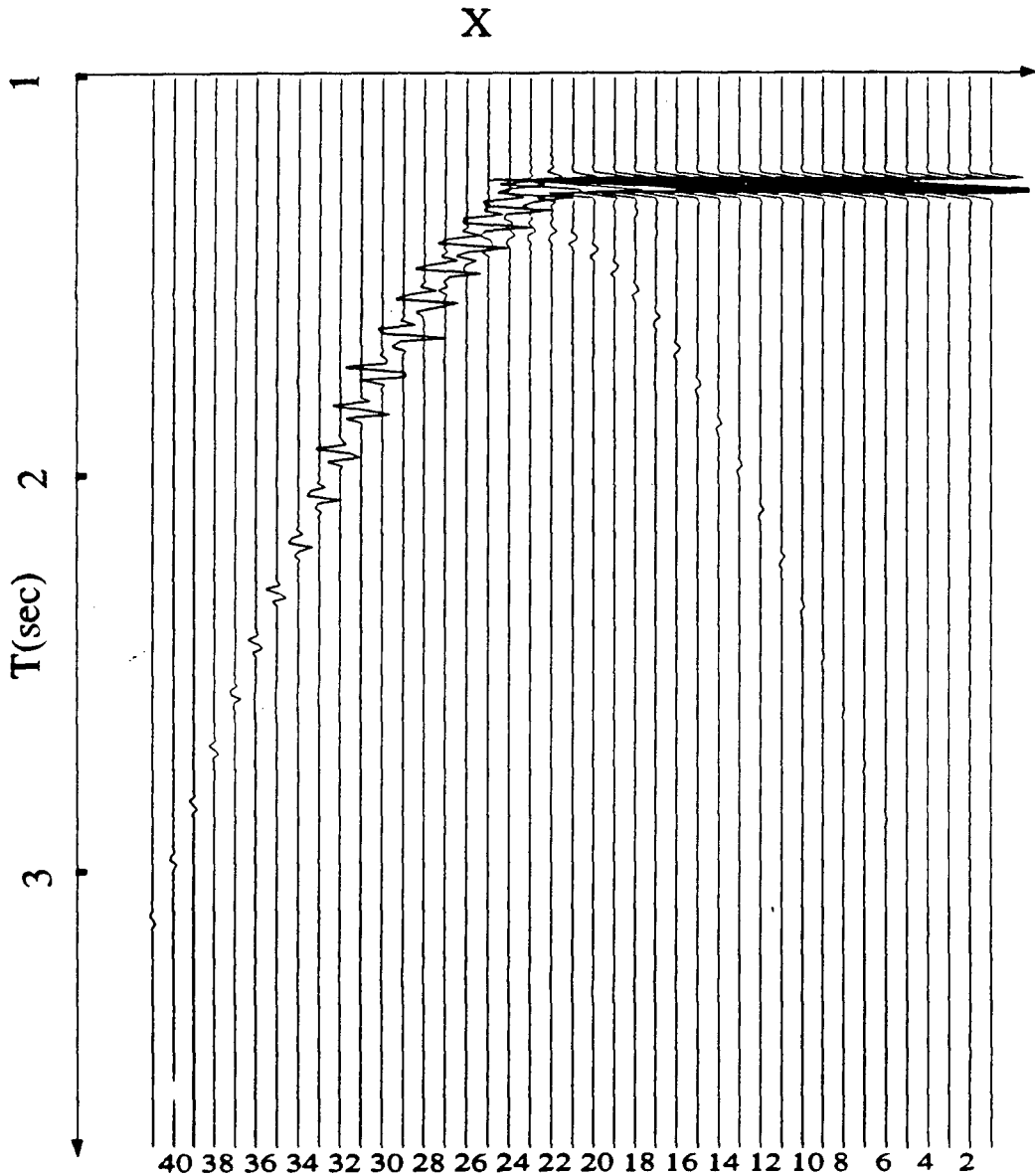
Figure 5.47: Calculated total scattered pulses from a curved half-plane for zero offset source-receiver pairs. $a=8\times10^2$m, $h=4\times10^3$m, $\alpha_0 = 45°$ and pulse velocity is 4×10^3m/s. The spacing of traces is 346m and trace number 1 is started at x=6928m.
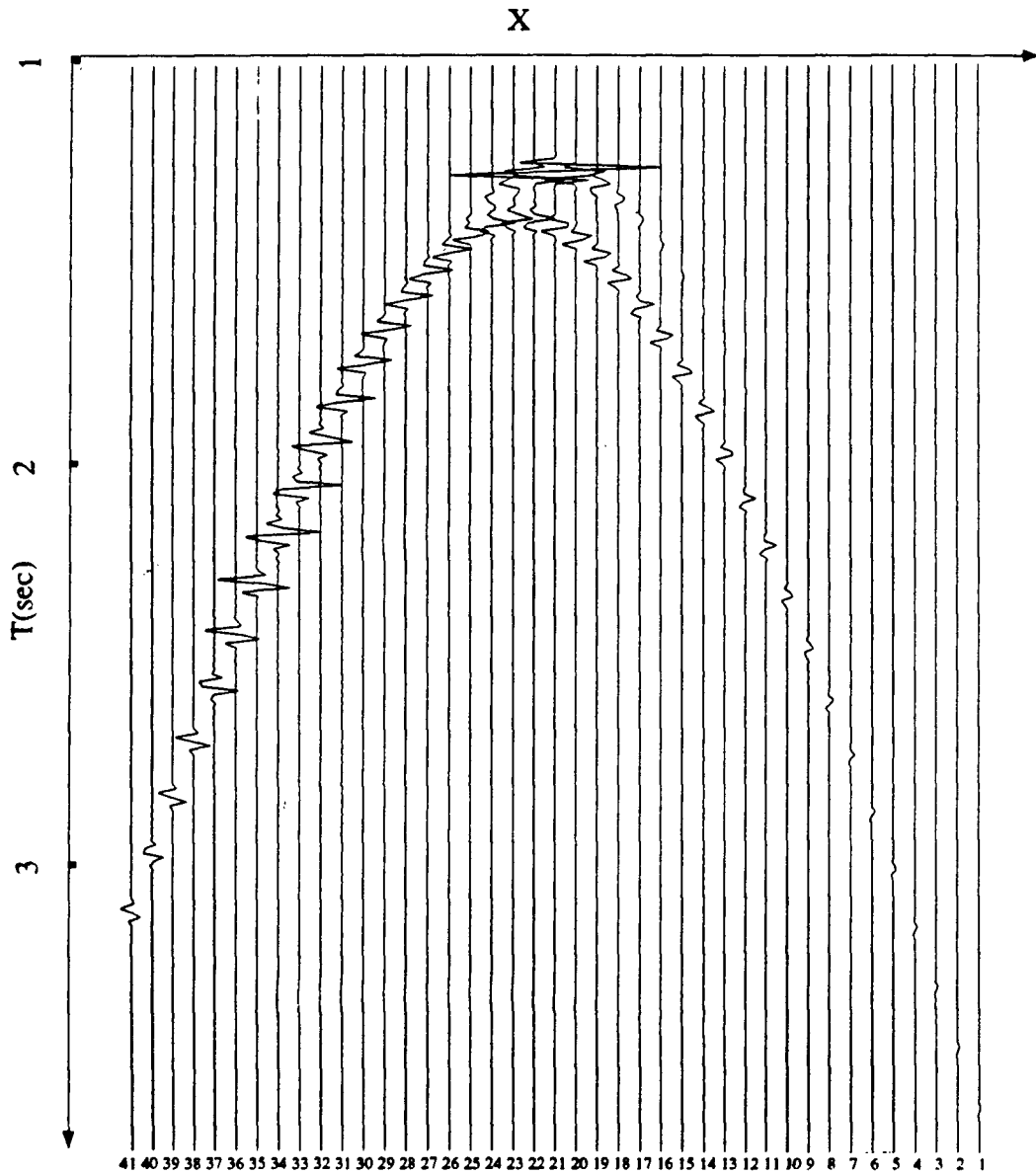
Figure 5.48: Diffracted pulses of figure 5.47.
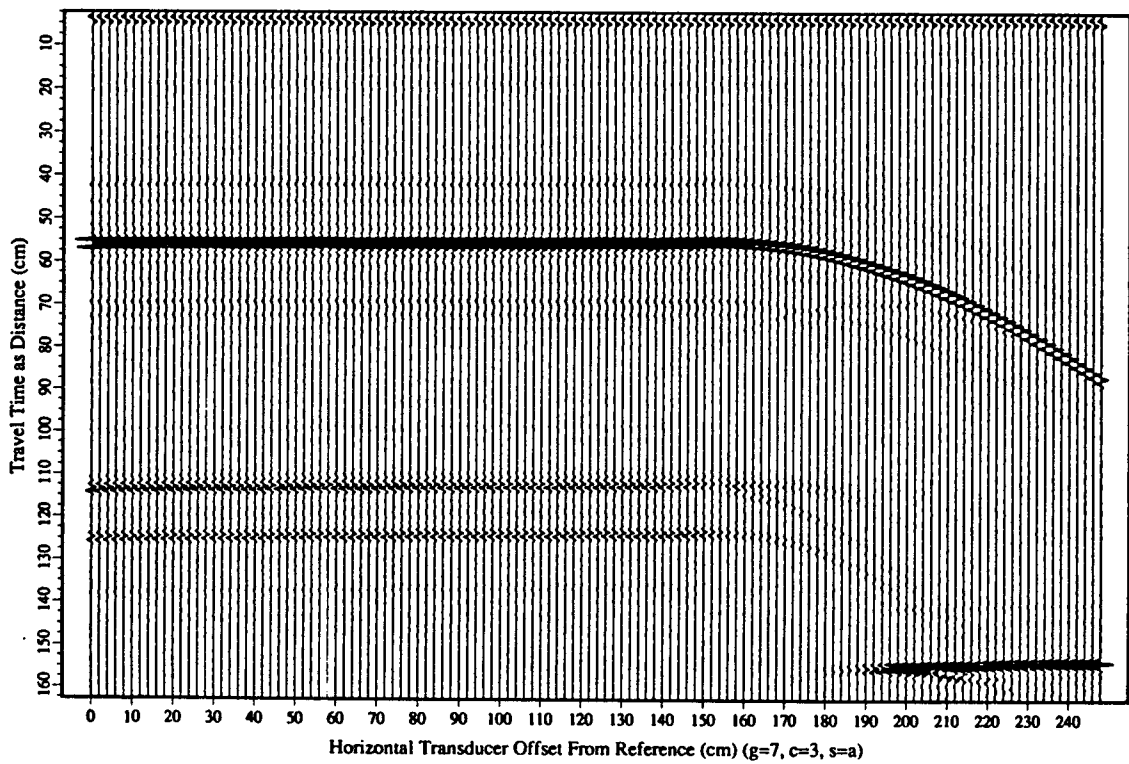
Figure 5.49: Measured acoustic reflection and diffraction by a curved half-plane. Courtesy of Mellema [43].
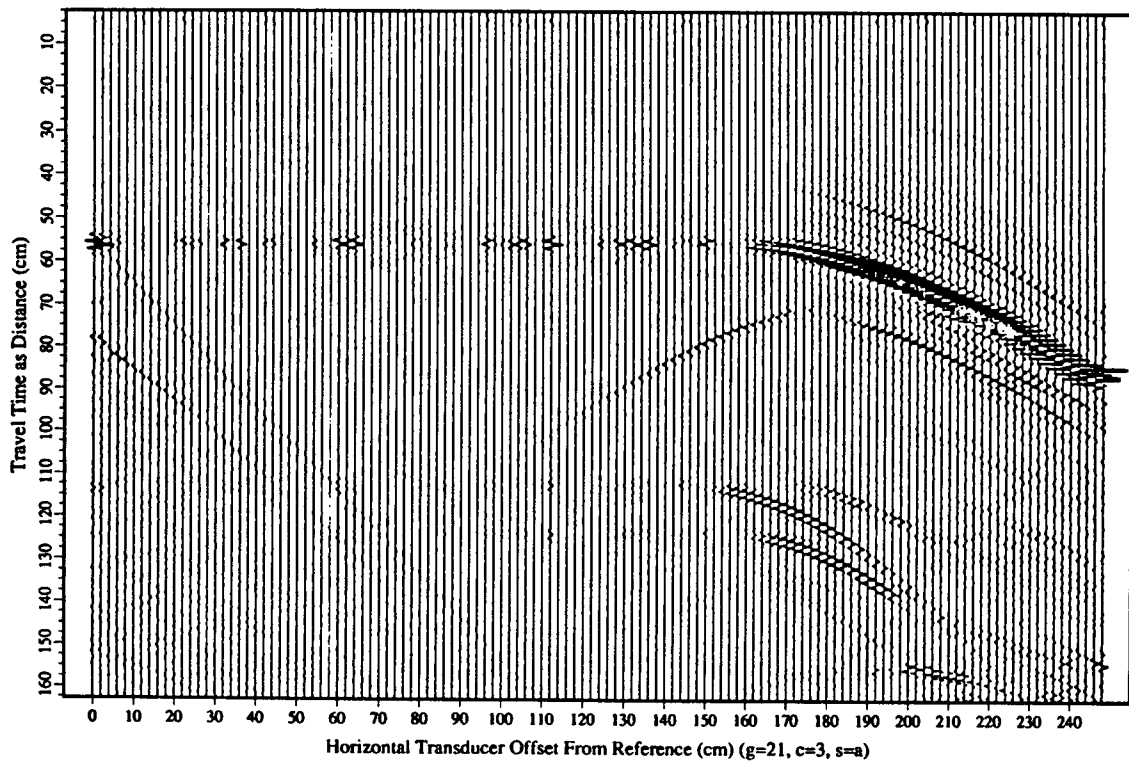
Figure 5.50: Median filtered result of figure 5.49 for acoustic reflection and diffraction by a curved half-plane. Courtesy of Mellema [43].

half-plane. Further on in the plot (traces 22 to 34), reflection from the curved segment is separated in time from diffraction by the edge E initially, but these two fields merge into one on the reflection boundary. Across the reflection boundary (between trace 34 and 35), reflection vanishes and the total field continues in the form of the edge diffraction. In figure 5.48, the diffracted field changes its phase on the reflection boundary. This behaviour of the diffraction field makes the total field change smoothly. In figure 5.48, right above the second order edge (trace 21), the second order edge diffraction arrives first and is larger in magnitude than the first order edge diffraction. When the field point moves away from the reflection boundary, the second order edge diffraction fades rapidly. The creeping wave diffraction in the first several traces are plotted separately in figure 5.51. Creeping wave diffraction alone is responsible for those pulses in trace 1 to trace 10. The first order edge diffractions start at trace 11. At the shadow boundary of the edge diffracted space ray, the diffracted field changes continuously from direct edge diffraction to creeping wave diffraction. The latter is much smaller in magnitude.

5.7 Conclusion

In this chapter high frequency scattering property by a cylindrically curved half-plane is studied. This solution can correctly predict not only the first order edge diffracted space ray, but also the second order edge diffracted space ray and the creeping wave which has been missing in previous solutions. By using the Fock function in the transition region of the grazing incidence, the total diffracted field changes uniformly from the direct edge diffraction to the creeping wave diffraction.
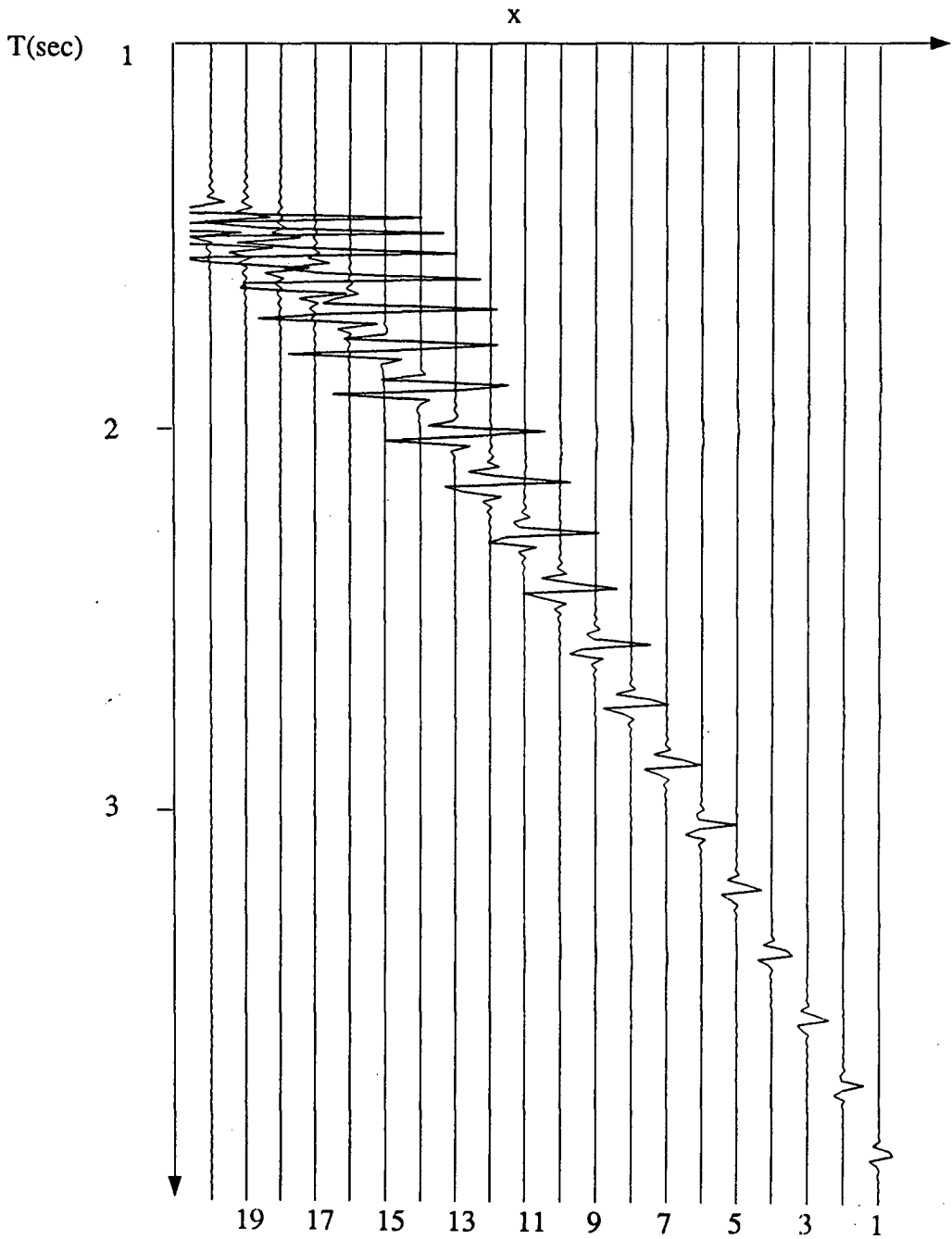
Figure 5.51: Diffracted space ray and creeping wave pulses from figure 5.47.

Chapter 6

CONCLUSIONS

6.1 Conclusions

The geometrical theory of diffraction in electromagnetics is used to derive the solutions of the spherical wave diffraction by a 90° step, two offset half-planes, an inclined step and a curved surface. These solutions are more accurate and efficient than previous ones based on Kirchhoff diffraction theory. Previous incorrect predictions of the diffraction phase shift at the edge and the amplitude symmetric hyperbola are corrected by the GTD solutions. The solution for the 90° step is further extended to beam source diffraction. This makes it possible to simulate the real source diffraction in electromagnetics and in geophysics. The beam diffraction solution can be further generalized to diffraction by other configurations.

For a 90° step, single diffraction and double diffraction are most important. Predicted by the theory, they can also be observed in the measurements. Triple diffraction is very weak in the analysis and has not been observed in the experimental results. Creeping wave diffraction is responsible for the diffraction received when the receiver is beyond the shadow boundary of the direct edge diffraction. The above conclusions have been confirmed by Mellema's acoustic scatter-mapping imaging system.

Time-domain infinite impulse response (IIR) filtering methods can have advantages over the frequency-domain approach which needs an inverse Fourier transformation to obtain the time-domain pulse solution. A 75% computing time saving can be achieved for

single diffraction. The same procedure can be applied to double diffraction, but the time saving will be less significant, since more IIR filters have to be designed to implement the convolution. The single and double diffraction coefficients in the time-domain are given explicitly in the thesis.

6.2 Future Work

Future work can be divided into two parts. One is the study of the similar models by rigorous methods and comparison with the solutions given here. The other is to use the solutions given here to construct solutions for more complex shapes.

The solution for low frequency diffraction by a 90° step with a plane wave incidence can be obtained by the method used by Jones [45], but the result will be only valid for a low step. The analysis for for arbitrary step height is difficult. Some preliminary works have been done in this area by the author, but much more effort is needed to complete the solution and to obtain some useful numerical results.

There is no rigorous solution for double diffraction by two edges with point source incidence and completely arbitrary source and receiver positions. This is difficult because, like single diffraction at a reflection or shadow boundary, the physical wave separates into diffraction and reflection terms in the analysis, but physically they are essentially the same at the reflection or shadow boundaries. The analysis is always difficult when the geometrical optics field and the diffracted field cannot be separated. The mathematical tools which can be applied to this problem are also very limited.

To apply the existing solution to more complex models and to generalize the solution to different waves and boundary conditions is more realistic. Different seismic models can be constructed to provide solutions for evaluating the different data processing methods and different filters. In the process of constructing the solutions for complex diffracting

bodies, the interaction between the edges must be taken into account.

Based on the present solutions and programs, a graphic interface software for the computation of the reflection and diffraction by complex shapes can be developed to meet the needs of different applications. The potential users would be scientists and engineers working in seismic imaging, engineers working in acoustic design and sound reproduction, and engineers working in radar scatter and nondestructive testing.

Bibliography

[1] A. W. Trorey: *A Simple Theory for Seismic Diffractions,* Geophysics Vol. 35, pp. 762-784, 1970.

[2] –: *Diffractions for Arbitrary Source-Receiver Locations,* Geophysics Vol. 42, pp. 1177-1182, 1977.

[3] F. J. Hilterman: *Three Dimensional Seismic Modelling,* Geophysics, Vol. 35, No. 6, pp. 1020-1037, December 1970.

[4] G. D. Hutton: *The Perfectly Reflecting Wedge Used as a Control Model in Seismic Diffraction Modelling,* Geophys. Prospecting, Vol. 35, pp. 681-699, 1987.

[5] M. A. Biot and I. Tolstoy: *Formulation of Wave Propagation in Infinite Media by Normal Coordinates with Application to Diffraction,* J. Acoust. Soc. Am., Vol. 29, pp. 381-391, 1957.

[6] A. Sommerfeld: *Mathematische Theorie der Diffraction,* Math. Ann., Vol. 47, pp. 317-374, 1896.

[7] H. M. Macdonald: *Electric Waves,* Cambridge University Press, Cambridge, England, 1902.

[8] –: *A Class of Diffraction Problems,* Proc. London Math. Soc. Vol. 14, pp. 410-427, 1915.

[9] H. S. Carslaw: *Diffraction of Waves by a Wedge of Any Angle,* Proc. London Math. Soc. Vol. 18, pp. 291-306, 1920.

[10] J. B. Keller: The Geometrical Optics Theory of Diffraction, McGill Symp. on Microwave Optics 1952, AFCL Rep., TR-59-118(II), 1959.

[11] –: *Geometrical Theory of Diffraction,* J. Opt. Soc. Am., Vol. 52, pp. 116-130, 1962.

[12] J. Boersma and P. H. M. Kersten: *Uniform Asymptotic Theory of Electromagnetic Diffraction by a Plane Screen,* Dept. Math., Tech. Univ. Eindhoven, Eindhoven, Netherlands (in Dutch), Tech. Rep., 1967.

[13] R. M. Lewis and J. Boersma: *Uniform Asymptotic Theory of Edge Diffraction,* J. Math. Phys., Vol. 10, pp. 2291-2305, 1969.

[14] D. S. Ahluwalia, R. M. Lewis and J. Boersma: *Uniform Asymptotic Theory of Diffraction by a Plane Screen,* SIAM J. Appl. Math., Vol. 16, pp. 783-807, 1968.

[15] R. G. Kouyoumjian and P. H. Pathak: *An Uniform Geometrical Theory of Diffraction for an Edge in a Perfectly Conducting Surface,* Proc. IEEE, Vol. 62, pp. 1448-1461, 1974.

[16] R. Mittra, Y. Rahmat-Samii and W. L. Ko: *Spectral Theory of Diffraction,* Appl. Phys., Vol. 10, pp. 1-13, 1976.

[17] Y. Rahmat-Samii and Mittra: *Spectral Analysis of High-Frequency Diffraction of an Arbitrary Incident Field by a Half Plane–Comparison with Four Asymptotic Techniques,* Radio Science, Vol. 13, pp. 31-48, 1978.

[18] S. W. Lee and J. Boersma: *Ray-Optical Analysis of Fields on Shadow Boundaries of Two Parallel Plates,* J. Math. Phys., Vol. 16, pp. 1746-1764, 1975.

[19] R. Tiberio and R. G. Kouyoumjian: *An Analysis of of Diffraction at Edges Illuminated by Transition Region Fields,* Radio Science, Vol. 17, pp. 323-336, 1982.

[20] –: *Calculation of the High-Frequency Diffraction by Two Nearby Edges Illuminated at Grazing Incidence,* IEEE Trans. on Antennas and Propagat., Vol. AP-32, No. 11, Nov. 1984.

[21] B. R. Levy and J. B. Keller: *Diffraction by a Smooth Object,* Commun. Pure Appl. Math., Vol. 12, pp. 159-209, 1959.

[22] N. C. Albertsen and P. L. Christiansen: *Hybrid Diffraction Coefficients for First and Second Order Discontinuities of Two-Dimensional Scatterers,* SIAM J. Appl. Math., Vol. 34, No. 2, pp. 389-414, March 1978.

[23] M. Idemen and E. Erdogan: *Diffraction of the Creeping Waves Generated on a Perfectly Conducting Spherical Scatterer by a Ring Source,* IEEE Trans. on Antennas. and Propagat., Vol. AP-31, No.5, pp. 776-784, 1983.

[24] A. H. Serbest: *An Extension to GTD for an Edge on a Curved Perfectly Conducting Surface,* IEEE Trans. on Antennas and Propagat., Vol. AP-34, No. 6, pp. 837-841, June 1986.

[25] A. Michaeli: *Transition Functions for High-Frequency Diffraction by a Curved Perfectly Conducting Wedge, Part I: Canonical Solution for a Curved Sheet,* IEEE Trans. on Antennas and Propagat., Vol. AP-37, No. 9, pp. 1073-1079, Sept. 1989.

[26] –: *Transition Functions for High-Frequency Diffraction by a Curved Perfectly Conducting Wedge, Part II: A Partially Uniform Solution for a General Wedge Angle,* IEEE Trans. on Antennas and Propagat., Vol. AP-37, No. 9, pp. 1080-1085, Sept. 1989.

[27] –: *Transition Functions for High-Frequency Diffraction by a Curved Perfectly Conducting Wedge, Part III: Extension to Overlapping Transition Regions,* IEEE Trans. on Antennas and Propagat., Vol. AP-37, No. 9, pp. 1086-1092, Sept. 1989.

[28] N. A. Logan: *General Research in Diffraction Theory,* Vol. 1, 2, LMSD-288087, 288088, Missiles and Space Div., Lockheed Aircraft Corp., 1959.

[29] V. A. Fock: *Electromagnetic Diffraction and Propagation Problems,* Pergamon Press, New York, 1965.

[30] V. H. Weston: *The Effect of a Discontinuity in Curvature in High-frequency Scattering,* IRE Trans.on Antennas and Propagat., Vol. AP-10, pp. 775-580, November 1962.

[31] T. B. A. Senior:*The Diffraction Matrix for a Discontinuity in Curvature,* IEEE Trans. on Antennas and Propagat., Vol. AP-20, No. 3, pp. 326-333, May 1972.

[32] G. L. James: *Geometrical Theory of Diffraction for Electromagnetic Waves,* Peter Peregrinus Ltd., 1976.

[33] A. J. M. Soares and A. J. Giarola: *Plane Wave Scattering by a Step Discontinuity in a Conducting Plane,* ISAE'85-7-3, Beijing, Aug. 1985.

[34] G. A. Suedan and E. V. Jull: *Beam Diffraction by Half Planes and Wedges: Uniform and Asymptotic Solutions,* J. of Electromagnetic Waves and Applics., Vol. 3, No. 1, pp. 17-26, 1989.

[35] J. R. Wait: *Diffraction of a Spherical Wave PUlse by a Half-Plane Screen,* Can. J. Phys., Vol. 35, pp. 693-696, 1957.

[36] L. B. Felsen and N. Marcuvitz: *Radiation and Scattering of Waves,* Englewood Cliffs, NJ: Prentice Hall, 1973, chapter 6.

[37] D. R. Dalton and M. J. Yedlin: *ARMA Implementation of Diffraction Operators with Inverse-Root Singularities,* IEEE Trans. on Antennas and Propaga., Vol. 38, No. 6, pp. 831-837, 1990.

[38] D. R. Dalton and M. J. Yedlin: *Exact Time Domain Solutions for Acoustic Diffraction by a Half Plane,* Surveys in Geophys., Vol. 10, pp. 305-330, 1989.

[39] J. L. Shanks: *Recursion Filters for Digital Processing,* Geophysics, Vol. XXXII, No. 1, pp. 33-51, 1967.

[40] C. S. Burrus and T. W. Parks: *Time Domain Design of Recursive Digital Filters,* IEEE Trans. on Audio and Electroacoustics, Vol. AU-18, No. 2, pp. 137-141, June 1970.

[41] H. P. Berlage: *Seismometer, Handbuch der Geophysik,* Borntraeger, Vol. 4, pp. 299-526, 1930.

[42] S. Hong and V. H. Weston: *A Modified Fock Function for the Distribution of Currents in the Penumbra Region with Discontinuity in Curvature,* Radio Sci., Vol. 1 (new series), pp. 1045-1053, September 1966.

[43] G. R. Mellema: *An Acoustic Scatter-Mapping Imaging System,* M.A.Sc. thesis, Dept. of Electrical Engineering, University of British Columbia, 1990.

[44] G. M. Jebsen and H. Medwin: *On the Failure of the Kirchhoff Assumption in Backscatter,* J. of the Acoustical Soc. of Am. Vol. 72, pp. 1607-1611, 1982.

[45] D. S. Jones: *Diffraction by a Thick Semi-Infinite Plate,* Proc. Roy. Soc. A217, pp. 153-175, 1953.

[46] K. Kobayashi: *Diffraction of a Plane Electromagnetic Wave by a Rectangular Conducting Rod (I),* Bull. Facul. Sci. & Eng. Chuo University, Vol. 25 pp.229-261, 1982.

[47] −: *Diffraction of a Plane Electromagnetic Wave by a Rectangular Conducting Rod (II),* Bull. Facul. Sci. & Eng. Chou University, Vol. 25 pp.263-282, 1982.

[48] A. Michaeli: *A Closed Form Physical Theory of Diffraction Solution for Electromagnetic Scattering by Strips and 90° Dihedrals,* Radio Sci., Vol. 19(2), pp. 609-616, 1984.

[49] −: *A New Asymptotic High-Frequency Analysis of Electromagnetic Scattering by a Pair of Parallel Wedges: Closed Form Results,* Radio Sci., Vol. 20, pp. 1537-1548, 1985.

[50] Q. Zhang, E. J. Jull and M. J. Yedlin: *Acoustic Pulse Diffraction by Step Discontinuities on a Plane,* Geophysics, Vol. 55, No. 6, pp. 749-756, June 1990.

[51] S. Choudhary and L. B. Felsen: *Analysis of Gaussian Beam Propagation and Diffraction by Inhomogeneous Wave Tracking,* Proc. IEEE, Vol. 62, No. 11, pp. 1530-1541, 1974.

[52] W. Y. D. Wang and G. A. Deschamps: *Application of Complex Ray Tracing to Scattering Problems,* Proc. IEEE, Vol. 62, No. 11, pp. 1541-1551, 1974.

[53] J. B. Keller and W. Streifer: *Complex Rays with an Application to Gaussian Beams,,* J. Opt. Soc. Am., Vol. 61, No. 1, pp. 40-43, 1971.

[54] G. A. Deschamps: *Gaussian Beam as a Bundle of Complex Rays,* Electronics Letters, Vol. 7, No. 23, pp. 684-685, 1972.

[55] A. C. Green, H. L. Bertoni and L. B. Felsen: *Properties of the Shadow Cast by a Half-Screen When Illuminated by a Gaussian Beam,* J. Opt. Soc. Am., Vol. 69, No. 11, pp. 1503-1508, 1979.

[56] R. W. Ziolkowski: *Exact Solutions of the Wave Equation with Complex Source Locations,* J. Math. Phys. Vol. 26(4), April 1985.

[57] P. D. Einziger and S. Raz: *Wave Solutions under Complex Space-Time Shifts,* J. Opt. Soc. Am., Vol. 4 No. 1, pp. 3-10, Jan. 1987.

[58] G. A. Suedan: *High Frequency Beam Diffraction by Apertures and Reflectors,* Ph.D thesis, Dept. of Electrical Engineering, University of British Columbia, 1987.

[59] Q. Zhang and E. V. Jull: *Acoustic Pulse Diffraction by a Curved Half-Plane,* URSI International Symposium on Electromagnetic Theory, Stockholm, Aug. 1989.

[60] C. W. Chuang: *An Asymptotic Result for the Diffraction of Plane Waves Propagating Along a Cylindrically Truncated Flat Surface,* IEEE Trans. on Antennas and Propagat. Vol. AP-34, No. 4, pp. 503-509, April 1986.

[61] L. Kaminetsky and J. B. Keller: *Diffraction Coefficients for Higher Order Edges and Vertices,* SIAM J. Appl. Math., Vol. 22, No. 17, pp. 109-134, January 1972.

[62] N. Bleistein: *Uniform Asymptotic Expansions of Integrals with Stationary Points near an Algebraic Singularity,* Comm. Pure Appl. Math., Vol. 19, No. 4, pp. 353-370, 1966.

[63] J. J. Bowman, T. B. A. Senior and P. L. E. Uslenghi (Eds.): *Electromagnetic and Acoustic Scattering by Simple Shapes,* North-Holland Publishing Company, 1969.

[64] R. Tiberio, G. Manara, G. Pelosi and R. G. Kouyoumjian: *High-Frequency Electromagnetic Scattering of Plane Waves from Double Wedges,* IEEE Trans. on Antennas and Propagat., Vol. AP-37, pp. 1172-1180, 1989.

[65] M. J. Yedlin, B. B. Narod, G. Mellema, E. V. Jull and Q. Zhang: *The Imaging of Acoustic Scattering Data of Complicated Geological Structures,* Fall Meeting of American Geophysical Union, San Francisco, CA, Dec. 3-7, 1990.